Using Scanning Lasers for Real-Time Pavement Thickness Measurement

National Concrete Pavement Technology Center

CP Tech Center

Final Report
June 2006

ctre
Center for Transportation
Research and Education

IOWA STATE
UNIVERSITY

About the National Concrete Pavement Technology Center

The mission of the National Concrete Pavement Technology Center is to unite key transportation stakeholders around the central goal of advancing concrete pavement technology through research, tech transfer, and technology implementation.

Disclaimer Notice

Nondiscrimination Statement

Technical Report Documentation Page

1. Report No. IHRB Project TR-538	2. Government Accession No.	3. Recipient's Catalog No.	
4. Title and Subtitle Using Scanning Lasers for Real-Time Pavement Thickness Measurement		5. Report Date June 2006	
		6. Performing Organization Code	
7. Author(s) Edward J. Jaselskis, E. Thomas Cackler, Russell C. Walters, Jianzhong Zhang, Manop Kaewmoracharoen		8. Performing Organization Report No. CTRE Project 05-205	
9. Performing Organization Name and Address Center for Transportation Research and Education Iowa State University 2711 South Loop Drive, Suite 4700 Ames, IA 50010-8664		10. Work Unit No. (TRAIS)	
		11. Contract or Grant No.	
12. Sponsoring Organization Name and Address Iowa Highway Research Board Iowa Department of Transportation 800 Lincoln Way Ames, IA 50010		13. Type of Report and Period Covered Final Report	
		14. Sponsoring Agency Code	
15. Supplementary Notes Visit www.ctre.iastate.edu for color PDF files of this and other research reports.			
16. Abstract			

Due to limited budgets and reduced inspection staff, state departments of transportation (DOTs) are in need of innovative approaches for providing more efficient quality assurance on concrete paving projects.

The goal of this research was to investigate and test new methods that can determine pavement thickness in real time. Three methods were evaluated: laser scanning, ultrasonic sensors, and eddy current sensors. Laser scanning, which scans the surface of the base prior to paving and then scans the surface after paving, can determine the thickness at any point. Also, scanning lasers provide thorough data coverage that can be used to calculate thickness variance accurately and identify any areas where the thickness is below tolerance. Ultrasonic and eddy current sensors also have the potential to measure thickness nondestructively at discrete points and may result in an easier method of obtaining thickness.

There appear to be two viable approaches for measuring concrete pavement thickness during the paving operation: laser scanning and eddy current sensors. Laser scanning has proved to be a reliable technique in terms of its ability to provide virtual core thickness with low variability. Research is still required to develop a prototype system that integrates point cloud data from two scanners. Eddy current sensors have also proved to be a suitable alternative, and are probably closer to field implementation than the laser scanning approach. As a next step for this research project, it is suggested that a pavement thickness measuring device using eddy current sensors be created, which would involve both a handheld and paver-mounted version of the device.

17. Key Words		18. Distribution Statement	
concrete pavement quality assurance—concrete pavement thickness—electromagnetic eddy current sensors—laser scanning—ultrasonic sensors		No restrictions.	
19. Security Classification (of this report) Unclassified.	20. Security Classification (of this page) Unclassified.	21. No. of Pages 108	22. Price NA

USING SCANNING LASERS FOR REAL-TIME PAVEMENT THICKNESS MEASUREMENT

Principal Investigator
Edward J. Jaselskis
Professor
Department of Civil, Construction, and Environmental Engineering, Iowa State University

Co-Principal Investigators
E. Thomas Cackler
Associate Director for Construction Technology and Advanced Research,
Center for Transportation Research and Education, Iowa State University

Russell C. Walters
Assistant Professor
Department of Civil, Construction, and Environmental Engineering, Iowa State University

Research Assistants
Jianzhong Zhang
Manop Kaewmoracharoen

TABLE OF CONTENTS

LIST OF FIGURES

LIST OF TABLES

ACKNOWLEDGMENTS

EXECUTIVE SUMMARY

Taking core samples of concrete pavement is an essential step in the quality assurance process, and the quality of the samples determines pay quantities for contractors. Due to limited budgets and reduced inspection staff, state departments of transportation (DOTs) are in need of innovative approaches for providing more efficient quality assurance on concrete paving projects. In Iowa, the current technique is to take core samples of the pavement every 2,000 square yards. This labor-intensive process requires that the hole be patched. In addition, taking samples at this interval may not be thorough enough to catch all deficiencies. Payment methods for concrete paving contractors typically involve taking cores from the new roadway, averaging the lengths, and comparing this average to the design thickness. The unit price is then adjusted based on the results of these core samples. Pavement coring is expensive for state DOTs, and any approach that can eliminate this process will be beneficial.

The goal of this research is to investigate and test new methods that can determine pavement thickness in real time. One method, which uses a laser to scan the surface of the base prior to paving and then to scan the surface after paving, can determine the thickness at any point. Also, scanning lasers provide thorough data coverage that can be used to calculate thickness variance accurately and identify any areas where the thickness is below tolerance. Other benefits from this technique include the ability to determine concrete yield quantities and possibly smoothness. Although the proposed scope of this project only included scanning lasers, the scope was extended to examine the ultrasonic and eddy current sensors. A literature review revealed that ultrasonic and eddy current sensors have the potential to measure thickness nondestructively at discrete points and may result in an easier method of obtaining thickness.

The laser scanning methodology for this study involved the following: (1) investigating characteristics of the paving process, (2) using a laser scanner on three different sites (one involving an Iowa Special and two using a spreader with rebar and baskets, (3) processing the data to create clean surface models, (4) performing statistical analyses to determine thickness variability, and (5) summarizing the results. The ultrasound approach involved (1) establishing critical test parameters such as frequency, concrete mix design, and thickness; (2) performing laboratory tests; and (3) processing and analyzing the data. The electromagnetic test methodology was similar to that developed in using ultrasound.

There appear to be two viable approaches for measuring concrete pavement thickness during the paving operation. Laser scanning has proved to be a reliable technique in terms of its ability to provide virtual core thickness with low variability. Research is still required to develop a prototype system that integrates point cloud data from two scanners. Coordinate control will be required and can be achieved using a total station approach or GPS for x-y control and the stringline for accurate elevation readings. Electromagnetics has also proved to be a suitable alternative. This technique is probably closer to field implementation than the laser scanning approach. As a next step for this research project, it is suggested that a pavement thickness measuring device using electromagnetics be created; this would involve both a handheld and paver-mounted version of the device. The concept behind electromagnetic scanning is to place metal plates on the base in a random fashion. A bank of sensors can be mounted on the back of the paver to measure concrete pavement thickness in real time. DOTs or other quality controlling

agencies would also be able to use a handheld version for performing quality assurance. This technique would allow the measurement of concrete pavement thickness as well as dowel bar placement and depth. Laser scanning is still the preferred method for determining both concrete thickness and dowel bar placement because it can provide accurate and continuous monitoring capabilities. The electromagnetic approach, in contrast, is discrete in nature.

INTRODUCTION

Problem Statement

Taking core samples of concrete pavement is an essential step in the quality assurance process, and the quality of the samples determines pay quantities for contractors. Due to limited budgets and reduced inspection staff, state departments of transportation (DOTs) are in need of innovative approaches for providing more efficient quality assurance on concrete paving projects. In Iowa, the current technique is to take core samples of the pavement every 2,000 square yards. This is a labor-intensive process and requires that the hole be patched. In addition, taking samples at this interval may not be thorough enough to catch all deficiencies. Payment methods for concrete paving contractors typically involve taking cores from the new roadway, averaging the lengths, and comparing this average to the design thickness. The unit price is then adjusted based on the results of these core samples. Pavement coring is expensive for state DOTs, and any approach that can eliminate this process will be beneficial.

The goal of this research is to investigate and test new methods that can determine the thickness of the pavement in real time. By using a laser to scan the surface of the base prior to paving and then to scan the surface after paving, the thickness at any point can be determined. Also, scanning lasers would provide thorough data coverage that can be used to calculate thickness variance accurately and identify any areas where the thickness is below tolerance. Other benefits from this technique involve the ability to determine concrete yield quantities and possibly smoothness. Although the proposed scope of this project only included scanning lasers, the scope was extended to examine the ultrasonic and eddy current sensors. Ultrasonic and eddy current sensors have the potential to measure thickness nondestructively at discrete points and could result in an easier method for obtaining thickness.

Project Objectives

The principal objective of the research is to develop the algorithms that can process real-time laser scanning data to create an accurate 3D model of the pavement that can then be used to determine pavement thickness at any point. Such a device will eliminate the need for state DOTs to take cores in order to assess this aspect of quality. This device can also be considered for in-process control of the paver, since real-time concrete depths will be calculated. This real-time method may eliminate the need for the owner and contractor to take depth measurements during the paving process.

1

VISION OF THE PROPOSED SYSTEM

Figure 1 shows a possible setup for the implementation of a laser scanning system. The current vision consists of two 2D scanning lasers, with one mounted on the front to measure subgrade profile and the other mounted on the back to measure pavement surface profile. The rear scanning laser may not be necessary if the Ames Engineering (which involves lasers) or the GOMACO (which uses ultrasound) concrete pavement smoothness techniques can provide the necessary profile of the paved surface.

Coordinate control can be accomplished through the total station tracking of prisms mounted on the paver and through paver slope measurement, similar to the system that GOMACO currently uses in its stringless control system for slipform pavers (Alta Ingenieria 2000; Gomaco 2004).
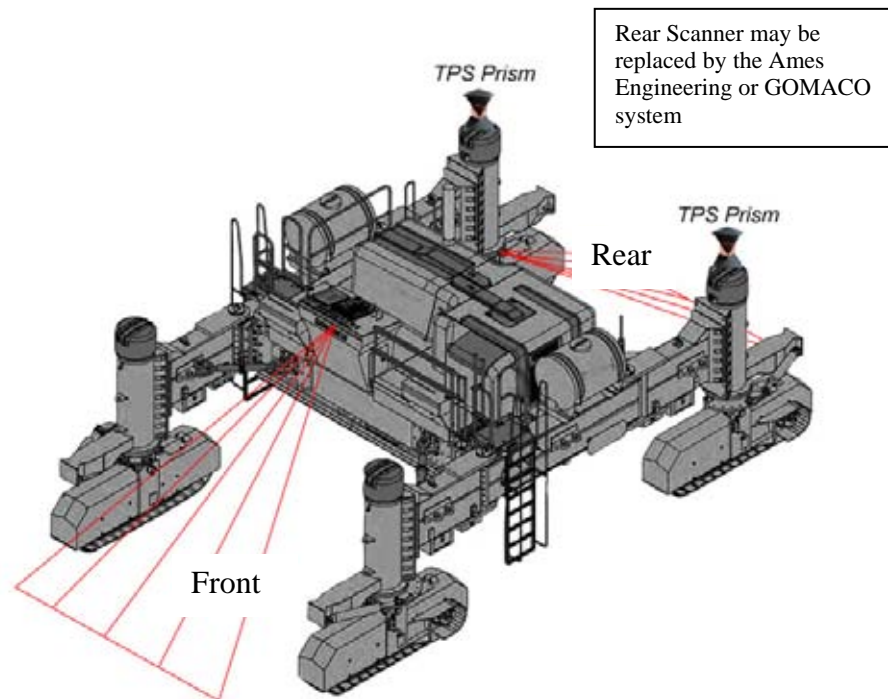
Figure 1. Anticipated vision of laser scanning concrete thickness profiler

A schematic view of the laser scanning concrete thickness profiler is shown in Figure 2. The coordinate control system consists of two tracking total stations that each track one prism mounted on the paver. The tracking total stations send coordinate data to a computer mounted on the paver. Using the data from the total stations and slope readings from a paver-mounted tilt sensor, the coordinates of the paver are determined in three dimensions. Scanning lasers mounted on the front and back of the paver constantly scan the surface of the subgrade and the installed pavement. An accelerometer mounted on the lasers record vibrations to be used to correct vibration-induced errors in the scanned profile.
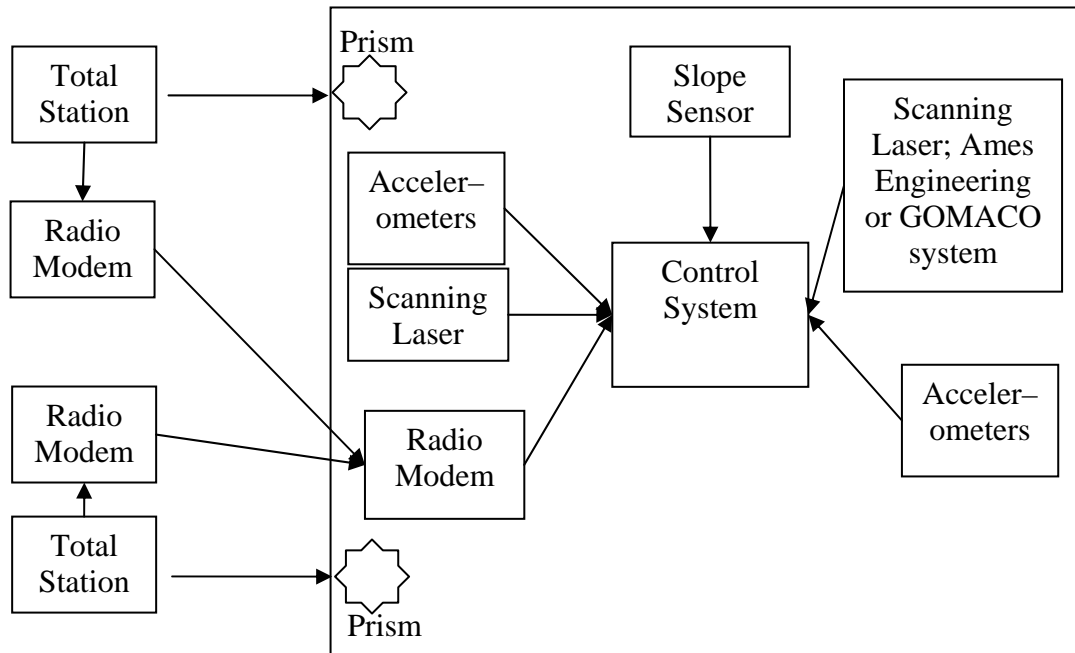
Figure 2. Schematic view of setup for laser paver application using tracking total stations

The setup of Figure 1 is ideal when coordinate control already exists on the paver, such as that required for stringless paving applications. For instance, the stringless control system developed by GOMACO uses three Leica Geosystems tracking total stations, which cost approximately $35,000 each. An alternative setup is shown in Figure 3, where velocity and direction are tracked by an onboard system. By tracking the speed of each of the paver tracks, the compass orientation, and the slope of the paver, it may be possible to relatively align the forward and rear laser scans. Other methods to aid in obtaining position include attaching laser reflectors to grade control stakes and GPS signals enabled with a wide area augmentation system (WAAS). Although such a system would not be accurate enough to support stringless paving, such a system may allow sufficient precision to determine pavement thickness. Determining pavement thickness requires that the rear scan of the pavement surface be overlaid with the corresponding scan of the subbase from the forward laser.
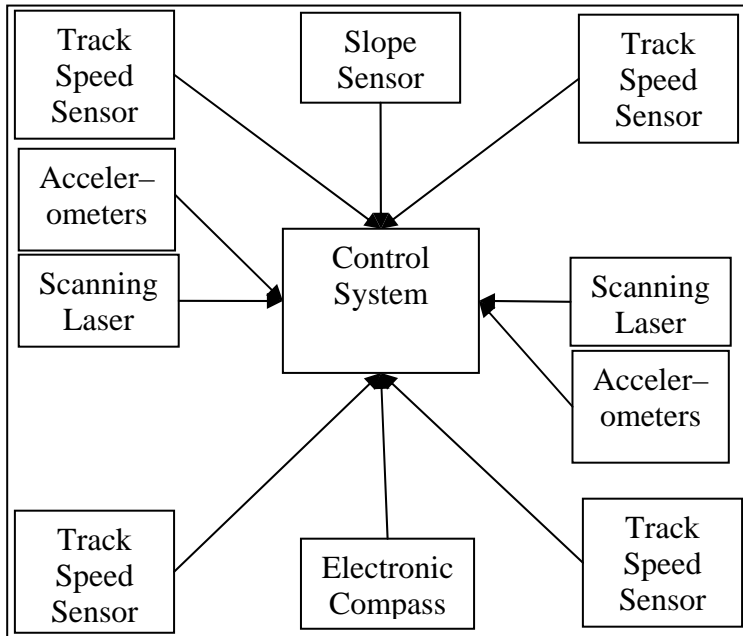
Figure 3. Schematic view of setup for laser paver application using an onboard relative coordinate system

LITERATURE REVIEW

NDE Methods Used to Spot Check Pavement Thickness

Impact echo methods have been used to determine pavement thickness with some success (Civil Engineering 1994; Public Works 1995). The technique requires sophisticated neural networks to identify the reflection of the impact signal from the bottom surface of the pavement. High-frequency ultrasound has also been evaluated for its use in measuring pavement thickness. By using a process known as split spectrum processing, ultrasonic techniques have been successful in measuring the thickness of stainless steel and other materials. Although encouraging results have been obtained for concrete testing, further work is needed because concrete produces more scattering than a homogenous material such as steel (Popovics, Bilgutay, and Karaoguz 2000).

The shadow moiré (Guralnick, Suen, and Smith 1993) method projects lines of light onto the test surface by projecting light through a grate. A camera records the pattern of lines projected onto the test surface. By analyzing the distortion of the lines, the surface profile can be determined. Although this technique has shown promise as a quick and cost-effective method for acquiring 3D images, the method is not well-suited for the real-time monitoring of paving because of the difficulty of projecting light onto the surface in the presence of full sunlight. There will also be many obstructions, such as rebars, people, and concrete trucks that produce variations in the environment.

Ground penetrating radar has been used to detect voids and locate rebars in concrete and may hold promise for determining pavement thickness, but this method needs further development to produce automated data evaluation (Maierhofer 2003). The additional factor of wet concrete may also contribute to variability in the results.

Stereo vision can be used to capture 3D data by using two cameras. Some difficulties, however, include low visibility caused by dust, fog, and poor lighting. Radar is a well-developed technology that can measure distance, but it is typically not used in these types of applications due to the potentially harmful effects of radar on people.

One widely used method for measuring the distance of objects is called laser range finder or LIDAR (light detection and ranging) (Wozencraft and Millar 2005). In order to calculate the distance between the laser device and an object, a laser pulse is sent toward the objects, and the device determines the length of time before the laser returns to the camera. The accuracy of LIDAR depends on the laser pulse and the laser device.

Lasers have long been used to measure distance. Some examples include airborne scanning lasers for terrain mapping (Cutelius 1998), 3D scanning lasers for recording as-built construction details (Sawyer 2002), and 3D imaging on a very large excavator (Roberts, Winstanley, and Corke 2003). Figure 4 shows the drag line used in a test by Roberts, Winstanley, and Corke (2003), and Figure 5 shows a laser-generated 3D digital terrain map (DTM) relative to the drag line. This project presented many challenges for the researchers: the laser scanner needed to see through rain and dust, the bucket and its associated ropes and chains were swinging beneath the

laser and could obscure the laser scanner's view, and the DTMs had to be computed in real time. A laser scanning system was chosen because it addressed these issues better than other available solutions. By combining position data from the dragline with the laser-scanned data, the researchers were able to establish the Cartesian position of each scanned point in real time.

RIEGL Laser Measurement Systems (2004) has developed a high-speed 2D laser scanning system (LMS-Q250i) that has been used for profiling railroad tunnels. The range is up to 15 meters with a 5 mm measurement resolution (Figure 6).

Figure 4. A Bucyrus-Erie 1350 dragline (Roberts, Winstanley, and Corke 2003)
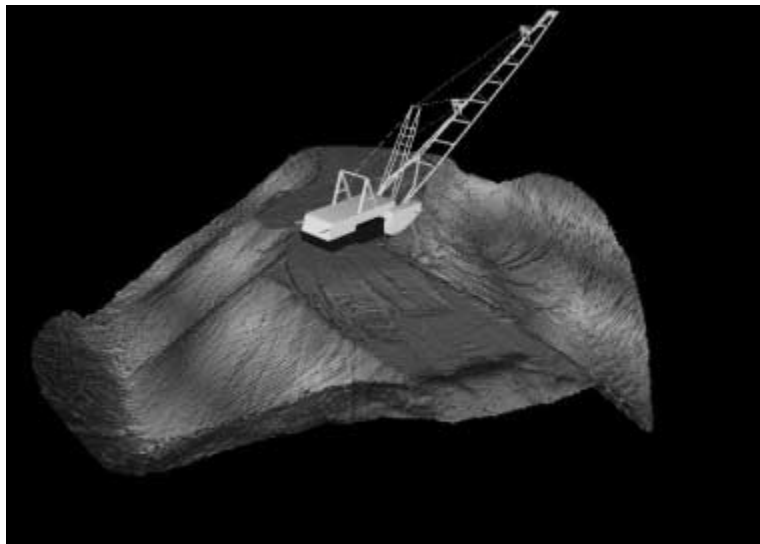
Figure 5. A laser generated digital terrain map and dragline (Roberts, Winstanley, and Corke 2003)

Figure 6. Riegl 2D laser scanner LMS-Q20i (RIEGL 2004)

Another challenge for this nondestructive evaluation (NDE) tool is the ability to capture coordinate data within acceptable tolerances for a concrete paver. One approach is to use tracking total stations, such as the system developed by Leica Geosystems and GOMACO (GOMACO 2004). Another system developed by CMI Terex and Geologic Computer Systems uses a combination of GPS and laser for coordinate controls (Cable and Jaselskis 2004). Both of these systems have shown that coordinate control for slipform pavers is possible.

NDE Methods Used to Determine Pavement Smoothness

The conventional approach to determining concrete pavement smoothness involves the use of a profilometer to determine a smoothness index for the pavement (Grogg and Smith 2001). Advancements in the use of lasers and ultrasonic techniques have been and are currently being developed. For example, Ames Engineering, Inc., is using laser beams fired in close proximity to the concrete pavement in order to develop a smoothness profile (see Figure 7, from http://www.acuityresearch.com/products/ ar600/ common-applications-road-profiling.shtml). An algorithm is used to account for scattering caused by the grooves in the pavement. GOMACO also claims to be able to create a smoothness profile using ultrasound.

Figure 7. Ames Engineering, Inc., road profiling laser to test smoothness

METHODOLOGY

The methodology for the present research involved investigating three NDE approaches for determining concrete pavement thickness. The initial scope of this project was to investigate only the use of laser scanning, but upon the recommendation of the technical committee the scope was expanded to include ultrasound and electromagnetics. Appropriate tests were then established for each of the techniques. Laser scanning involved extensive field testing on actual paving projects during the summer of 2005. In contrast, the ultrasonic and electromagnetic tests were performed in a laboratory. The overall purpose of this initial research phase was to identify the most suitable NDE technologies for measuring concrete pavement thickness and then to establish a plan for implementation.

LASER SCANNING

Field Trip Preparation

After reviewing the literature, the research team visited four paving projects to observe the process, consider equipment mounting options, and develop a plan for taking laser scans. Information about these projects is listed below.

First Project: 18 May 2005

Date:	18 May 2005
Place:	Fort Dodge, Webster County, Iowa
Weather:	60°F, windy
Pavement Type:	Concrete (see Figure 8 for an image of the project's paving train)
Contractor:	Fred Carlson
Contact Person:	Dennis Klocke
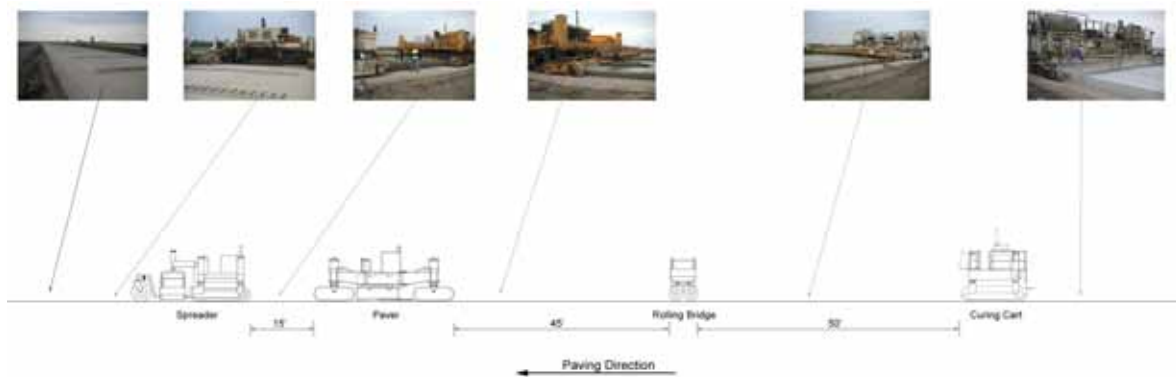
Figure 8. Illustrated paving train image of Fred Carlson

Second Project: 14 June 2005

Date:	14 June 2005, 11 a.m.
Place:	IA-60 in Hospers, Sioux County, Iowa
Weather:	Cold and raining; the plant was shut down and no paving occurred
Pavement Type:	Concrete
Contractor:	Cedar Valley Corp.
Contact Person:	Craig Hughes, project manager, (319) 290-5617

Memo
The paving plant had shut down before the research team arrived due to predictions of heavy rain. However, the team visited the plant to see the concrete machines and talk to the project manager. Cedar Valley Corp. uses a Guntert & Zimmerman concrete spreader and concrete slipform paver, as well as a GOMACO texture/cure machine (see Figure 9, from right to left).

The research team learned that (1) the pavers already have vibration sensors that might be useable in the new concrete thickness profiling method, (2) the paver will insert dowel bars during the paving process in the middle of the road, and (3) subbase elevations vary up to half an inch.

Figure 9. Paving train from Cedar Valley Corp. on IA-60 project

Third Project: 14 June 2005

Date: 14 June 2005, 12 p.m.
Place: IA-60 in Alten, Sioux County, Iowa
Weather: Cold and scattered rain
Pavement Type: Concrete
Contractor: Irving F. Jensen Co.
Contact Person: Terry Hamer

Memo
The paving crew was operating while the research team was present, despite scattered rain. Researchers met the Iowa DOT officer and talked about the project. During the project, concrete trucks were unloading concrete about every one minute.

Irving F. Jensen Co. uses a GOMACO concrete spreader, CMI concrete slipform paver, and a Guntert & Zimmerman texture/cure machine. The research team learned that (1) Jensen Co. uses a V-float at the back of the paver to smooth the concrete, which may obstruct the laser beam (see Figure 10); (2) the workers use bull floats near the rear of the V-float.

Figure 10. Jensen Co. paver with the V-float

Fourth Project: 22 June 2005

Date: 22 June 2005, 1 p.m.
Place: G-61 (county road) in Macksburg, Madison County, Iowa
Weather: Hot and dusty, around 90°F
Pavement Type: Iowa Special
Contractor: Fred Carlson
Contact Person: Mark Williams, County Engineer

Memo
Fred Carlson was using a CMI autograder (Iowa Special), a RexCon concrete slipform paver, and a Guntert & Zimmerman texture/cure machine (see Figure 11, from left to right). The researchers also learned the following:

- The CMI autograder does a final grade trim, so subbase scanning will have to be done between the Iowa Special and the paver.
- Concrete is dumped from the front of the paving train onto a belt placer that is part of the CMI Autograder, transported over the top of the CMI Autograder, and placed in the rear.
- Rebar baskets are placed by workers behind the CMI Autograder in front of the concrete.
- There were no shoulders on either side of the road.
- The combination of crushed concrete as a subbase and the final trim from the autograder produced a lot of dust, which may be detected by the laser.

Figure 11. Paving train from Fred Carlson on G-61

12

Thickness Data Collection Procedure

Using knowledge gained during the field visits, the research team then developed a plan to use a commercially available, survey-grade scanning laser to capture thickness data from actual paving projects. A laser scanner was rented for a one-week period and was used to capture data from the following three projects.

First Project

Date: 11 July 2005
Place: South of Hospers, Iowa, IA-60, northbound lane
Station ID: 204+90
GPS Coordinates: N43.03.4818/W095.54.7183
Weather: Hot and sunny
Pavement Type: Concrete
Contractor: Cedar Valley Corp.
Contact Person: Craig Hughes

Figure 12. Aerial photo near project site near Hospers, Iowa

Second Project

Date: 11 July 2005
Place: Near Seney, Iowa, IA-60
Station ID: 53+90
GPS Coordinates: N42.50.8846/W096.08.4483
Weather: Hot and sunny
Pavement Type: Concrete
Contractor: Irving F. Jensen Co.

Figure 13. Aerial photo near project site near Seney, Iowa

Third Project

Date: 13 July 2005, 10am
Place: US 30, West of Tama, Tama County, Iowa
Weather: Hot and dry, 90°F
Pavement Type: Concrete
Contractor: Fred Carlson

Figure 14. Aerial photo near project site near Tama, Iowa

The research team used an HDS3000 Leica Geosystems scanning laser to measure the thickness with three scans: (1) the subbase scan, (2) the concrete scan between the paver and the curing cart, and (3) the concrete scan after the curing cart (see Figure 15).

Figure 15. Performing laser scan on the subbase level

Researchers recorded the Earth coordinates of a laser scan target using GPS (see Figure 16) to identify the location of the scan.

Figure 16. Using GPS on the target

Setting up the laser scanner took about 25 minutes before the first scan, including finding a suitable location, setting the tripod, opening the laser scanner, opening the software, and imaging the surrounding area. Each scan took about 5–15 minutes, depending on the scanning resolution.

Moreover, an additional scan was made for the texture at the Tama location. The research team scanned a one-by-one-foot area of the concrete surface at high resolution, the 1000-by-1000-point resolution, to experiment with the surface sampling.

Figure 17. Concrete texture detail at the Tama project

At the end of the day, the research team collected additional scan data by scanning the Marston water tower (168 feet tall), Beardshear Hall (high motif detail), and Howe Hall (a glass building) on the Iowa State University campus. It was discovered that the laser scan did not capture the glass material. The laser went through the glass and detected the wall inside Howe Hall.

Data Collection Results from the Construction Projects

The data from the construction sites were reviewed using Cyclone, a software tool provided by Leica Geosystems to process the point cloud. The software is useful for viewing, measuring, and filtering the data. Some major functions are listed below:

- Distance measuring, which measures the distance between two or more point clouds by selected points.
- Point cloud unification, which reduces the density of the point clouds from the original files. This reduces the file size and number of point clouds for easy later use.
- Smooth surface region growing, which separates point clouds into different pieces defined by the positions and closeness measurements of the point clouds. The system divides different point clouds with different similarities by parameters the user sets. After this function processing, major noise sources, such as people walking in front of the scanner, can be easily removed.
- Cross-sectioning, which automatically generates cross-section views of the whole roadway along polylines or curves. The sections are created following the parameters the user has set, as shown in Figure 18. This cross section can be compared to the actual design, such as the design shown in Figure 19.
- Triangular irregular network (TIN), which creates a TIN surface from the point clouds by selecting point cloud(s). A TIN surface can be used for generating, for instance, the shortest distance between TINs or the volume between two TINs. Figure 20 shows two TIN surfaces created from the real concrete pavement (top) and subbase (bottom). Data from two TIN surfaces are generated to find the thickness of concrete (differentiating between the upper TIN and lower TIN), as shown in Figure 21 with Microsoft Excel.
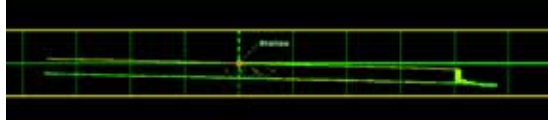
Figure 18. Cross section generated from the Cyclone software
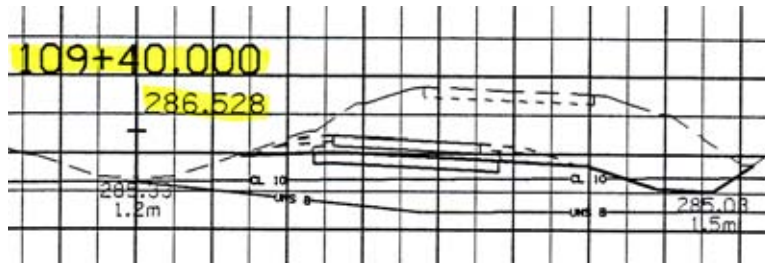
Figure 19. Cross section from the drawing
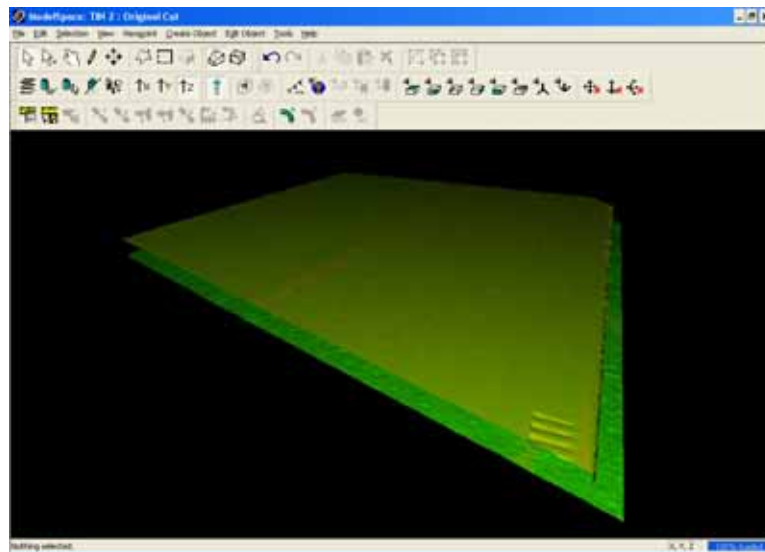
Figure 20. TIN of concrete surface and subbase surface

17

Figure 21. Data of XYZ positions of TIN data

The laser scan data can be used directly in Leica Geosystem's Cyclone software or exported to other software. With the features found in Cyclone, point clouds can be exported to other programs for further analysis. However, analysis can be difficult because the data set may be very large. To reduce the file size, point clouds can be either selected in smaller pieces or unified and exported separately.

Other Examples Using Laser Scanning

The research team used the laser scanner on the Iowa State University campus to gather data from different objects, such as the Marston water tower, Howe Hall, Hoover Hall, and Beardshear Hall. Figure 22 shows the scan of the Marston water tower, Howe Hall, and Hoover Hall. According to the laser scan data, the tower height is 164 feet 9 inches from the base; according to data published on the Iowa State University Daily website, the height is 168 feet.
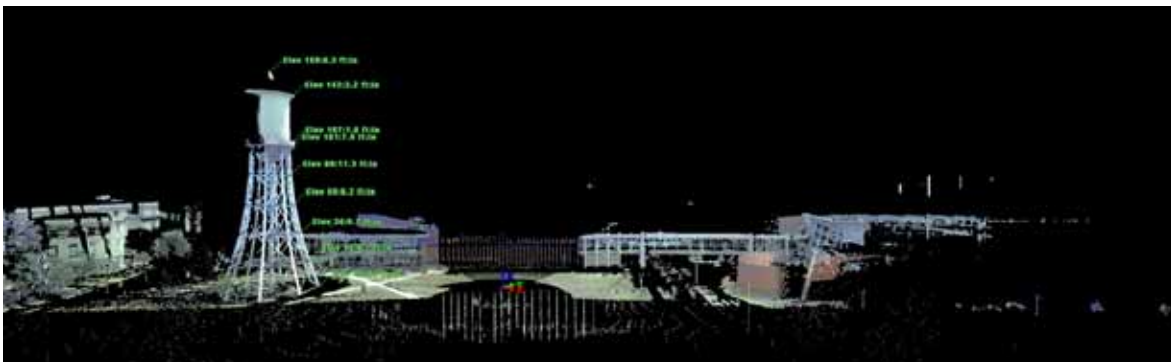
Figure 22. Example scan finding height of the tower

18

A high-resolution scan was also performed of the top motif on the front of Beardshear Hall. Although the scanner was 135 feet away from the object, the scanner was able to capture point data at a 0.5 x0.5 inch grid (see Figure 23). However, it was found that the laser beam cannot detect an object that is transparent and highly reflective, such as a mirror or a chrome bar.

Figure 23. Example high-resolution scan

Observed Features of Thickness Data

Figure 24 illustrates laser scan data for the pavement and subbase sections of IA-60 in Hospers, Iowa (contractor Cedar Valley Systems). The data was gathered with the Leica Geosystems HDS3000 laser scanner and viewed through the Cyclone software. The point cloud view shows the raw data points directly from the laser scanner without any filtering or noise removal. The data is viewed horizontally along the direction of paving. The upper line in the point cloud section is the pavement and the lower line is the subbase. The subbase line is slightly thicker and fuzzier, which is expected, as the aggregate surface of the subbase is not as smooth or finely graded as the pavement surface. It can be noted that, from this view, the pavement and subbase do not vary significantly along the axis of paving. This observation will be useful for developing data filtering and prediction algorithms that can be used at different sites without customization. TIN models were then created from the point cloud by connecting each adjacent point cloud.

Measuring thickness directly from point cloud data is difficult because it is highly unlikely that the laser will capture data along the same Z axis for both the subbase and pavement. Therefore, data interpolation and prediction are necessary. The TIN mesh helps because the TIN is a surface and the Cyclone software can measure the distance between the two TINs along user-defined grid spacing. The thickness shown in the figure was estimated this way. The thickness is shown again with the vertical scale enhanced to magnify the data trends. The thickness varies across the road more than along the axis of paving. The pavement thickness increases by about 10mm from the left to the right, with a slight peak in the middle of the road.
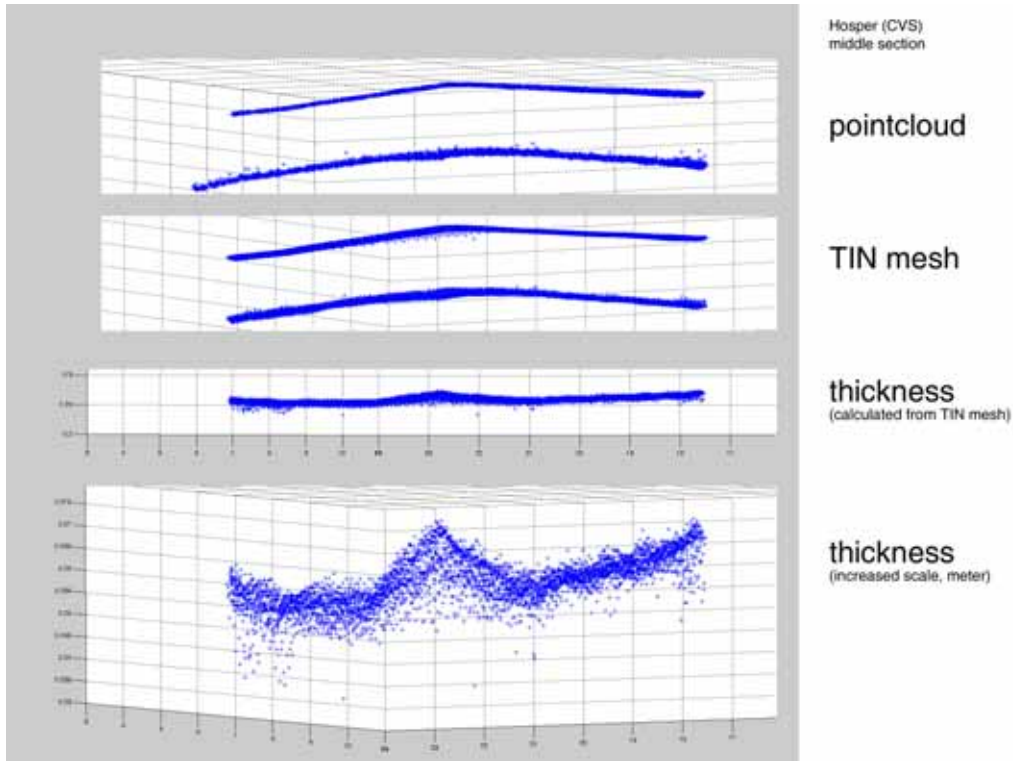
Figure 24. Thickness data from Hospers, Iowa

The data for Seney and Tama also show a variance of about 10mm for the thickness along the lateral axis of the road (Figures 25 and 26). There is also a slight bulge of about 5mm on the right side of the road that causes a slight dip in pavement thickness. As seen from these figures, there is significant variance in the pavement thickness, and the main source of the variance is the subbase.
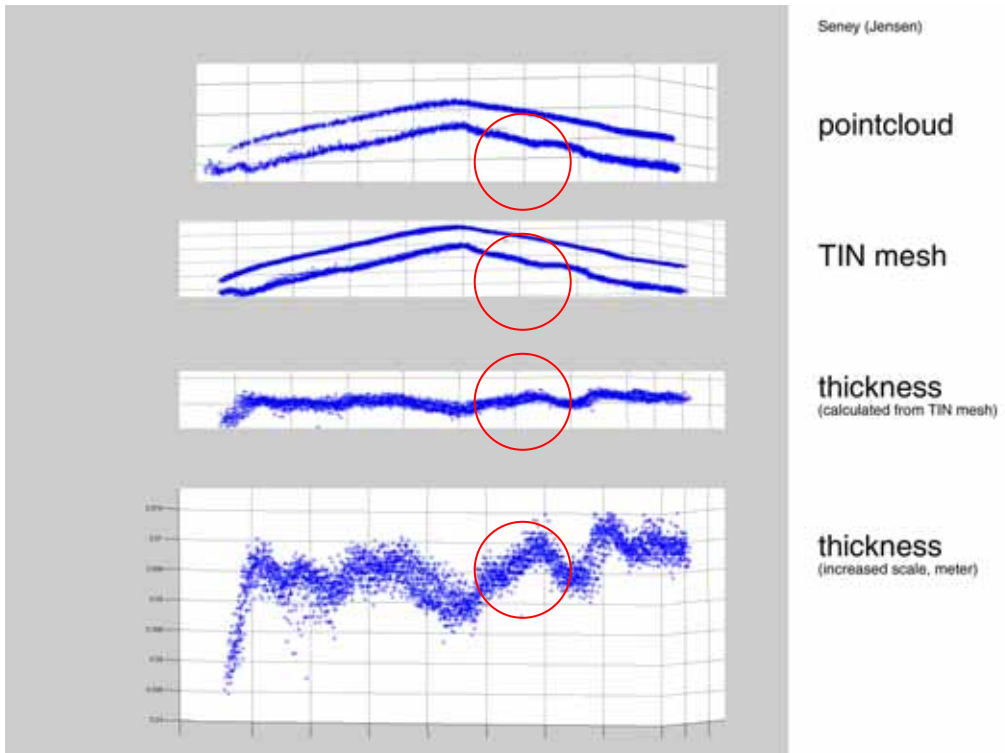
Figure 25. Thickness data from Seney, Iowa
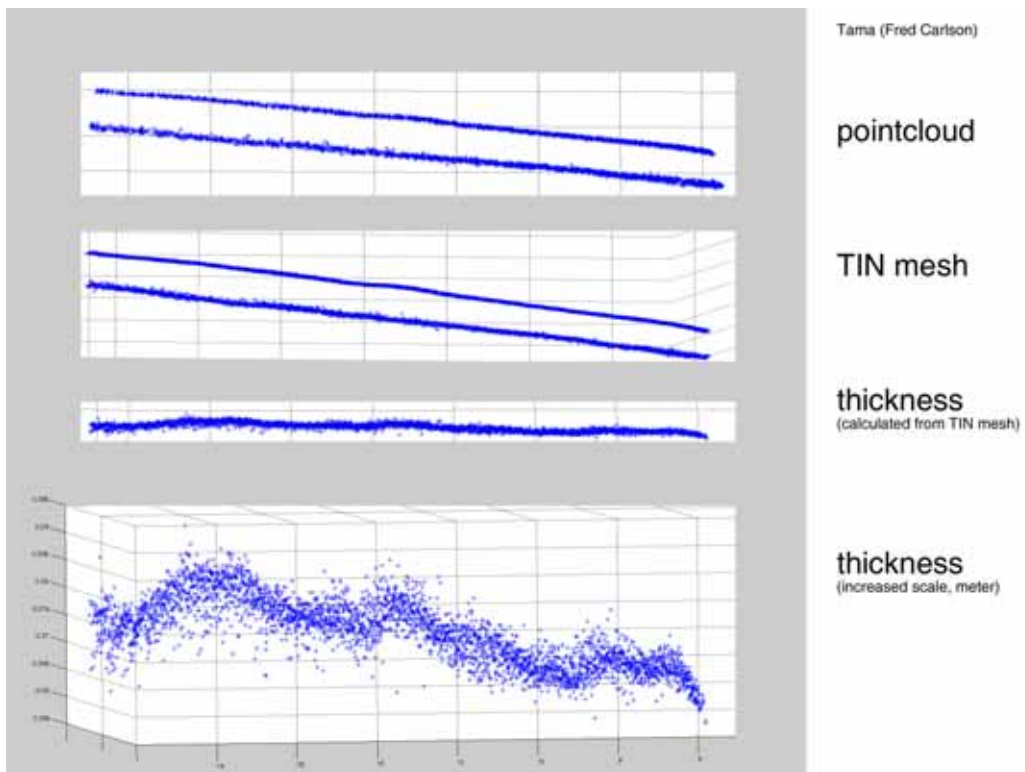
Figure 26. Thickness data from Tama, Iowa

Algorithms for Data Processing

Scanning lasers are very useful for collecting a large amount of data very quickly. However, the amount of data can produce some challenges for data processing. For instance, a single surface scan, such as the one in Figure 27, contains over 100,000 data points, with each having an X, Y, and Z axis coordinate.
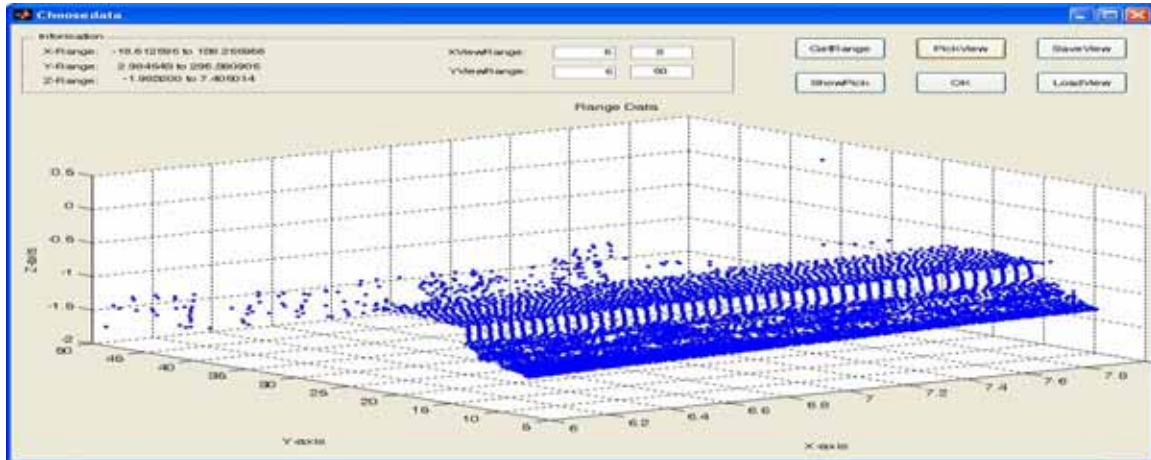
Figure 27. Unprocessed surface scan with over 100,000 data points

Clustering

The first step in processing was to choose a one-meter section of road. This was done to reduce the data set size to about 4,000 points, which can easily be processed by a computer with a 2.8 GHz Pentium 4 processor. This data set is shown in Figure 28. The surface is easy to identify, with a smooth, flat surface. Another feature noted in the figure is one of the edges. The scanning laser was stationed to the right of the image and could not see the other edge. Some background noise was also detected on the other side of the pavement.
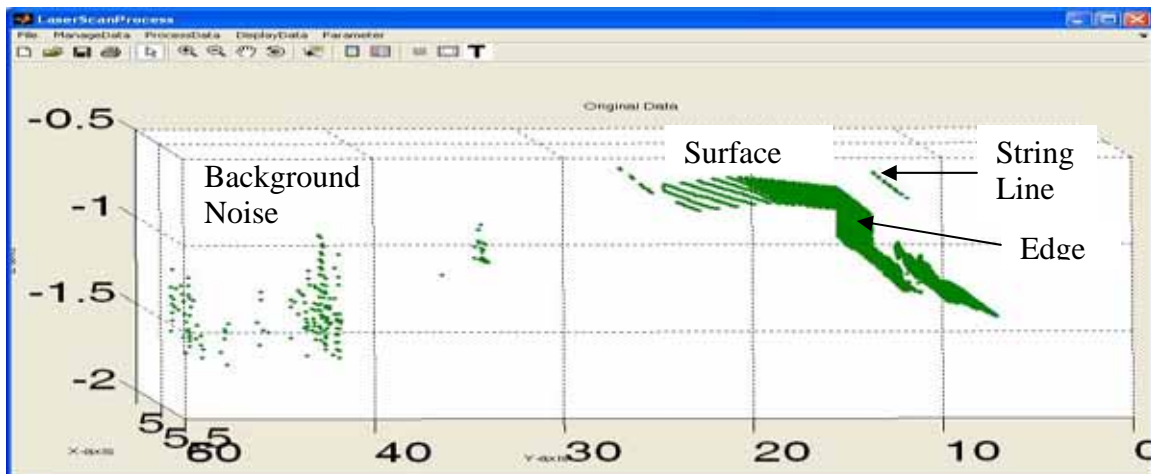
Figure 28. A one-meter-long section of the pavement

The string lines and the background noise are easy to remove through clustering. This concept is best explained through an example. Figure 29 shows a set of 10 data points. If a point, such as x9, is identified as a starting point for a cluster, then the points within that cluster can be identified by comparing the Euclidean distance between x9 and all other points. In this case, x5, x7, x8, and x10 are much closer to x9 than the other points, so a cluster is created containing these 5 points. In the application of laser scans of pavement, the distance between points on the pavement is known to be within a certain range, both horizontally and vertically. This a priori knowledge can be used to set the cluster threshold. Using this type of algorithm, Figure 28 was processed to produce Figure 30. Figure 30 shows the laser scan without string lines and background noise. This type of processing also removes the noise caused by a worker passing by in front of the scanning laser.
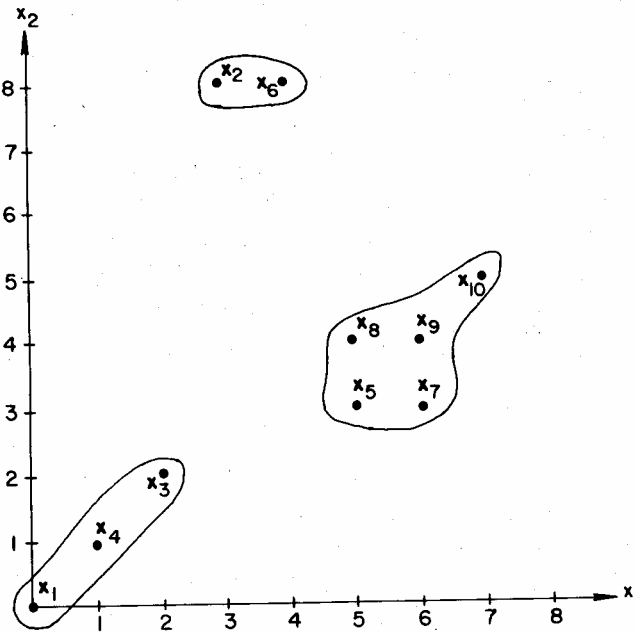
Figure 29. Example of 2D clustering (Tou and Gonzales 1974)
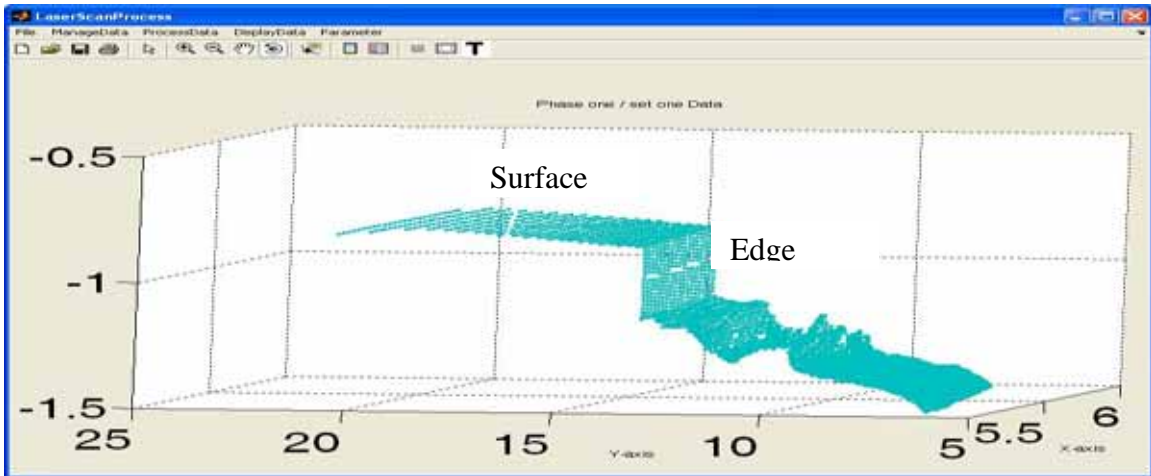
Figure 30. A one-meter-long section of pavement after noise removal

Feature Identification

Once the noise has been removed through clustering, the next step is to identify the edges of the pavement. One challenge of finding the edge of the pavement is that the laser often does not scan the edge. The dots in Figure 31 represent the laser scan across the pavement. As the laser scans across the surface, points are recorded at a fixed angular displacement. If, for instance, that angular displacement results in a distance (represented by $d1$ in the figure) of two inches between laser samples at the edge of the pavement, the point closest to the edge could be up to 2 inches away from the pavement. The next laser shot will be off the edge of the pavement and at a noticeably large distance away (that is, $d2$ will be much larger than $d1$). Also, the elevation of the point off the edge will be noticeably lower. The difference in the distances $d1$ and $d2$, as well as the drop in elevation, can be used to detect that the laser has encountered the edge of the pavement, and the value of $d1$, which would be known, would represent the maximum error of edge detection. For this reason, $d1$ needs to be constrained to meet the desired accuracy. The error introduced by this error will impact estimates of pavement width and yield quantities. If only thickness is desired, then the value of $d1$ is not critical.
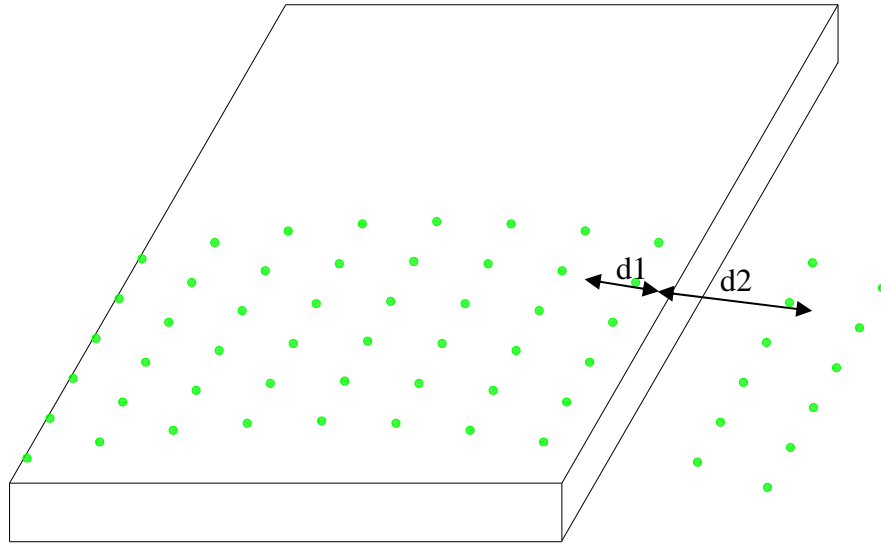
Figure 31. Detecting the pavement edge

Figure 32 shows the result of edge detection. Once the edges are located, all data outside of this range are removed. The key features for data processing efficiency identify the right and left edges as well as the crown. The crown of the road is also identified by looking for the change in grade slope.
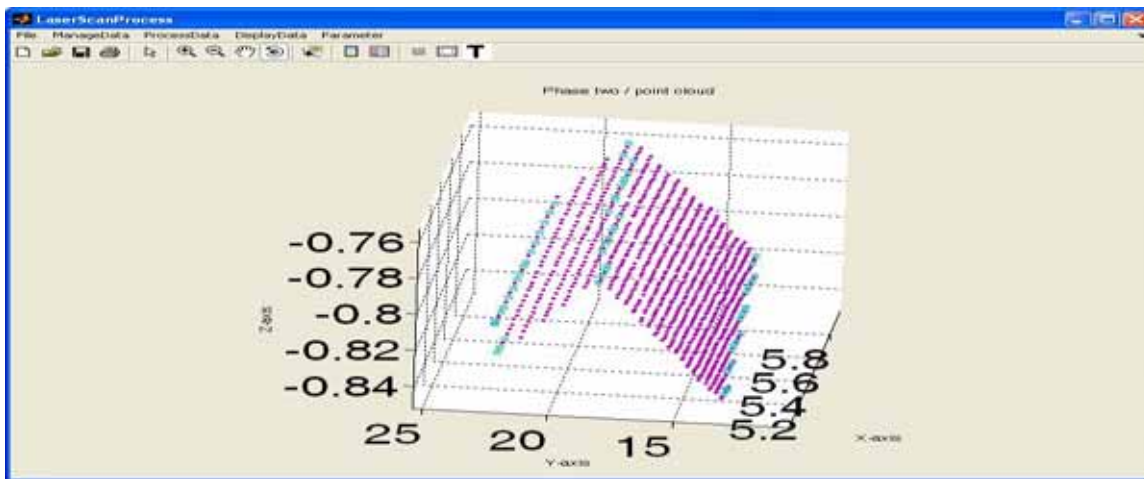
Figure 32. A one-meter-long section of pavement after edge identification

Subbase Processing

The subbase, shown in Figure 33, was selected by taking all points from the subbase scan that lie underneath the pavement section identified in Figure 32. Noise was removed from the subbase by using clustering analysis.
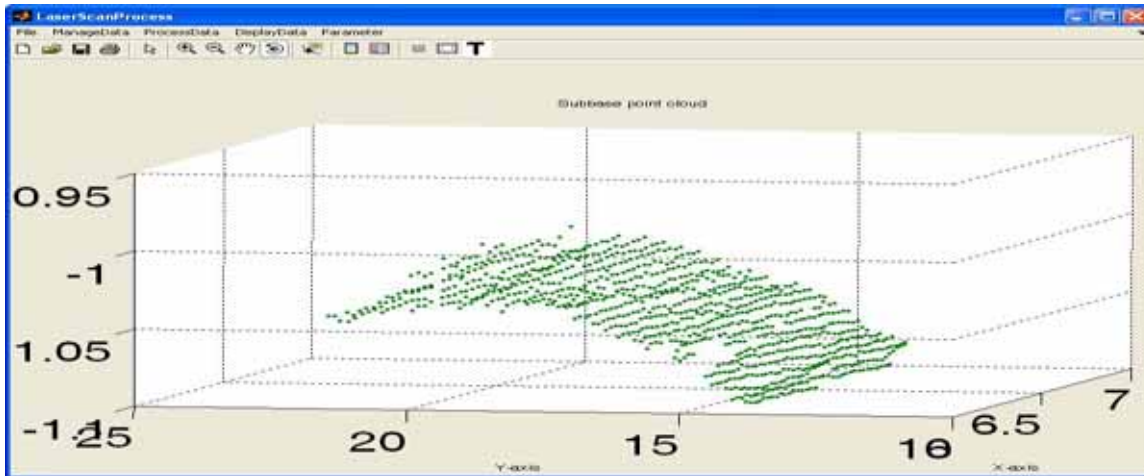
Figure 33. Subbase data set aligned with identified pavement

Virtual Core

Thickness can be estimated from this data by taking a virtual core. The user sets the core diameter, and a vertical core is then "drilled." An average is taken of the points on the surface and subbase, respectively, and then the distance is calculated between the two surfaces. For this example, the thickness was 0.255 meters for a road with a design thickness of 0.260 meters. A more rigorous approach using appropriate statistical techniques is described in the next section.
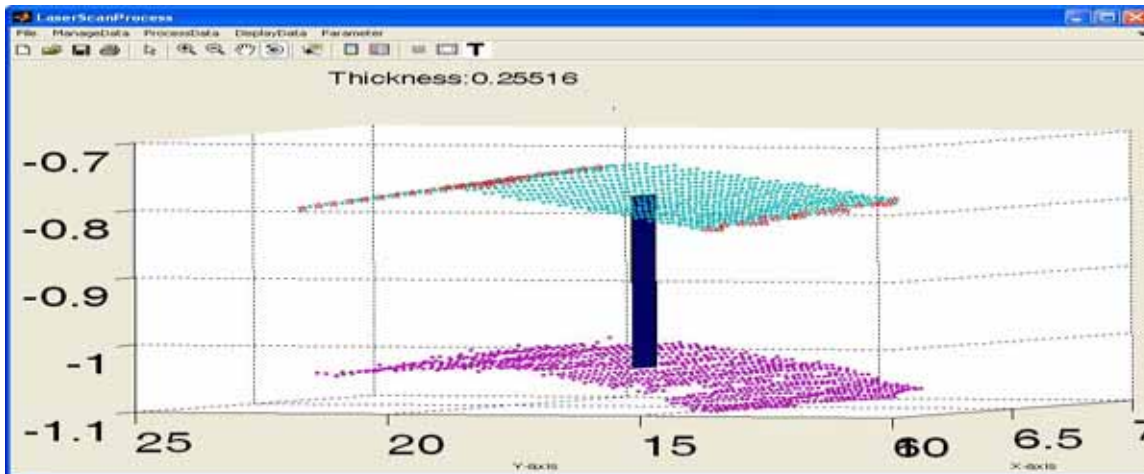
Figure 34. Virtual core

Data Processing Results

As demonstrated in the preceding sections, laser data can be processed automatically.

Ordinary Kriging Method of Data Interpolation

There is a challenge in measuring the thickness of the pavement from the laser scan point clouds. Ideally, the thickness would be measured by calculating the distance between a point in the surface scan point cloud and a point from the subbase point cloud that lies in the same Z axis. In reality, the odds of the two scans aligning in this fashion is highly unlikely. For this reason, data interpolation is needed to estimate surface and subbase points that lie in the same Z axis. This problem was solved by using a spatial statistical tool called ordinary kriging. In ordinary kriging, the spatial relationship of the data is analyzed and modeled. Finding spatial models is not always possible; however, these models were determined for each of the three sample projects. The following sections describe the process of developing the ordinary kriging models. Using the ordinary kriging models, 2,000 thickness values were generated for each of the three projects. These data sets were used to quantify the confidence intervals between the measured thickness data and the model of the road, which is an estimate of the accuracy of the laser system. Also, the effect of sampling density on accuracy was measured. A summary of the kriging analysis is presented here. Refer to the appendix for a more thorough analysis.

Ordinary Kriging

To predict the depth of the pavement, ordinary kriging was employed. The steps of ordinary kriging include first calculating the empirical variogram. To calculate the empirical variogram, the distance between two points is calculated for all possible pairs of points. The distance between two points is then used to place each pair of points into a bin with other pairs that are separated by a similar distance. Suppose that there are m bins, such that h_n represents the nth bin. An estimate of the variability of the difference between the z-coordinate for each pair of points in a bin is calculated using the method-of-moments estimator, which is given as

$$\frac{1}{|N(h_n)|} \sum_{N(h_n)} \{Z(s_i) - Z(s_j)\}$$

(1)

Where $N(h_n)$ represents all pairs of points in the nth bin,

$|N(h_n)|$ represents the number of pairs of points in the nth bin, and

$Z(s_k)$ represents the z-coordinate at location s_k for $k = i, j$.

The empirical variogram is then a plot of the estimate of variability as calculated by Equation 1, represented as $2\hat{\gamma}(h_n)$ versus the midpoint of the bin range. If $\hat{\gamma}(h_n)$ is plotted instead of $2\hat{\gamma}(h_n)$, then the variogram is called a semi-variogram.

A theorectical variogram is then fitted to the empirical variogram. The goal is to fit a theoretical variogram that has a shape very similar to that of the empirical variogram. There are several theoretical variograms, such as linear, power, and wave, but two theoretical variograms in particular were similar in shape to the empirical variograms for all the pavement and subbase data sets: the spherical and exponential variograms. The spherical semi-variogram is represented by the following equation:

$$
\gamma(h \mid \theta) = \begin{cases} 0, & h = 0 \\ c_0 + c_s\{(3/2)(h/a_s) - (1/2)(h/a_s)^3\}, & 0 < h < a_s \\ c_0 + c_s, & h \geq a_s \end{cases}
\tag{2}
$$

Where c_0 is interpreted as the nugget, c_s is the partial sill, and a_s is the range.

Similarly, the exponential semi-variogram is as follows:

$$
\gamma(h \mid \theta) = \begin{cases} 0, & h = 0 \\ c_0 + c_e\{1 - \exp(-h/a_e)\}, & h \neq 0 \end{cases}
\tag{3}
$$

Where c_0 is interpreted as the nugget, c_e is the partial sill, and a_e is the effective range.

Both spherical and exponential variograms were fitted to the empirical variogram for all data sets. Futhermore, a weighted least squares criterion was calculated for each variogram:

$$
Q(\theta \mid z) = \sum_{n=1}^{m} \mid N(h_n) \mid \left\{ \frac{\hat{\gamma}(h_n)}{\gamma(h_n \mid \theta)} - 1 \right\}^2
\tag{4}
$$

The variogram with the lowest weighted least squares criterion was chosen.

Ordinary kriging then uses the chosen theoretical variogram to predict the z-coordinate at a new location by taking a linear combination of the existing observations with weights that are based on the theoretical variogram.

Analysis of the Hospers, Iowa, Data Set

The first data set analyzed was the data from Hospers, Iowa. To aid in the statistical analysis, a clean section of raw data was selected from the point clouds. The selected area is from a section between two dowel baskets lengthwise and between the pavement edges widthwise. The area was chosen to be large as possible without including the features of the dowel baskets and the pavement edges. Since the scan of this area was clear of artifacts such as pedestrian and vehicle traffic, no filtering or cleaning of the data was necessary.

Hospers Pavement Point Cloud

The result is a data set of 5,905 observations that can be used for statistical analysis. Figure 35 contains the contour plot of the pavement data set on the left and the perspective plot on the right. The x- and y-coordinates are measured in meters, while the z-coordinate is measured in millimeters. The perspective plot shows that the pavement increases in height from left to right in the x-direction and the crown that is present in the pavement, which creates an inverted V pattern in the pavement along the y-direction. The plot also shows that one side of the pavement has a greater slope than the other side. Since these trends in the pavement were intentionally created by the paver and prediction is the main goal of the analysis, trends will be removed by fitting a linear model. Then, ordinary kriging will be performed using the residuals that result from fitting the linear model. In order to fit a model to the inverted V pattern, the data was rotated so that the ridge in the pavement was located along the x-axis. Then the inverted V pattern could be modeled using the absolute value of the y-coordinate as an explanatory variable.
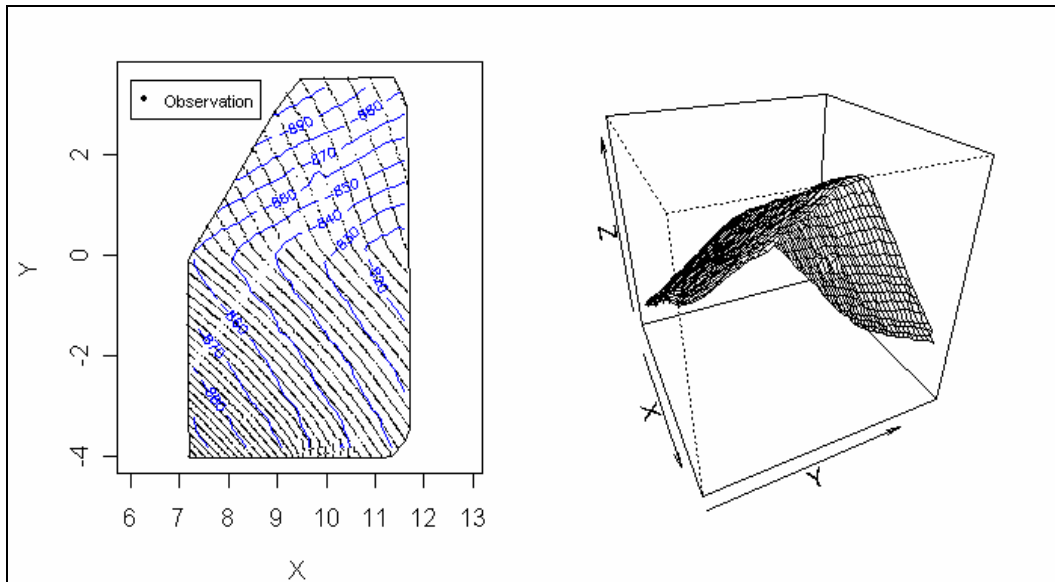
Figure 35. Contour plot and perspective plot of the pavement data

From the trends observed in the perspective plot in Figure 35, the following model was selected:

$$Z = \beta_0 + \beta_1 Y_0 + \beta_2 X + \beta_3 |Y| + \beta_4 Y_1 \tag{5}$$

Where $Y_0 = \begin{cases} 1, & if \ Y \geq 0 \\ 0, & if \ Y < 0 \end{cases}$.

29

Table 1. Parameter estimates for Model 2

Parameters	Estimates
β_0	-949.273
β_1	2.038
β_2	12.259
β_3	-8.405
β_4	-14.101

For a detailed analysis of the process of developing this model, review the description of the kriging analysis in the appendix.

Figure 36 shows the empirical semi-variogram for the residuals for three different types of directional analysis. Starting from the left, the first plot shows the omnidirectional semi-variogram. The omnidirectional analysis gives equal weight to all points in the x and y directions. This semi-variogram does not fit well to any known model. The next plot shows the directional semi-variogram with emphasis given to points in the transverse direction, which is a line drawn across the road. Again, this semi-variogram does not fit any known model. The final plot is a directional variogram for the longitudinal direction, which is a line drawn along an axis in the direction of the paver. Fortunately, this semi-variogram does fit both the spherical and exponential semi-variogram. That the longitudinal direction produces a more predictable model is not surprising, as initial data analysis indicated that the variance of data is smaller when viewed in the axis of the direction of the paver. When the data is viewed transversely, the variance of the data is greater, and the model of the variance is difficult, if not impossible, to predict.
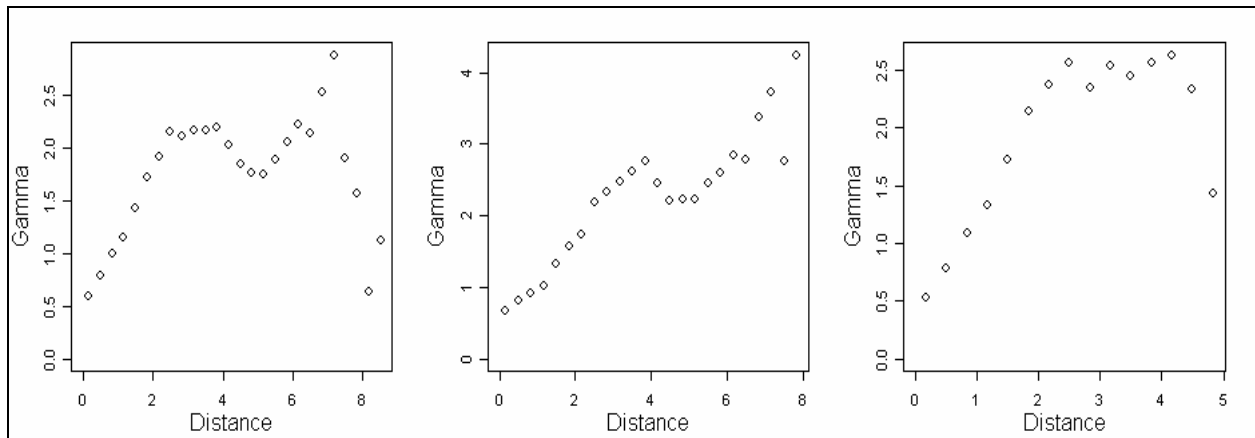
Figure 36. Empirical semi-variogram of the residuals: omnidirectional, transverse, and longitudinal

According to the weighted least squares criterion and Figure 37, the spherical variogram fits the empirical variogram better than the exponential variogram. Next, ordinary kriging was performed using the spherical variogram and another random sample of 2,000 residuals. By choosing another 2,000 residuals from the remaining 3,905 residuals that were not chosen for the

calculation of the empirical variogram, one can assess how well ordinary kriging can predict the height of the pavement by comparing the predicted height to the observed height at locations that were not used to estimate the parameters of the model. The second random sample consisting of 2,000 residuals and their respective locations will be called the validation data set. Predictions and prediction squared errors for the validation data set are shown graphically in the image and contour plots in Figure 38. The squared errors are slightly larger in the lower left corner of the contour plot than in the upper right corner, which is a result of the pavement data being denser in the lower left corner than in the upper right corner. The impact of the number of observations on the squared errors will be examined in more detail in a later section.
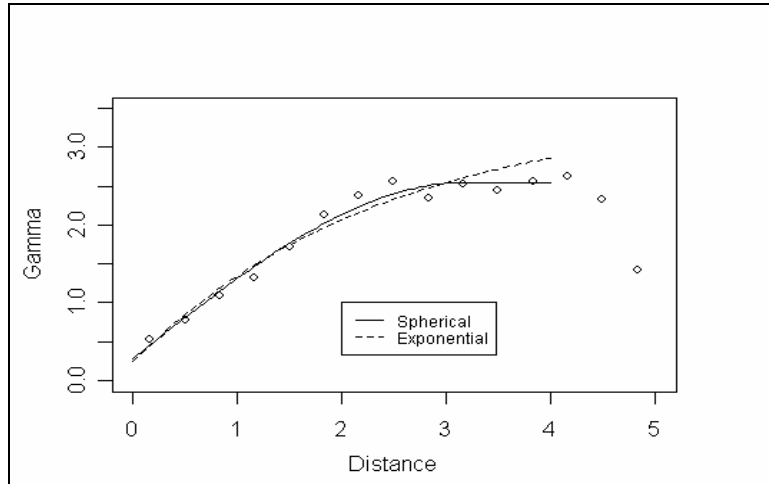
Figure 37. Fitted theoretical semi-variograms
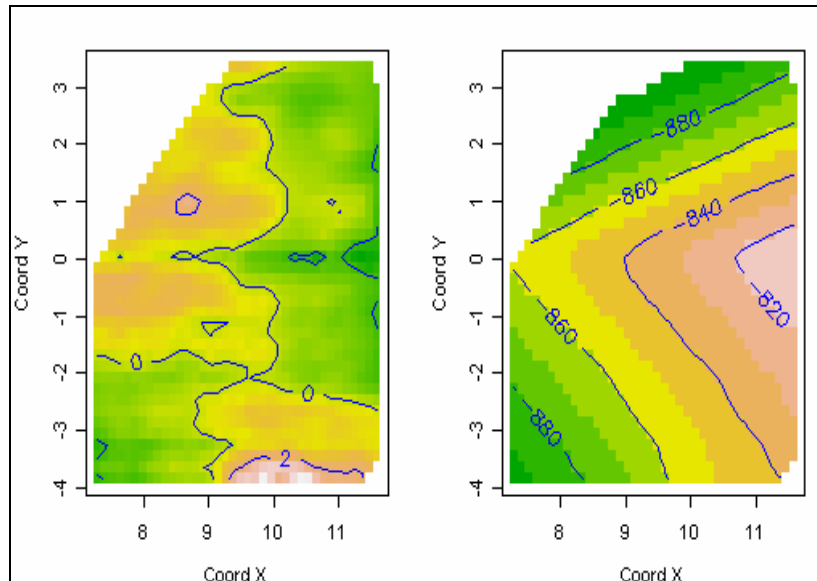
Figure 38. Contour and image plots of predictions for residuals (left) and predictions for pavement height (right)

31

Confidence intervals based on a significance level of 0.05 were then calculated for each location in the validation data set. The predicted height of the pavement consists of the sum of the predicted height and the corresponding predicted residual from the kriging analysis for each location. The 95% confidence intervals were then calculated as follows:

$$p_p(Z, s_i) \pm 1.96\sqrt{\sigma^2_p(s_i)}$$

(6)

Where $p_p(Z, s_i)$ is the prediction of height at location, s_i,

and $\sigma^2_p(s_i)$ is the squared error at location, s_i.

The coverage probability, which is the percentage of confidence intervals that capture the actual observation, is 96.6%. The median of the confidence intervals is 2.45 mm. Moreover, the theoretical prediction mean squared error, which is the mean of the squared errors from the kriging analysis, is 0.402. The empirical prediction mean squared error is 0.437 and is calculated by the following:

$$\hat{\sigma}^2_e = \frac{1}{n}\sum_{i=1}^{n}(Z(s_i) - \hat{Z}(s_i))^2$$

(7)

Since random samples were used for the analysis, the steps described in this section, beginning with generating a random sample of 2,000 observations to create the empirical variogram, were repeated 25 times to better understand the values that could be expected for the coverage probability and the median width of a confidence interval. However, only a spherical variogram was fitted to the empirical variogram for every random sample and used for prediction. There is a possibility that, in some cases, an exponential variogram may have been a slightly better choice. In addition, since the process was repeated only 25 times, the following summary should be treated as a descriptive statement, not an inferential statement. For the 25 repetitions, the minimum and maximum values for the coverage probability were 94.8% and 97.3%, respectively, and the minimum and maximum values for the median width were 2.08 mm and 2.83 mm, respectively.

Hospers Subbase Point Cloud

The subbase data set, which contains 7,698 observations, was rotated and analyzed in the same manner as the pavement data set. As expected, the trends that were discovered in the pavement data can be seen in the subbase data, as shown in Figure 39. However, the trends are less pronounced because the subbase material does not create a surface that is as smooth as the pavement surface.
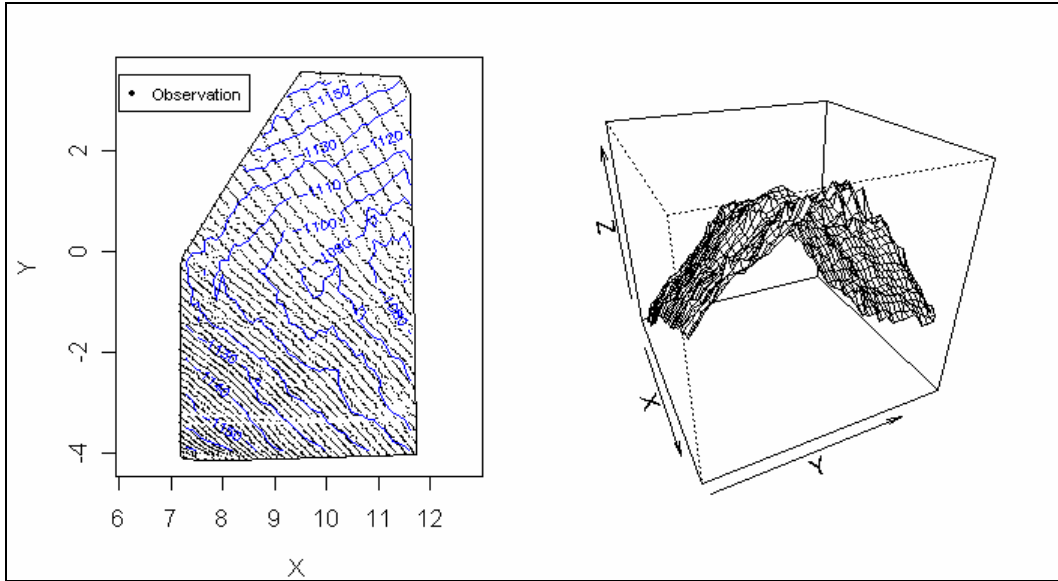
Figure 39. Contour plot and perspective plot of the subbase data set

Since the model in Equation 1 was used to model the trends in the pavement data set, this model will also be used to model the trends in the subbase data set. The ordinary least squares estimates can be found in Table 2, and the contour plot and perspective plot of the residuals can be found in Figure 40.

Table 2. Parameter estimates for Model 2

Parameters	Estimates
β_0	-1201.123
β_1	-7.097
β_2	12.280
β_3	-13.254
β_4	-7.390
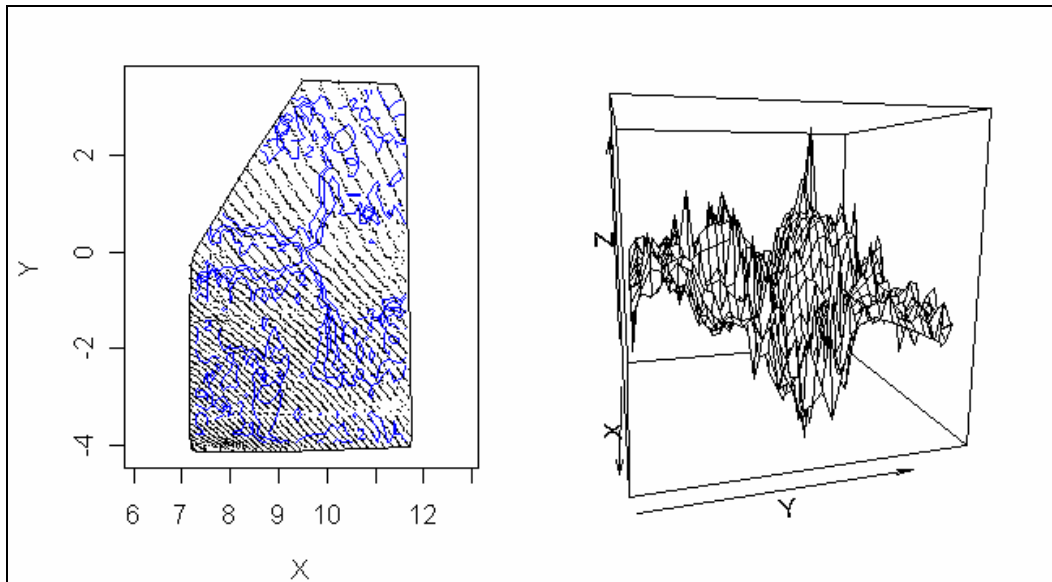
Figure 40. Contour plot and perspective plot of residuals (mm) for subbase

As with the pavement data, the empirical semi-variograms were computed omnidirectionally, transversely, and longitudinally. Again, the longitudinal directional analysis produced the best fit with known models for a semi-variogram.
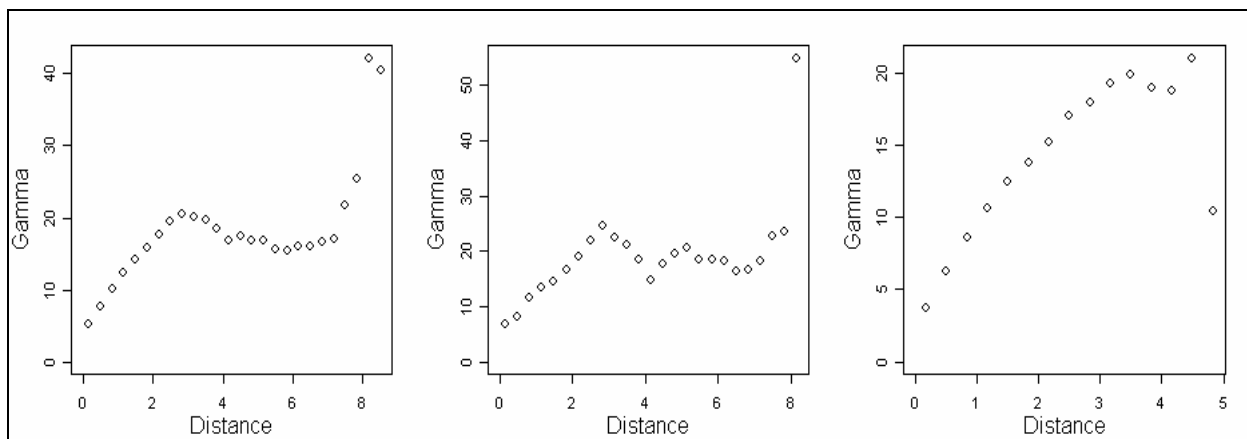
Figure 41. Empirical semi-variogram of the residuals: omnidirectional, transverse, and longitudinal

The best fit for the empirical semi-variogram is the exponential theoretical semi-variogram up to four meters (see Figure 42). For this reason, only data within four meters of the prediction location will be used for estimating subbase elevations.
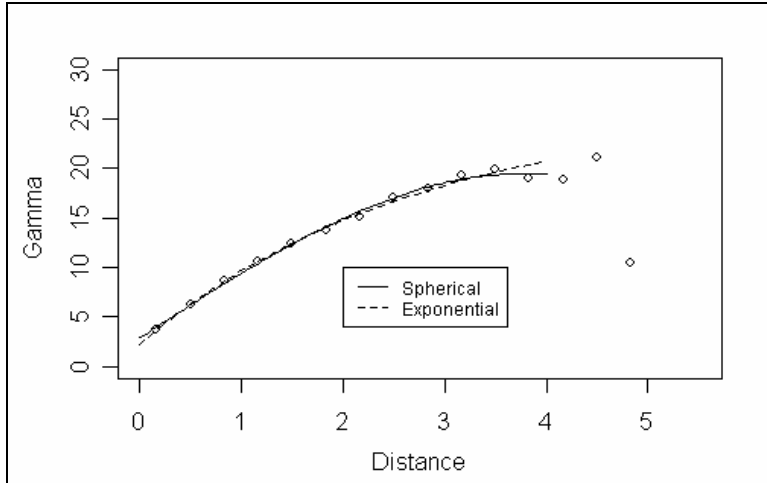
Figure 42. Fitted theoretical semi-variograms

Again, a random sample of 2,000 observations was selected from the remaining observations that were not used to calculate the empirical variogram. Next, ordinary kriging was performed using the exponential variogram. Once predictions were obtained, the 95% confidence intervals were calculated for each location in the validation data set. The coverage probability is 95.9%, while the median of the width of the confidence intervals is 6.98 mm. The theoretical prediction mean squared error is 3.230, while the empirical prediction mean squared error is 2.870. The median width of the confidence intervals for the subbase is larger due to the uneven nature of the subbase when compared to pavement. The contour and image plot of the predictions and squared errors can be seen in Figure 43.
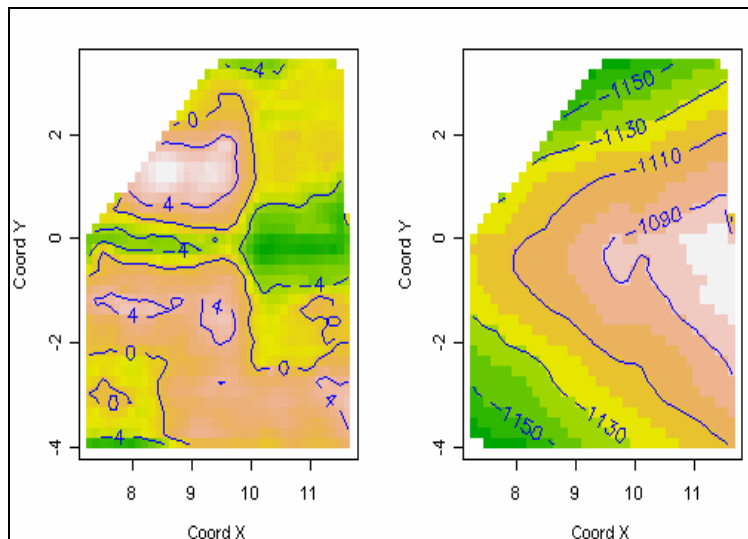
Figure 43. Contour and image plots of predictions of residuals (left) and predictions of subbase height (right)

As with the pavement data, the above process was repeated 25 times, beginning with generating a sample of 2,000 observations to create the empirical variogram. However, only an exponential

35

variogram was fitted to the empirical variogram for every random sample and used for prediction. There is a possibility that a spherical variogram could have a lower value for the weighted least squares criterion. For the 25 repetitions, the minimum and maximum values for the coverage probability were 94.7% and 97.1%, respectively. The minimum and maximum values for the median width were 6.42 mm and 7.70 mm, respectively.

Depth of Pavement

The 2,000 locations from the subbase validation data set were used to predict not only the height of the subbase at those locations but also the height of the pavement. Figure 44 shows the predicted depth (left) and the variance (right).
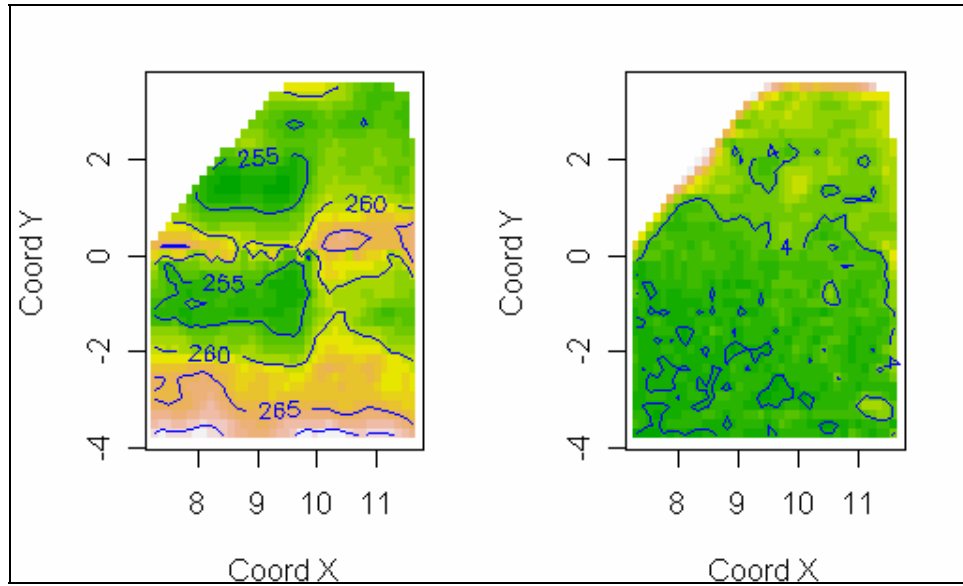
Figure 44. Contour and image plots of predicted depth of pavement (left) and squared errors (right)

Once the predictions and squared errors were calculated for the height of the subbase and the predictions and squared errors were calculated for the height of the pavement, the 95% confidence intervals were constructed as follows:

$$p_p(Z,s_i) - p_s(Z,s_i) \pm 1.96\sqrt{\sigma_p^2(s_i) + \sigma_s^2(s_i)}$$

(8)

Where $p_j(Z,s_i)$ is the prediction of height at location, s_i, for $j = p, s$

and $\sigma_j^2(s_i)$ is the squared error at location, s_i, for $j = p, s$.

The median width of the 95% confidence intervals is 7.46 mm.

Predicted Depths at Tama and Seney, Iowa.

The data sets for Tama and Seney, Iowa, were analyzed in a manner similar to the data at Hospers, Iowa. The details of this analysis are presented in the appendix. In summary, the median of the 95% confidence intervals are 11.27 mm for Tama and 6.957 mm for Seney. Figure 45 and Figure 46 show the predicted depths and squared errors for each project.
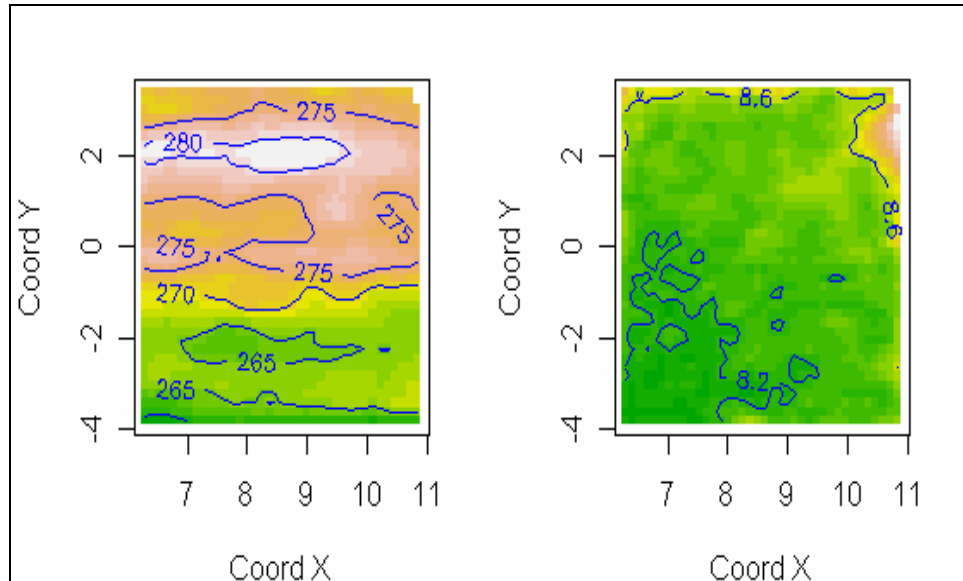
Figure 45. Contour plots of predicted depth (left) and squared errors (right) for Tama, Iowa
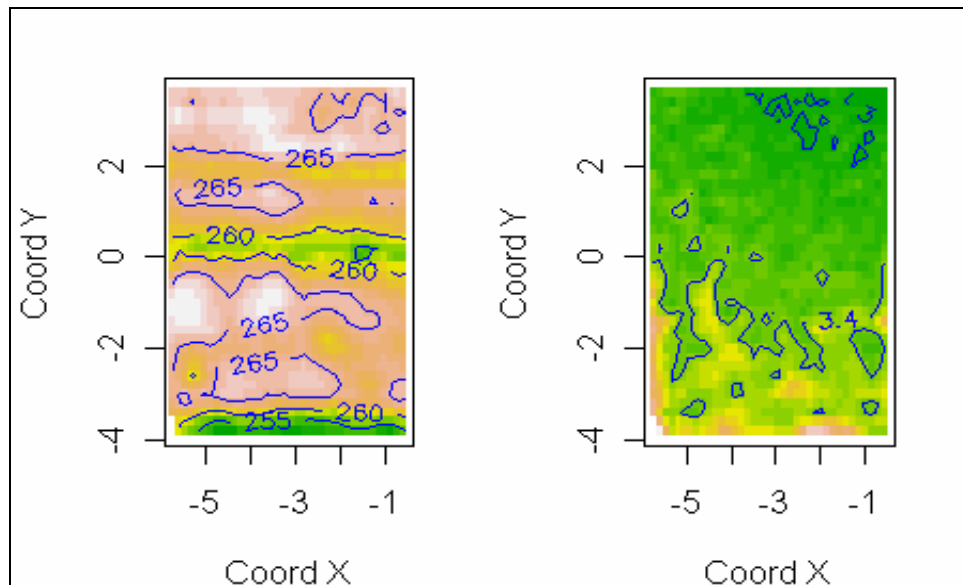
Figure 46. Contour plots of predicted depth (left) and squared errors (right) for Seney, Iowa

Summary of Statistical Analysis

The data analysis described above reveals significant variability in the pavement thickness. Table 3 lists the statistical values for the estimated pavement thickness values. These values are also shown graphically with boxplots in Figure 47. The height of the boxes represents the interquartile range (IQR), which is the difference between the 0.75 and the 0.25 percentile value. This means that 50% of the thickness values fall within the range represented by the box. The line in the box represents the median value and indicates the skewness of the data. The horizontal bars above and below the box represent the minimum and maximum values. The exception is for Seney, because the width of the lower quartile exceeds 1.5 times the width of the IQR. Data below the bar are considered outlier data.

Table 3. Descriptive statistics for the projects

	Hospers	**Seney**	**Tama**
Minimum (mm)	251.5	249.7	256.0
0.25 percentile (mm)	256.7	262.6	265.1
Median (mm)	260.5	265.1	267.8
0.75 percentile (mm)	264.8	266.3	274.5
Max (mm)	276.4	269.0	281.7
IQR (mm)	8.14	3.74	9.42
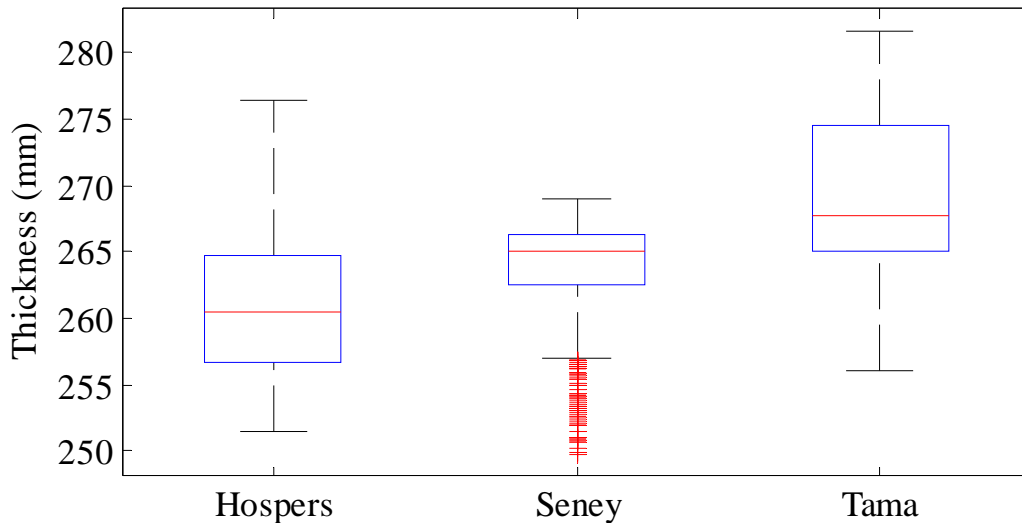
Figure 47. Boxplots of the estimated thickness values

In Iowa, pavement thickness is estimated by taking the mean minus one standard deviation, which means that a contractor's payment is impacted by both average thickness and variance of the thickness value. Table 4 shows the mean, standard deviation, estimated thickness, and design thickness for the three projects. Figure 48 shows the empirical frequency distributions for the three projects. These plots were obtained from the histograms of the thickness data for each project. The vertical lines mark the estimated thickness, which is equal to the mean minus one

standard deviation. Note that Seney had the lowest variance (SD=3.24 mm) while Tama had the highest (SD=5.82 mm). This variance is largely due to the subbase; the subbase material used at Tama was different from the material used at the other two sites. At Tama, the subbase was crushed portland cement concrete with very little fine material, whereas the material used at the other two sites consisted of a smaller aggregate with fine material, which resulted in less variation in the subbase surface texture.

Table 4. Mean and standard deviation of the project data

	Hospers	Seney	Tama
Mean (mm)	261.0	264.1	269.5
SD (mm)	5.19	3.24	5.82
Mean - SD (mm)	255.8	260.9	263.6
Design thickness (mm)	260	260	260
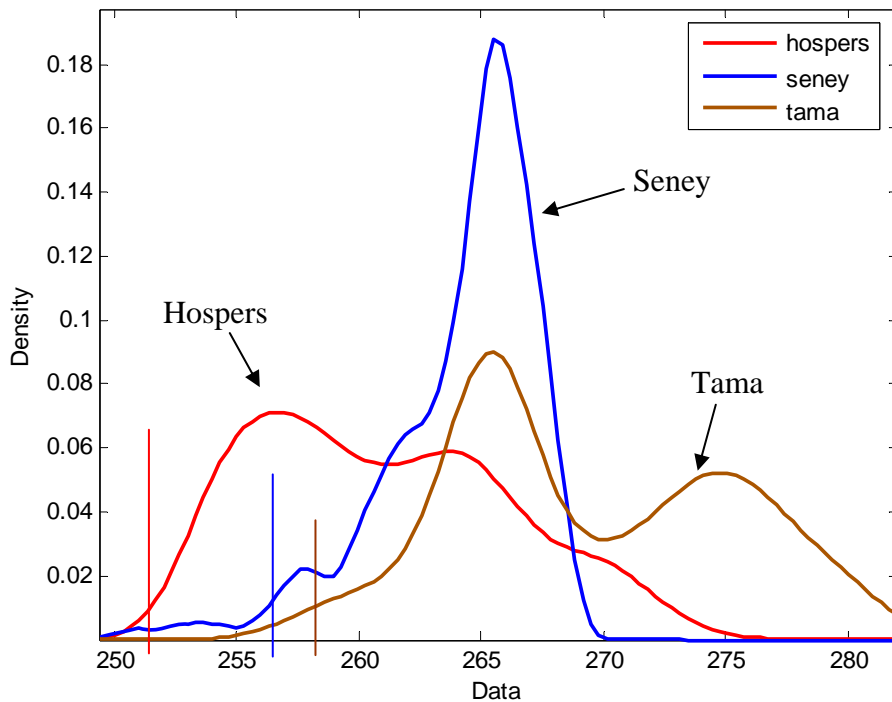
Figure 48. Empirical frequency distribution for pavement thickness at each project

Pavement Thickness Sampling Plan

In Iowa, concrete thickness is estimated by taking core samples. The procedure is documented in Materials Instructional Memorandum 346, "Locating, Drilling, and Evaluating Portland Cement Concrete Pavement Cores." (Iowa Department of Transportation 2005) The pavement is divided into lots, which are sections of the pavement not to exceed 2,000 sq. yd. (1,700 m^2). Each lot is then divided into six equal segments, both longitudinally and transversely, for a total of 36 subsections. Then, a die is rolled twice for each lot to randomly select one of the 36 subsections.

A core is then taken from the center of each selected subsection. The procedure for measuring the length of the core is specified in Materials Instructional Memorandum 347, "Measuring Length of Drilled Concrete Cores," which follows AASHTO T 148.97 (AASHTO 2001). Nine measurements are taken from the core. These nine individual observations are recorded to the nearest 0.05 in. (1 mm), and the average of the nine measurements is expressed to the nearest 0.05 in. (1 mm). This average value is recorded as the length of the core.

The average and standard deviation are calculated for all core samples, and then a thickness index (TI) is calculated as follows:

$$TI = (\overline{X} - S) - T$$

Where:

TI = thickness index for the section

$\overline{X}$ = mean core length for the section

T = design thickness

S = core length standard deviation for the section

This thickness index is used as the basis of payment, in accordance with Section 2301 (Iowa DOT 2001) of the Standard Specifications for the Construction of Highways and Bridges. This payment schedule is shown in Table 5.

Table 5. Payment schedule for portland cement concrete pavement

TI range, in inches (mm)	Percent payment	TI range, in inches (mm)	Percent payment
0.00 or more (0.00 or more)	103	-0.56 to -0.60 (-13.98 to -15.24)	91
-0.01 to -0.05 (-0.01 to -1.27)	102	-0.61 to -0.65 (-15.25 to -16.51)	90
-0.06 to -0.10 (-1.28 to -2.54)	101	-0.66 to -0.70 (-16.52 to -17.78)	89
-0.11 to -0.15 (-2.55 to -3.81)	100	-0.71 to -0.75 (-17.79 to -19.05)	88
-0.16 to -0.20 (-3.82 to -5.08)	99	-0.76 to -0.80 (-19.06 to -20.32)	87
-0.21 to -0.25 (-5.09 to -6.35)	98	-0.81 to -0.85 (-20.33 to -21.59)	86
-0.26 to -0.30 (-6.36 to - 7.62)	97	-0.86 to -0.90 (-21.69 to -22.86)	85
-0.31 to -0.35 (-7.63 to -8.89)	96	-0.91 to -0.95 (-22.87 to -24.13)	84
-0.36 to -0.40 (-8.90 to -10.16)	95	-0.96 to -1.00 (-24.14 to -25.40)	83
-0.41 to -0.45 (-10.17 to -11.43)	94	-1.01 to -1.05 (-25.41 to -26.67)	82
-0.46 to -0.50 (-11.44 to -12.70)	93	-1.06 to -1.10 (-26.68 to - 27.94)	81
-0.51 to -0.55 (-12.71 to -13.97)	92	-1.11 or less (-27.95 or less)	80

As seen from the table, a change of 0.05 in. (1 mm) in the TI results in a change of 1% in the payment. As an example, consider a 1/2-mile (805 m) stretch of road, which represents the typical output of one day of paving. If the width of the road is 8.5 yd. (7.8 m), and the thickness is 0.28 yd. (0.26 m), then daily yield would be 2,124 cu. yd. (1,632 m^3). Although a decrease in

TI of 0.05 in. (1 mm) would result in a yield decrease of approximately 0.5%, the payment will decrease by 1%.

Figure 49 shows an estimate of the empirical frequency distribution of data recorded by laser at Seney, Iowa. The area data is approximately 65 sq. yd. (55 m^2). The empirical frequency distribution was approximated by a 40-item histogram. The values of thickness within this small area vary from 250 mm to 269 mm, with a mean 264.14 mm. The standard deviation is 3.24 mm. If the intent is to pay on the following equation:

$$TI = (\overline{X} - S) - T$$

Then this section of road would have the following:

$$TI = (264.14 - 3.24) - 260 = 0.90 \text{ mm}$$
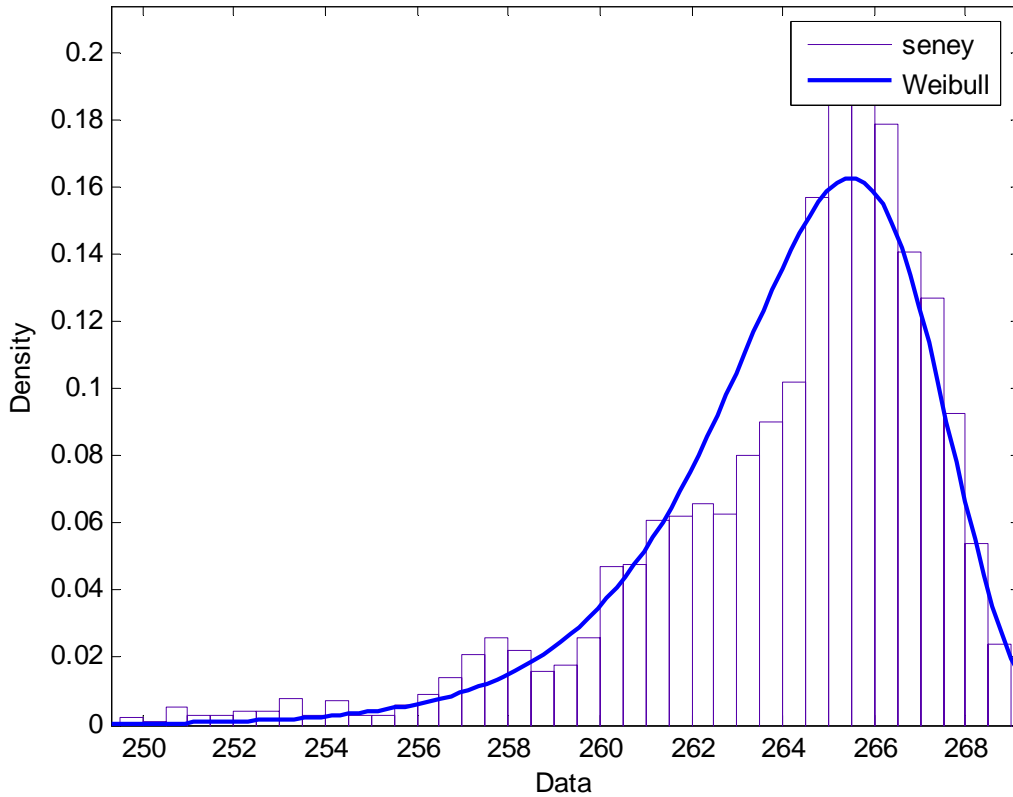
Figure 49. PDF of thickness data for Seney, Iowa

However, in this case, there are 2,000 samples in an area of 65 sq. yd. (55 m^2). For the example of a 1/2-mile (805 m) section of pavement with a core taken every 2,000 sq. yd. (1700 m^2), only four cores would be taken. In order to examine the likelihood that those four samples represent the actual value of the TI, one can examine the empirical frequency distribution of the Seney data at various sampling densities. Assuming that the statistical characteristics for the 1/2-mile

section of road are the same as those of Figure 49, the empirical frequency distributions for various sampling densities can be approximated using the 2,000 data points from the Seney project.

In Iowa, the minimum number of cores required to calculate TI is ten. A bootstrapping method was used to generate the empirical frequency distribution of a ten-point sample. Ten samples were randomly drawn with replacement from the set of 2,000. Once the ten samples were chosen, the TI was calculated. This process was performed 10,000 times, and the results are plotted in the empirical frequency distribution in Figure 50. TI ranged in value from -7 to 6 mm. This would represent a payment range from 97% to 103%. Ninety-five percent of the predicted values for TI are between -3 mm to 4.3 mm, which represents a payment range of 100% to 103%. There is no payment incentive for values of TI above 0. The average value of TI was 1.1 mm, which represents a payment of 103%. These data are summarized in Table 6.
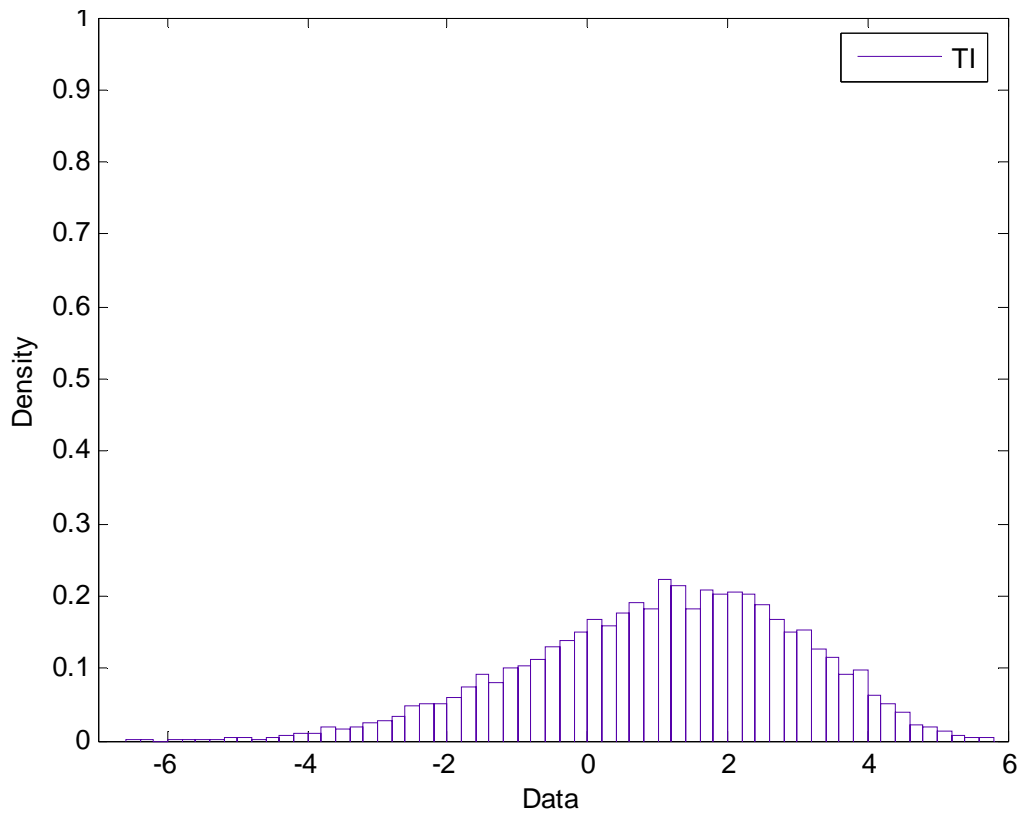
Figure 50. Empirical frequency distribution for a 10-point TI estimate

Table 6. Mean, variance, and range of TI data vs. sample size

Points	Mean	Var.	95% band	Lower band	Upper band	Payment range	Difference
10	1.0508	3.6836	7.2444	-2.9714	4.273	97-103%	6%
50	0.9445	0.7341	3.2801	-0.7700	2.5101	101-103%	2%
100	0.9027	0.3795	2.4133	-0.3202	2.0931	101-103%	2%
170	0.9119	0.2167	1.8595	-0.0544	1.8051	102-103%	1%

Figure 51 shows the empirical frequency distribution for a 50-point sample. When the sample size is increased from 10 cores to 50, the variance and range of the data decreases. At 50 samples, the range is from -2.5 to 4 mm, which represents a payment range of 101% to 103%. Ninety-five percent of the data lie in the range of -0.77 to 2.5 mm (102%–103% payment).
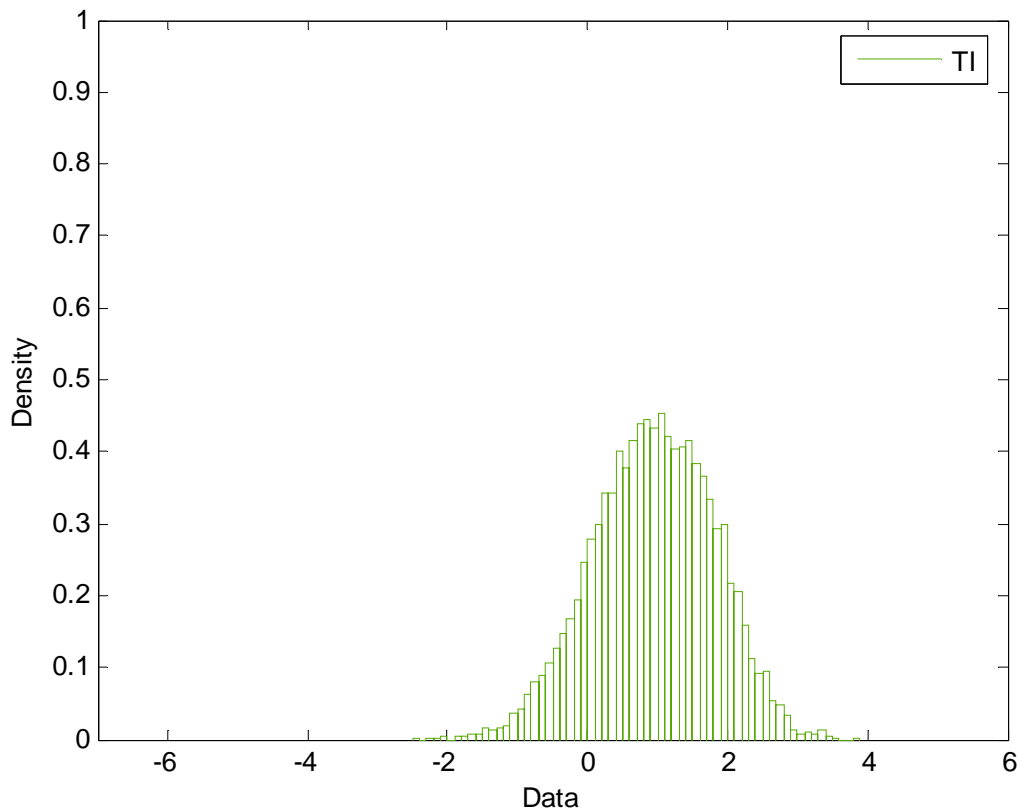
Figure 51. Empirical frequency distribution for a 50-point TI estimate

Figure 52 shows the empirical frequency distribution for a 100-point sample. Again, the variance and range of the data decrease. At 100 samples, the range is from -1.5 mm to 3 mm, which represents a payment range of 101% to 103%. Ninety-five percent of the data lie in the range of -0.32 mm to 2.09 mm (102%–103% payment).

Figure 53 shows the empirical frequency distribution for a 170-point sample. Again, the variance and range of the data decrease. At 170 samples, the range is from -1 mm to 2.6 mm, which

represents a payment range of 102% to 103%. Ninety-five percent of the data lie within a range of -0.054 mm to 1.89 mm (102%–103% payment). Figure 54 shows an overlay of the various empirical frequency distributions. If the goal is to estimate TI at an accuracy of +/-1 mm, then 170 cores would be needed at Seney. The data for Tama and Hospers were similarly analyzed, with the results summarized in Figure 55, Figure 56, and Table 6. The project with the lowest standard deviation (Seney) also happens to be the project with the highest required number of samples. This may seem counterintuitive; however, further analysis did show that the estimates for mean and standard deviation are not independent.
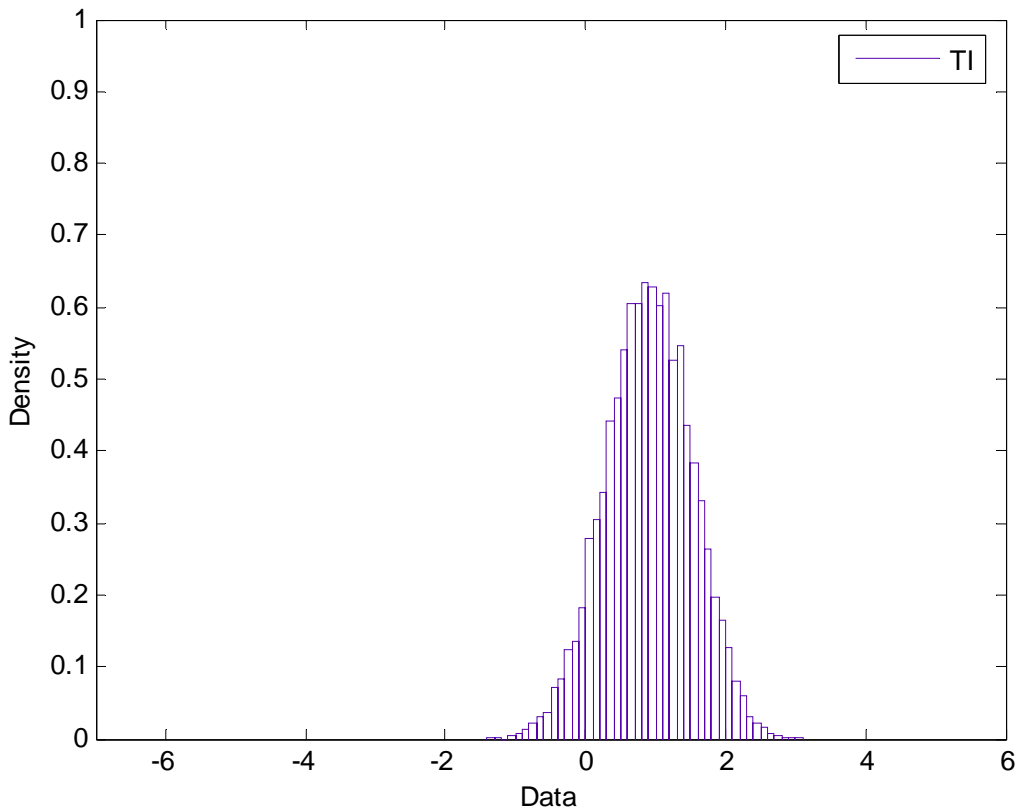
Figure 52. Empirical frequency distribution for a 100-point TI estimate
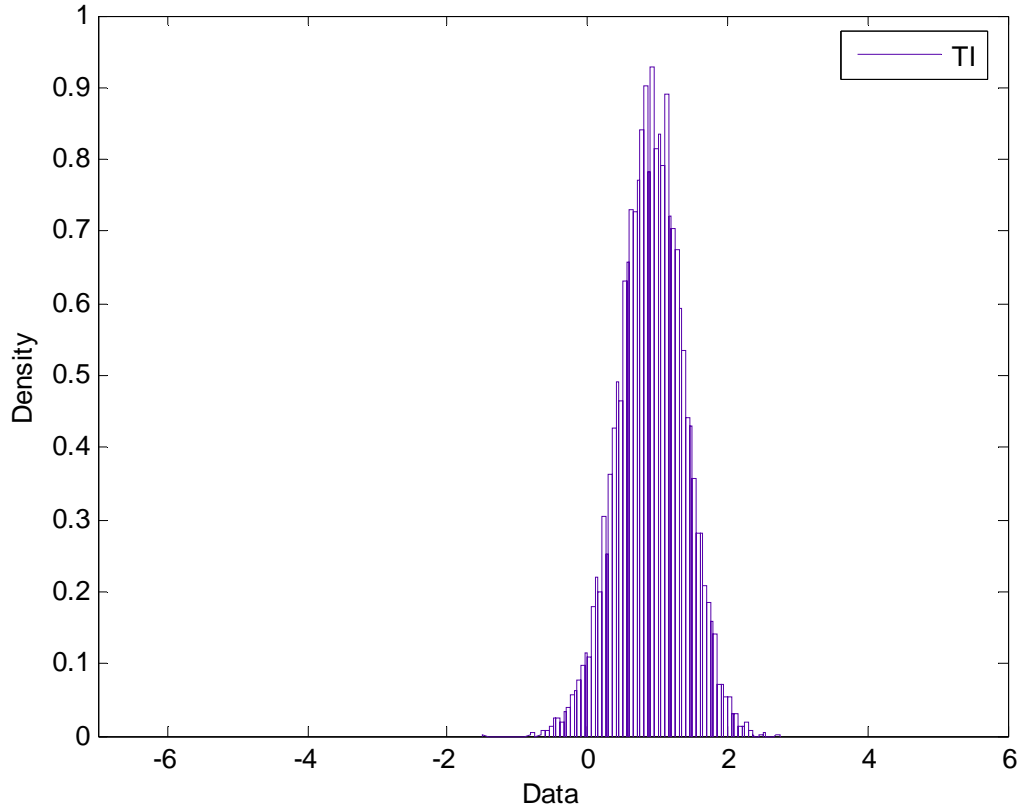
Figure 53. Empirical frequency distribution for a 170-point TI estimate
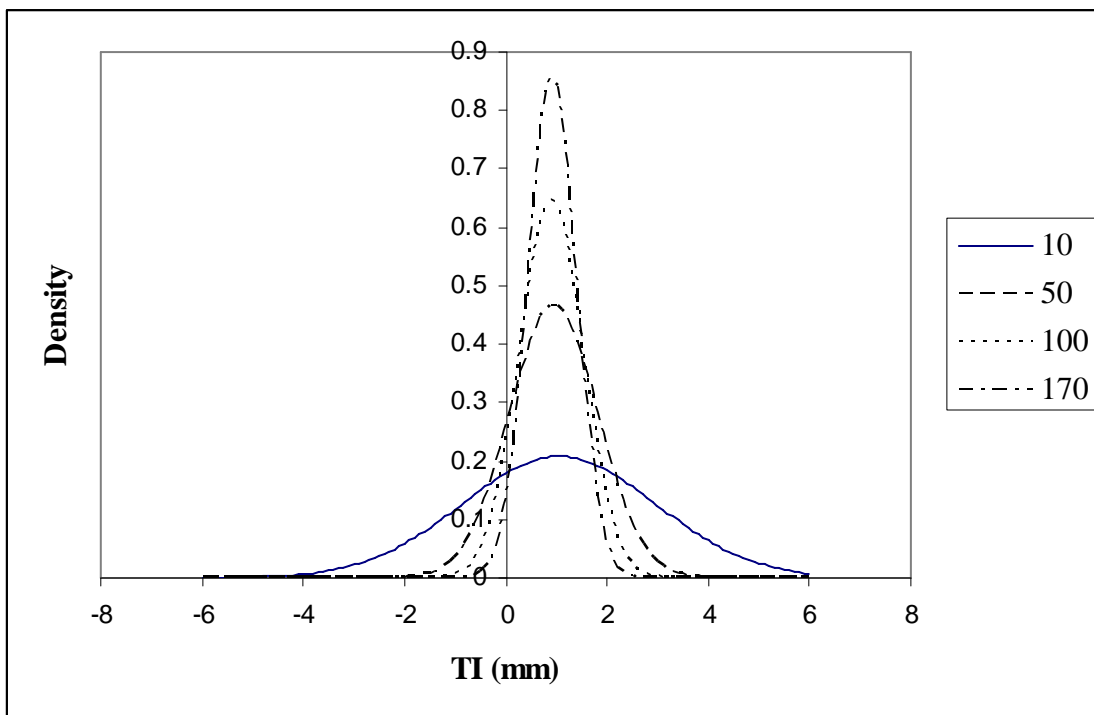
Figure 54. Overlay of the empirical frequency distributions at various sampling densities
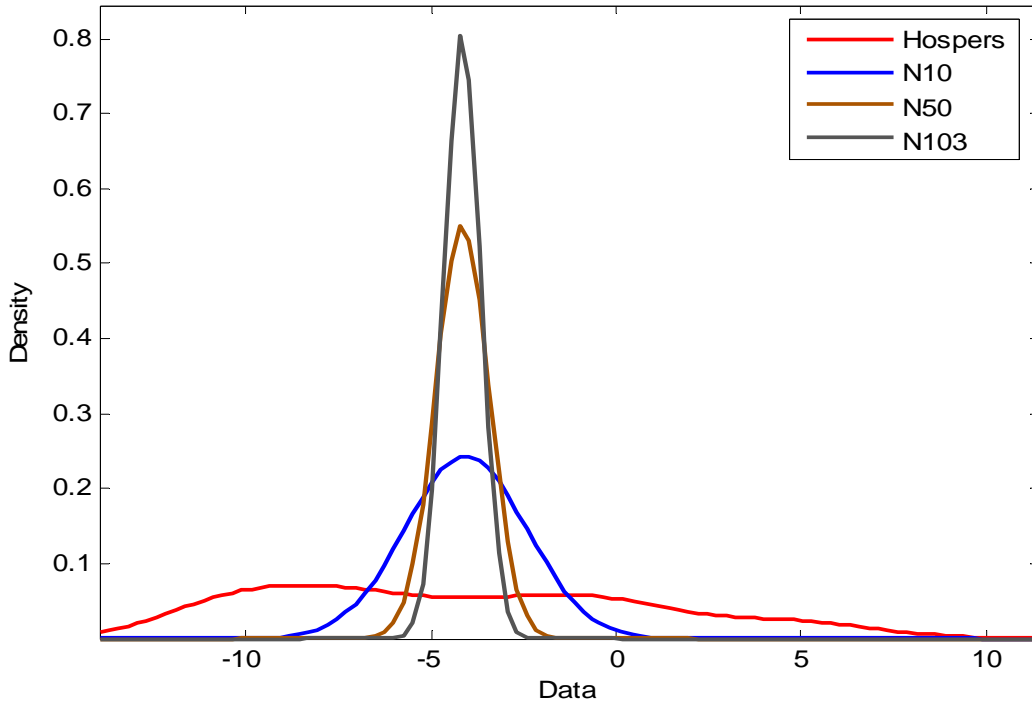
Figure 55. Overlay of empirical frequency distributions at various sampling densities for Hospers
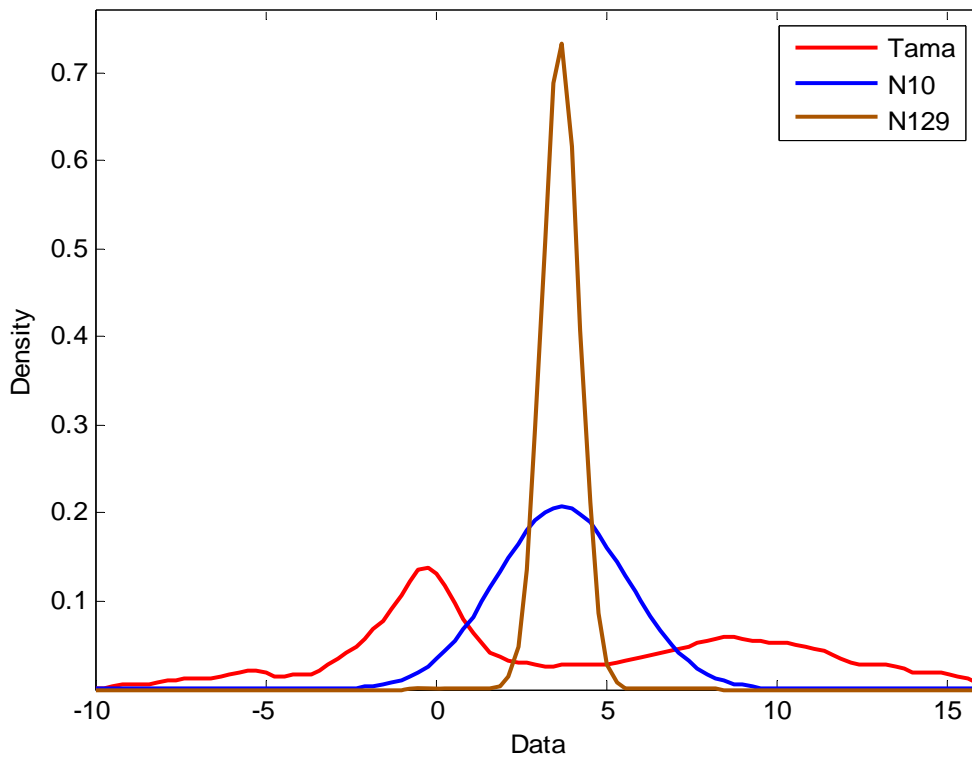
Figure 56. Overlay of empirical frequency distributions at various sampling densities for Tama

Table 6. Summary of required sampling densities

Project	Number of samples	95% band
Seney	170	1.8
Hospers	103	1.9
Tama	129	2.1

Sampling Plan

If the goal is to calculate TI close to the actual value (0.90 mm), then the coring method has serious shortcomings. Even at a sample size of 170 cores, 95% of the expected values range from -0.05 mm to 1.89 mm. Since there is no payment incentive for TI values above 0, there is little impact here on payment. At lower TI values, a 170-core sample could still produce a payment difference of +/- 1%.

Summary of the Laser Scanning Method

A thorough investigation of the use of laser scanning was conducted to assess its viability as an NDE technique for determining concrete pavement thickness during the paving operations. A stationary Leica Geosystems 3600 laser scanner was implemented in a fixed mode on the shoulder of the road. Laser scans were taken on three different projects and for each project involved one scan in front of the paving train and one behind. Filtering algorithms were created to process the image and leave a clean point cloud image of the subbase and concrete surface. This was followed by rigorous statistical analysis, which involved ordinary kriging. It was found that sites that used larger aggregate for the base experienced higher thickness variances. Further discussions with the subcommittee revealed that a more suitable subbase model would be based on the top surface of the aggregate as opposed to an average. Implementing this assumption will reduce the thickness variability. A sampling plan revealed that there are inherent shortcomings with the current sampling plan. Even with 170 core samples, there could still be a payment difference of +/- 1%. Overall, laser scanning appears to have merit; further research on the use of lasers should include building a prototype system complete with coordinate control for each of the two scanners that would be needed.

ALTERNATIVE NDE TESTING METHODS FOR WET CONCRETE

The research team brought two other NDE techniques to the attention of the technical committee members assigned to this project. For one, ultrasound uses sound waves to penetrate through the wet concrete, reflect off the base, and return to the receiver. This method is based on the time it takes for the acoustical wave to travel to the base and back. The eddy current method uses a coil with changing current to detect a metal plate situated on top of the base through a change in impedance and reactance portion. Both of these techniques and findings are provided in the following two sections.

Ultrasonic Method

The first NDE method that was investigated was ultrasound. This method is based on the idea that a sound wave propagating through a medium (wet concrete in this case) will reflect off a dissimilar object. In theory, if the sound waves can penetrate through the pavement with sufficient energy, then the dissimilar material of the subbase will reflect that wave back to the surface of the pavement. If the speed of sound in wet concrete is known, then the time elapsed between transmission and detection of the sound wave can be used to calculate the thickness. Although there was reason to believe that ultrasound would propagate well through wet cement, there was concern that the addition of aggregate to the cement paste would cause significant scattering of the signal and introduce significant noise. However, the cost of testing the method was low and the potential benefits where high, so the decision was made to proceed with a proof-of-concept test. Figure 57 shows the concept of the system. As the figure suggests, the probe would need to be in direct contact with the surface. This could be achieved by placing the probe on the metal pans behind the paver, as shown in Figure 58; having metal between the probe and the pavement would not absorb significant energy from the passing ultrasonic waves.
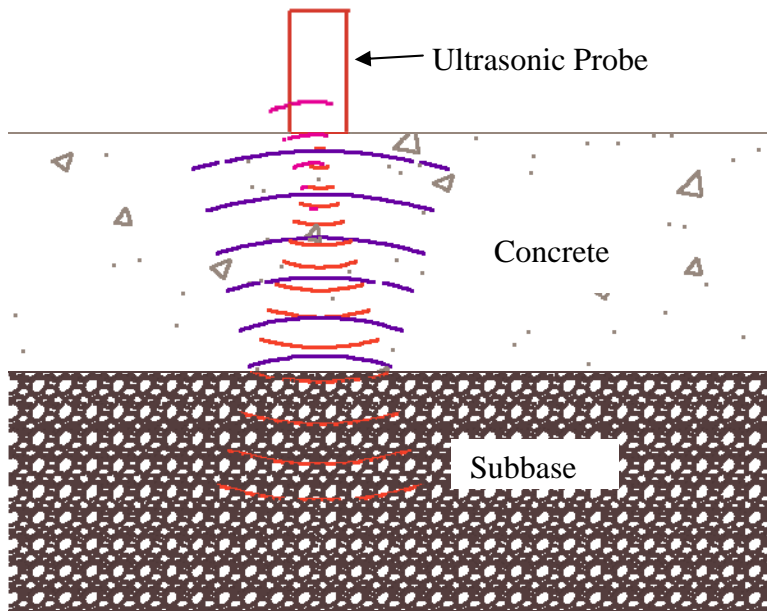
Figure 57. Application of ultrasound for measuring concrete thickness.

Figure 58. Possible location for ultrasonic contact sensor

Experimental Plan

To test the concept, a simple experiment was developed. The plan was to use two ultrasonic probes: one to transmit the signal on one side of the sample and the other to detect the signal on the other side. This setup could demonstrate the viability of detecting the ultrasonic wave after it

passes through wet cement. If successful, another test was to be performed that measures the reflected wave off the aggregate subbase. If unsuccessful, there would be no reason for any further tests. Figure 59 shows a drawing of the experimental test rig, and Figure 60 shows a photo from the test. There are holes in the side of the mole so that the ultrasonic probes are in direct contact with the test sample.
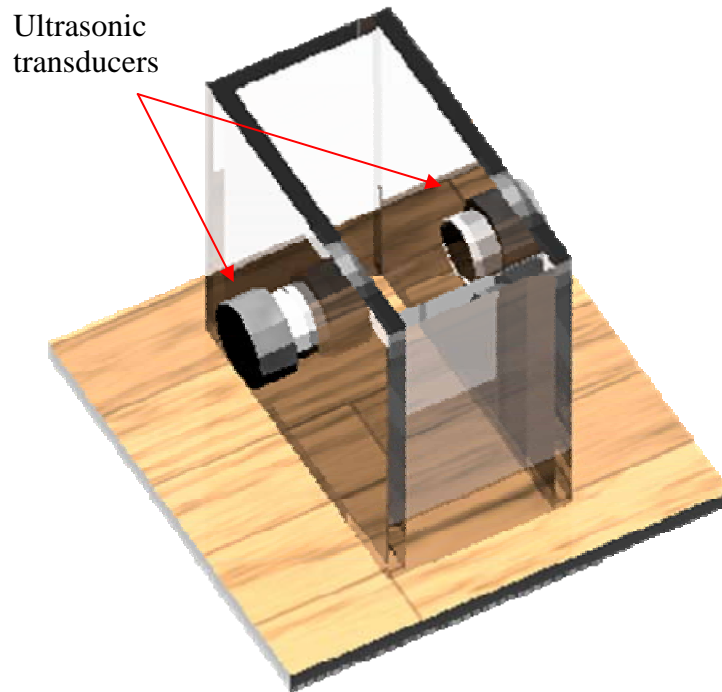
Figure 59. Experimental setup for ultrasonic test
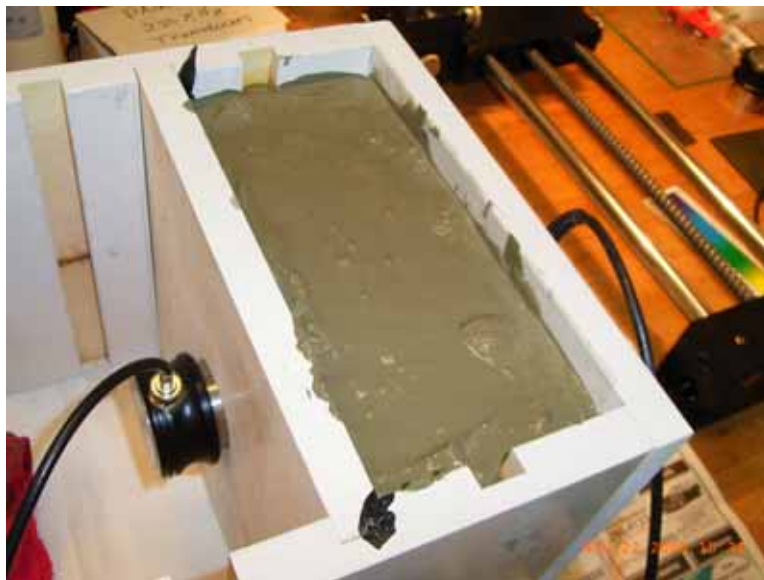
Figure 60. Ultrasonic test

Ultrasound Test Results

The this experiment, a pair of 100 kHz ultrasonic probes were used to transmit and measure the signal through four inches of wet concrete paste (i.e., there was no large aggregate in the mix). Based on difficulties detecting the signal at this level, further experiments where stopped. If signals cannot be detected with a probe mounted on each side with cement paste, then the odds of detecting a reflected wave from an aggregate subbase are low. To make this method viable, a barrier would need to be placed between the pavement and the subbase that would better reflect the ultrasonic wave. If a barrier is to be placed under the subbase, then other techniques that are less sensitive to the aggregate may be more effective. One such method is using electromagnetics with a conductive barrier placed between the pavement and the subbase. Since the conductivity of wet concrete and aggregate are much lower than that of a metallic barrier, an electromagnetic-based system would be insensitive to the physical properties of the concrete mix. For this reason, the follow-up experiment used an electromagnetic technique known as the eddy current method.

Eddy Current Method

Eddy current measurement is a widely used NDT method that can detect conductive materials. In eddy current testing, a coil of wire is powered with an alternating voltage source (Figure 61). As a result, the coil produces a magnetic field. The magnetic field generates eddy currents in conductive materials that in turn produce a magnetic field. This magnetic field affects the impedance of the coil of wire. Since the proximity of the conductive material to the coil, the type of material, and the thickness of material all impact the coil impedance, eddy current inspection techniques have been used to search for subsurface defects in metal.
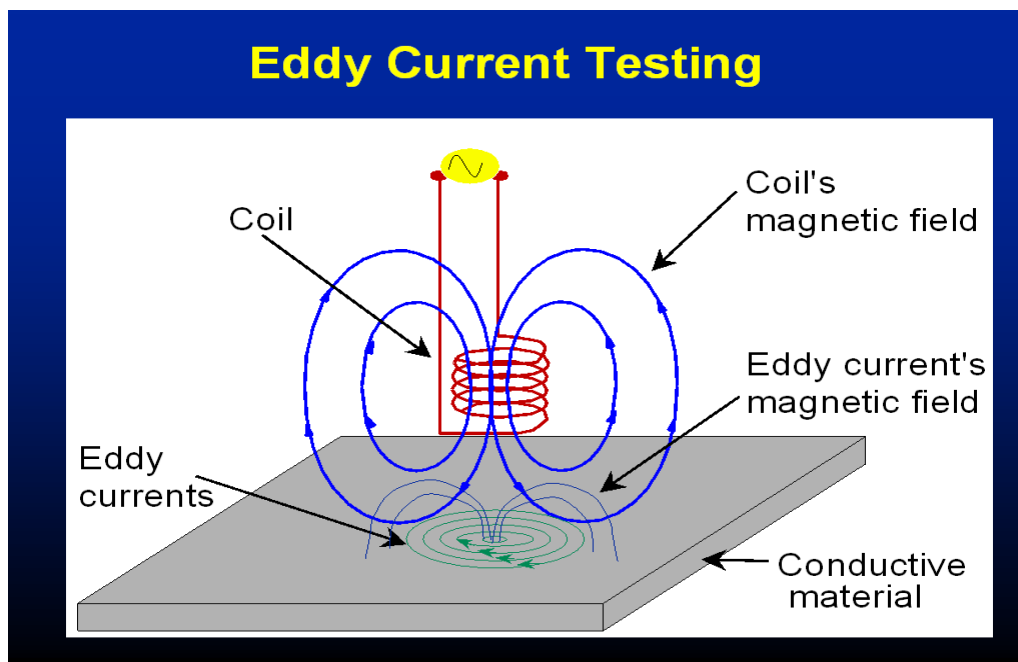
Figure 61. Eddy current testing (Euro NDT Ltd. 2006)

A literature review reveals that this or a similar technique is currently being used to determine the location and depth of joint dowel bars in concrete. This method is useful for determining precisely where to saw cut the concrete for crack control. The Kansas DOT funded a project that used a commercially available rebar detector to measure the position of dowel bars (DeVault and Miller 2005). However, no consideration was made for determining concrete depth. The electromagnetic device used in this research project was a Kolectric Covermeter (Kolectric 2006), which costs less than $2,800. The MIT Scan-2 device (Yu and Khazanovich 2005) can also be used to measure the orientation and depth of a rebar in concrete roads (see Figure 62). Figure 63 shows a simpler device, manufactured by Zircon (Zircon 2006), which costs under $200. Some progress in using this technique is being made. Further research is required to use either the MIT Scan device or the Zircon device to determine concrete pavement thickness.

Figure 62. MIT Scan-2 uses magnetic pulses to measure the depth of dowel bars

Figure 63. Zircon MT6 measures depth of metal to 6 inches +/- 1 inch

Eddy Current Testing for Concrete Thickness

Since concrete is a non-conductive material, an energized coil does not create eddy currents, and consequentially the eddy current inspection technique cannot detect concrete. However, if a conductive material is placed on the bottom of the concrete, an eddy current inspection technique can detect the plate. Additionally, the concrete is not an effective barrier to electromagnetic energy, which makes the concrete invisible to eddy current inspection. The result is that the eddy current system can measure the distance to a conductive metal plate. Whether wet concrete, dry concrete, or air stands between the coil and the conductive plate, the medium has very little effect on the measurement. These reasons make eddy current inspection an attractive technique for nondestructive concrete thickness measurement when a conductive plate is available for the bottom of the concrete pavement. As a result, a small experiment was performed to test the technique.

Experimental Plan

Figure 64 shows the conceptual setup for using an eddy current sensor for concrete paving. A coil is placed directly on the surface of the pavement and energized with an alternating current power source. Whether the concrete is wet or dry makes no difference in the measurement. The figure shows two separate tests. On the left is a coil on the pavement without a conductive plate placed under the pavement. Since the pavement and subbase have very low conductivity, an eddy current cannot be induced into the material, and the resulting impedance measurement of the coil will be similar to that of the coil impedance measured in air.

On the right is the same coil placed on the top of the pavement with a conductive plate placed on the bottom. Assuming that the coil's field strength is strong at the depth of the conductive plate, an eddy current is induced into the plate and the plate then generates its own magnetic field. The result is a change in the real impedance of the coil, which corresponds to the amount of power absorbed by the plate. The amount of real power absorbed is a function of field strength and frequency. The field strength is held constant for the measurement, but decreases as the distance between the coil and plate increases. There is also a change in the imaginary impedance of the coil. The imaginary portion of the impedance is a measure of inductance, a phenomenon associated with magnetic fields. The source of the magnetic field is charge-in-motion, or current. If the current varies with time, the magnetic field varies with time. A time-varying magnetic field induces a voltage in any conductor that is linked by the field. Magnetic fields store energy, and this energy can be returned to the circuit. The presence of a conductive plate in the magnetic field changes the permeance of the space in which the magnetic field exists. The change in permeance also changes the strength of the magnetic field, which changes the amount of energy stored in the field. This change in field strength is proportional to the inductance of the coil, which is proportional to the imaginary component of the coil impedance.
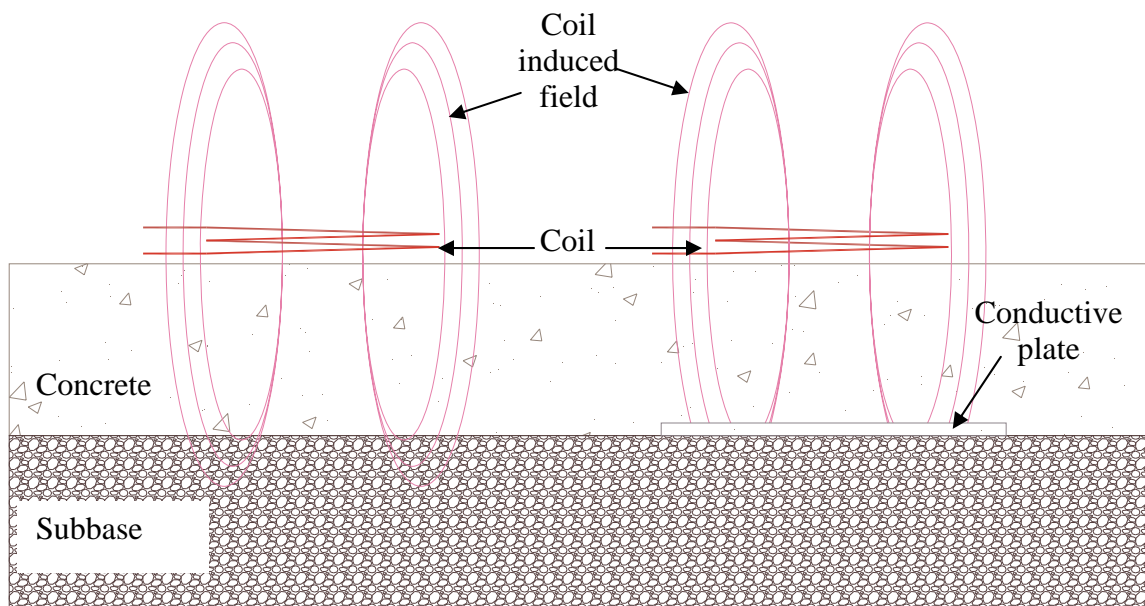
Figure 64. Eddy current sensor for concrete thickness measurement

A test of this concept was performed by using readily available materials. Figure 65 shows the coil used for the test. This coil has an outer diameter of 6" and an inner diameter of 4 7/8". As a rule of thumb, the depth penetration of an eddy current sensor is roughly equal to the diameter of the coil. In this case, the penetration is expected to be around 5". For this reason, an upper limit of 4" of concrete was used for this experiment.

Figure 65. Test coil for eddy current test

The test was performed using an 18" x 18" box with a 12" x 12" x 1/4" 6061 aluminum plate. Figure 66 shows the box with the aluminum plate prior to pouring the concrete. The impedance of the coil was measured over a range of 50 to 5,000 Hz at the following thicknesses for wet concrete: 0", 1", 2", 3", 3 7/8", and 4 1/2". An additional measurement was taken at 4 1/2" after 24 hours of curing time. The results of the wet concrete measurements are shown in Figures 68 and 69. Both the real and imaginary impedance show significant change with thickness: the sensitivity decreases as the thickness approaches 4 1/2", which is close to the expected useful depth of the test coil.

Additional measurements where taken of the coil in free air and of the 4 1/2" concrete sample after 24 hours of curing. These measurements are shown in Figures 70 and 71, along with the wet concrete thickness measurements. All of these measurements were taken at 5,000 Hz. There are several items to note from these figures. First, the sensitivity of the coil diminishes as the depth increases, with the change becoming small as the depth approaches the coil diameter. Second, the measurement of the 4 1/2" sample varies little between the wet and dry tests. This supports the hypothesis that the coil impedance is related to the conductive plate, and not the concrete. In fact, the real impedance increased slightly and the imaginary impedance decreased slightly, which could be due to shrinkage of the concrete. Third, the measurement of the impedance of the coil in free air is close to the measurement at 4 1/2". There was a slight change, which indicates that the conductive plate was at the edge of the magnetic field. This hypothesis is consistent with the expectation that the usable depth of the coil is approximately equal to the coil diameter.

Figure 66. Test box with aluminum plate prior to pouring concrete
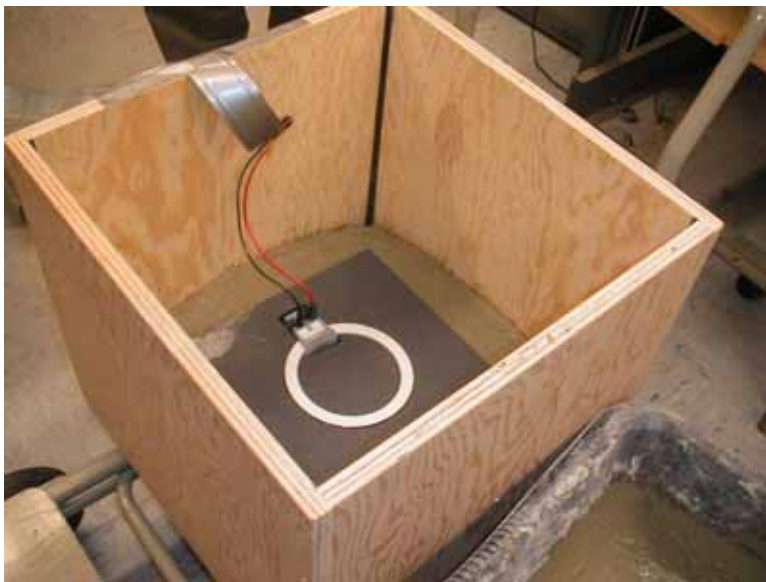
Figure 67. Photo from eddy current test of wet concrete
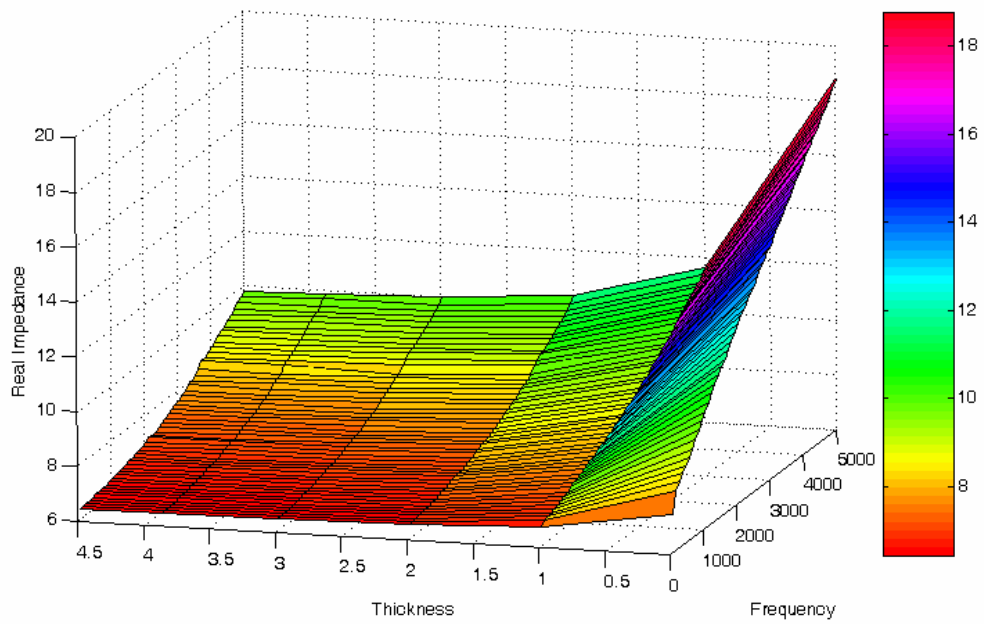
Figure 68. Real impedance of coil vs. frequency and thickness
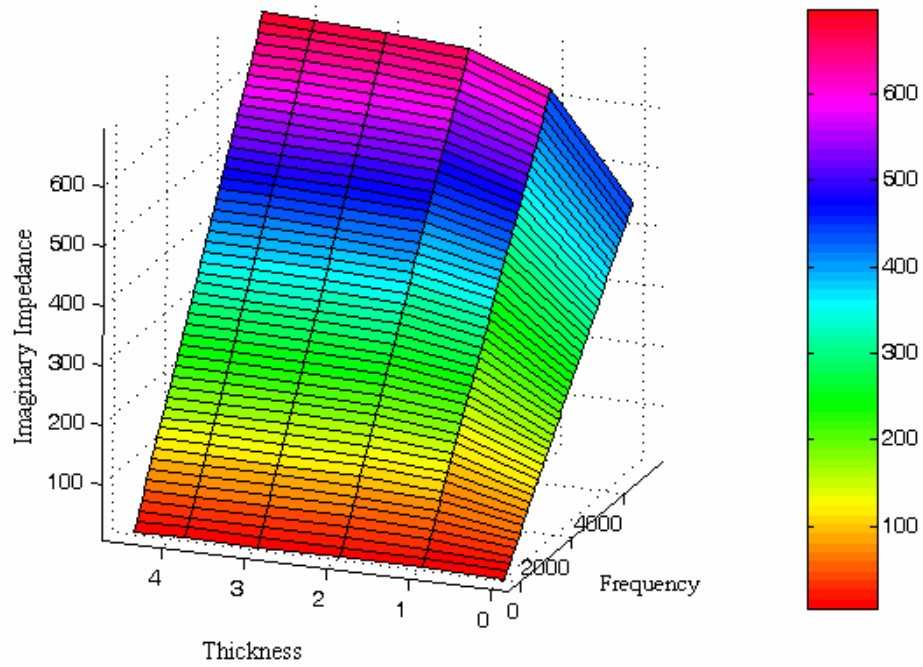
Figure 69. Imaginary impedance of coil vs. frequency and thickness
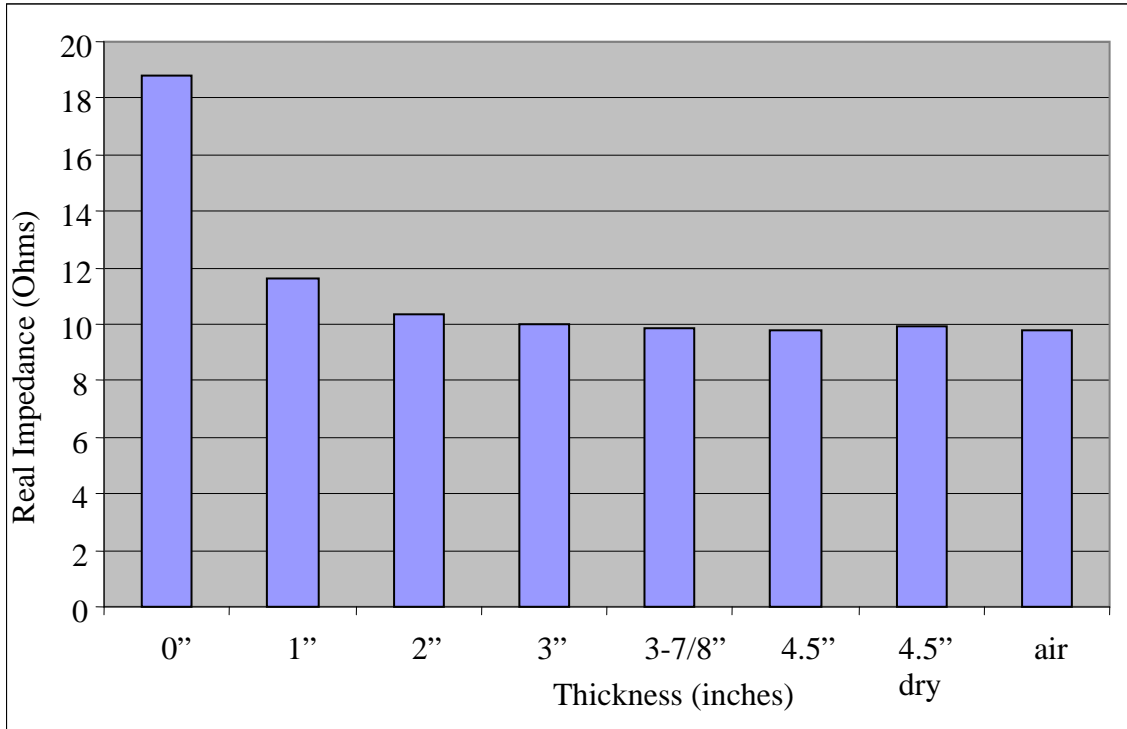
Figure 70. Real impedance vs. thickness at 5,000 Hz
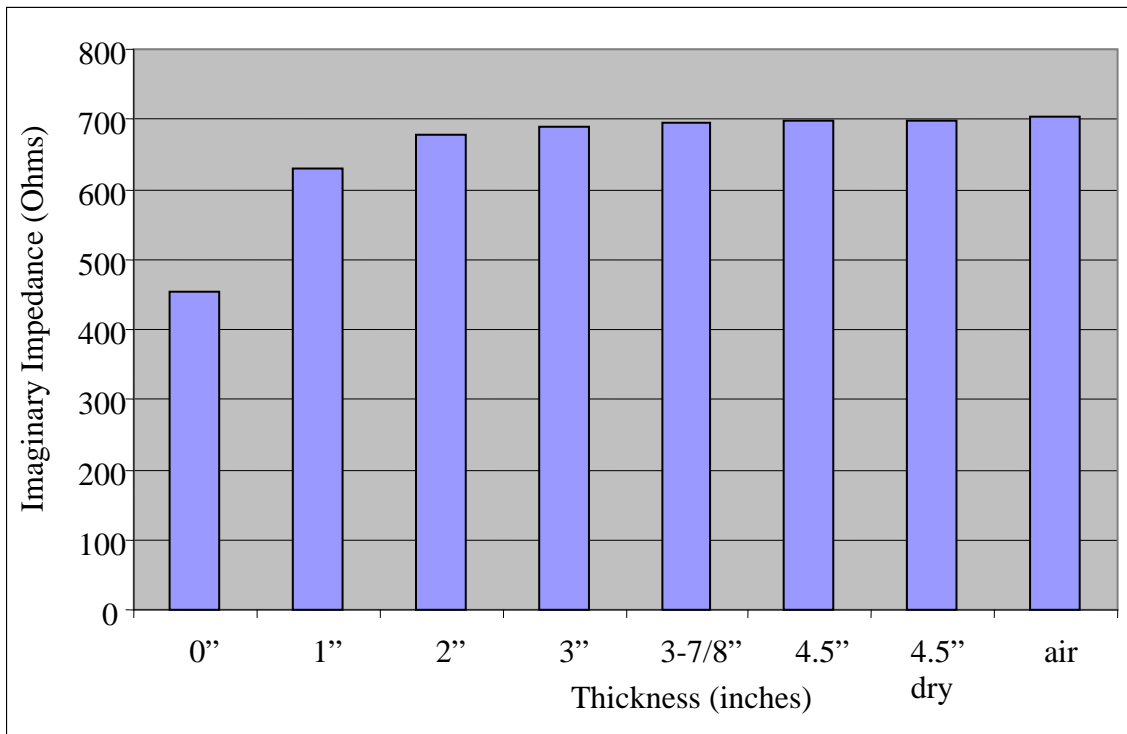
Figure 71. Imaginary impedance vs. thickness at 5,000 Hz

Conclusions and Recommendations for Eddy Current Testing

Eddy current testing is a common NDE technique that is used to examine conductive materials. It was expected that the method would be able to detect the 1/4" aluminum plate at the test depths. The experiment confirmed this hypothesis, as well as the expectation that concrete, whether wet or dry, is largely invisible to the coil. The method should be scalable to realistic pavement depths by using a coil with a diameter larger than the thickness of the concrete. To make this method practical to concrete paving, further work is needed. A fairly large aluminum plate was used for this test. Smaller and thinner plates could be used, but further testing would be required to find the minimum size and thickness.

In the field, a conductive material would have to be placed under the concrete. One idea is to add these plates to the rebar cages that are typically placed at lateral joints prior to paving. A thickness measurement at each lateral joint would provide more data than currently collected through core samples, and measurements could be taken on the wet concrete, providing on-the-fly thickness monitoring. Further testing will be required to determine the size and thickness of the plate. Also, the eddy current sensor will detect rebar cages, so the plate would need to be some distance from the rebar. This distance would also need to be verified through experiment.

Some calibration would be required. Eddy current testing is largely insensitive to concrete and to the aggregate subbase. In the worst case, it is expected that calibration would need to be performed each day. This could be done by taking a manual depth measurement of a few plates. The accuracy of the measurement will depend on many factors, including coil diameter, coil impedance, power supply frequency, and the size of the conductive plate. Further testing is required to determine the conditions necessary to achieve the desired accuracy.

Based on the findings of this small experiment, we believe that the eddy current sensor shows promise for measuring the thickness of concrete pavement.

RECOMMENDATIONS AND CONCLUSIONS

It appears that there are two viable approaches for measuring concrete pavement thickness during the paving operation. Laser scanning has proved to be a reliable technique in terms of its ability to provide virtual core thickness with low variability. Research is still required to develop a prototype system that integrates point cloud data from two scanners; coordinate control will be required, which can use a total station approach or GPS for x-y control and the stringline for accurate elevation readings.

Electromagnetics has also proved to be a suitable approach to measuring pavement thickness. This technique is probably closer to field implementation than the laser scanning approach. The electromagnetic approach would most likely involve the placement of metal plates (size and thickness to be determined) on the base in a random fashion. A row of electromagnetic sensors would be mounted on the back of the paver to measure concrete pavement thickness at any location along its width.

Although both laser scanning and electromagnetic sensing techniques can be used to determine concrete pavement thickness, the subcommittee recommended that the research team pursue the electromagnetic technique because it is closer to implementation. Laser scanning would involve tight coordinate control, which is possible using current technology (e.g., robotic total stations and a combination of GPS and the stringline for elevation control). Electromagnetic sensors will be more economical and can be implemented in a handheld device or fixed behind the paver.

REFERENCES

American Association of State Highway and Transportation Officials (AASHTO). 2001. *Standard Method of Test for Measuring Length of Drilled Concrete Cores*. AASHTO T 148-97 (2001). Washington, D.C.: American Association of State Highway and Transportation Officials.

Cable, J. K., and E.J. Jaselskis. 2004. *Stringless Portland Cement Concrete Paving*. Report TR-490. Ames, IA: Center for Portland Cement Concrete Pavement Technology.

Civil Engineering. 1994. Impact echo in the thick of pavement construction. *Civil Engineering--ASCE* 64.12: 19, 21.

Cutelius, B. 1998. Engineering applications of airborne scanning lasers: reports from the field. *Photogrammetric Engineering and Remote Sensing* 64.4: 246–247.

DeVault, J.E., and R.D. Miller. 2004. *A Field Verification Instrument to Assss the Placement Accuracy of Dowel Bars and Tie Bars in PCCP*. K-Tran: KSU-03-1. Topeka, KS: Kansas Department of Transportation.

Euro NDT Ltd. 2006. *Eddy Current NDT Inspection*. http://www.eurondt.com/EDDY CURRENT.html.

GOMACO. 2004. Stringless Control System. http://www.gomaco.com/downloads/ stringless_brochure.pdf.

GOMACO World. 2004. One of the First Concrete Projects in Baja Paves with a First of its Kind Paver. *GOMACO World* 32.1. http://www.gomaco.com/Resources/worldstories/ world32_1/altaingenieria.html.

Grogg, M. G., and K.D. Smith. 2001. *PCC Pavement Smoothness: Characteristics and Best Practices for Construction*. Washington, D.C.: U.S. Department of Transportation, Federal Highway Administration.

Guralnick, S.A., E.S. Suen, and C. Smith. 1993. Automating inspection of highway pavement surfaces. *Journal of Transportation Engineering* 119: 1–12.

Iowa Department of Transportation. 2001. *Standard Specifications for Highway and Bridge Construction*. Ames, IA: Iowa Department of Transportation.

Iowa Department of Transportation. 2005. Materials Instructional Memorandum 346: Locating, Drilling & Evaluating Portland Cement Concrete Pavement Cores. *Instructional Memorandums*. Ames, IA: Iowa Department of Transportation, Office of Materials.

Kolectric. 2006. *Micro Covermeter*. http://www.kolectric.com.

Maierhofer, C. 2003. Nondestructive Evaluation of Concrete Infrastructure with Ground Penetrating Radar. *Journal of Materials in Civil Engineering* 15.3: 287–297.

Popovics, S., N.M. Bilgutay, and M. Karaoguz. 2000. High-frequency ultrasound technique for testing concrete. *ACI Materials Journal* 97.1: 58–65.

Public Works. 1995. New tool for nondestructive thickness measurements (impact echo device). *Public Works* 126.1: 52–53.

RIEGL Laser Measurement Systems. 2004. *2D Tunnel Profiler LMS-Q250i*. http://www.riegl.com/industrial_scanners_/lms_q250i_/q250i_all_.htm.

Roberts, J., G. Winstanley, and P. Corke. 2003. Three-Dimensional Imaging for a Very Large Excavator. *International Journal of Robotics Research* 22.7/8: 467–477.

Sawyer, T. 2002. Lasers Go Into Overdrive, Pushed by Technology Gains. *ENR* 249.12: 54, 56.

Tou, J.T. and R.C. Gonzales. 1974. *Pattern Recognition Principles*. Reading, MA: Addison Wesley.

Wozencraft, J. and D. Millar. 2005. Airborne Lidar and Integrated Technologies for Coastal

Mapping and Nautical Charting. *Marine Technology Society Journal* 39.3: 27–35.

Yu, H.T. and L. Khazanovich. 2005. *Use of Magnetic Tomography Technology to Evaluate Dowel Placement*. FHWA-IF-06-006. Washington, D.C.: Federal Highway Administration.

Zircon. 2006. *MT6 Electronic Metal Locator*. http://www.zircon.com/SellPages/ScanAndSensor/ScanAndSensor/ScanAndSensor-Metal.html.

APPENDIX: STATISTICAL ANALYSIS OF THICKNESS DATA

1. Introduction

The first part of this project will look at the accuracy of predicting the depth of pavement based on two data sets: one for the height of the subbase (subbase data set) and one for the height of the pavement (pavement data set). Both data sets were created using a scanner, which was placed at the side of a four-lane divided highway. To create the pavement data set and the subbase data set, the scanner measured the height of the subbase before the paving operation was completed and then the height of the pavement after the paving operation was completed for one side of the four-lane divided highway. Each data set consists of thousands of observations, with each observation consisting of three coordinates, all recorded in meters. Ordinary kriging was then used to create two prediction surfaces: one for the pavement data set and one for the subbase data set.

The depth of the pavement at a particular location was then determined by calculating the difference between the two prediction surfaces at that location. Pavement and subbase data sets were obtained at three different locations and then analyzed to the error associated with using a scanner to determine pavement depth in a nondestructive manner. Since the scanner cannot distinquish between the subbase and the dowel bars, the subbase data sets contain measurements of the height of dowel bars. To remove the impact of the measurements based on the dowel bars, two rows of dowel bars were chosen for each subbase data set. Each subbase data set was then reduced so that the data set consists of observations located between the two rows of dowel bars. Each pavement data sets was then reduced to match the boundaries of its respective subbase data set. Therefore, only a small area of the road was analyzed at each of the three locations.

The second part of the project will examine the impact of the number of observations on the squared errors. The specific objective is to see whether increasing the number of observations reduces the size of the squared errors and, thus, decreases the size of the confidence intervals.

2. Ordinary Kriging

To predict the depth of the pavement, ordinary kriging was employed. Ordinary kriging first consists of calculating the empirical variogram. To calculate the empirical variogram, the distance between two points is calculated for all possible pairs of points. The distance between two points is then used to place each pair of points into a bin with other pairs that are separated by a similar distance. Suppose that there are n bins, such that h_n represents the nth bin. Then, an estimate of the variability of the difference between the z-coordinate for each pair of points in a bin is calculated using the method-of-moments estimator, which is given in the following:

$$\frac{1}{|N(h_n)|} \sum_{N(h_n)} \{Z(s_i) - Z(s_j)\}, \tag{2.1}$$

Where $N(h_n)$ represents all pairs of points in the nth bin, $|N(h_n)|$ represents the number of pairs of points in the nth bin, and $Z(s_k)$ represents the z-coordinate at location s_k for $k = i, j$.

The empirical variogram is then a plot of the estimate of variability as calculated by (2.1), represented as $2\hat{\gamma}(h_n)$ versus the midpoint of the bin range. If $\hat{\gamma}(h_n)$ is plotted instead of $2\hat{\gamma}(h_n)$, the variogram is called a semi-variogram. A theorectical variogram is then fitted to the empirical variogram. The goal is to fit a theoretical variogram that has a shape very similar to that of the empirical variogram. There are several theoretical variograms, such as linear, power, and wave, but two theoretical variograms in particular were similar in shape to the empirical variograms for all the pavement and subbase data sets: the spherical and exponential variograms. The spherical semi-variogram is represented by the following equation:

$$\gamma(h \mid \theta) = \begin{cases} 0, & h = 0 \\ c_0 + c_s\{(3/2)(h/a_s) - (1/2)(h/a_s)^3\}, & 0 < h < a_s, \\ c_0 + c_s, & h \geq a_s \end{cases} \quad (2.2)$$

Where c_0 is interpreted as the nugget, c_s is the partial sill and a_s is the range.

Similarly, the exponential semi-variogram is as follows:

$$\gamma(h \mid \theta) = \begin{cases} 0, & h = 0 \\ c_0 + c_e\{1 - \exp(-h/a_e)\}, & h \neq 0 \end{cases}, \quad (2.3)$$

Where c_0 is interpreted as the nugget, c_e is the partial sill and a_e is the effective range.

Both spherical and exponential variograms were fitted to the empirical variogram for all data sets. Futhermore, a weighted least squares criterion was calculated for each variogram:

$$Q(\theta \mid z) = \sum_{n=1}^{m} |N(h_n)| \left\{ \frac{\hat{\gamma}(h_n)}{\gamma(h_n \mid \theta)} - 1 \right\}^2, \quad (2.4)$$

The variogram with the lowest weighted least squares criterion was chosen. Ordinary kriging then uses the chosen theoretical variogram to predict the z-coordinate at a new location by taking a linear combination of the existing observations with weights that are based on the theoretical variogram.

3. Hospers, Iowa, Data Set

3.1. Pavement Data Set

First, the pavement data set was analyzed. Because the scanner is able to take thousands of measurements in a small area, the pavement data set contains 5,905 observations. Since the

location of the centerline of the road could only be approximated, the data set was rotated so the center of the two-lane road (one-half of a four-lane divided highway) would run as close as possible along the x-axis.

Figure 1 contains the contour plot of the pavement data set on the left and the perspective plot on the right. The x- and y-coordinates were measured in meters, while the z-coordinate was multiplied by 1,000 to convert the units from meters to millimeters. The reason for converting the z-coordinate to millimeters will be explained later. The perspective plot shows that the pavement increases in height from left to right in the x-direction. The plot also shows the crown present in the pavement, which creates an inverted V pattern in the pavement along the x-axis, although one side of the pavement has a greater slope than the other side. Since these trends in the pavement were intentionally created by the paver and prediction is the main goal of the analysis, trends are removed by fitting a linear model. Ordinary kriging is then performed using the residuals that result from the model.
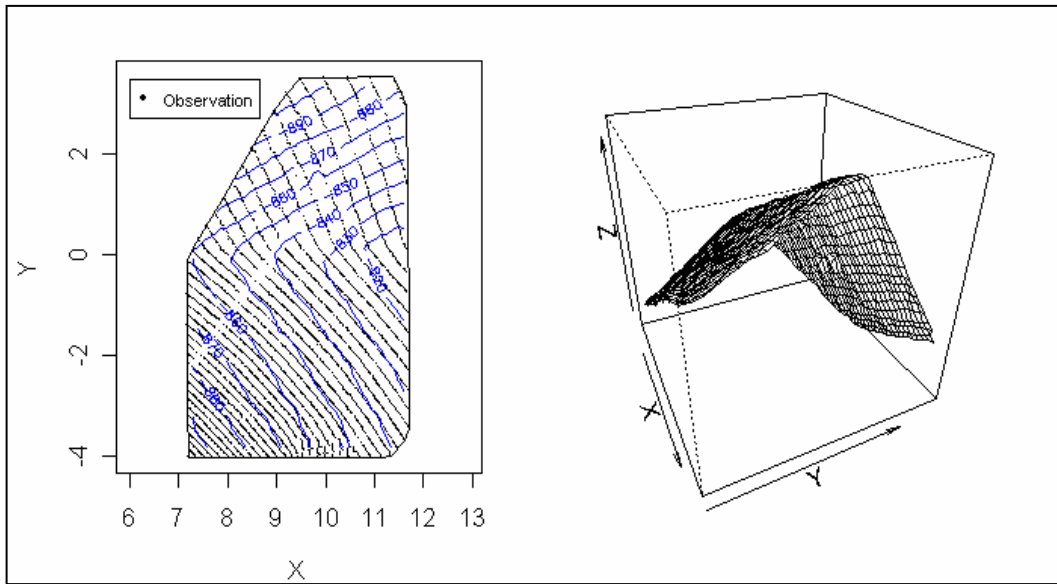
Figure A.1. Contour plot and perspective plot of the pavement data set

From the trends that were observed in the perspective plot in Figure A.1, a model that appropriately describes the trends, which will be called Model 1, is as follows:

$$Z = \beta_0 + \beta_1 X + \beta_2 |Y| + \beta_3 Y_1,$$
(3.1)

Where $Y_1 = \begin{cases} Y, & \text{if } Y \geq 0 \\ 0, & \text{if } Y < 0 \end{cases}$.

The Y_1 term was added to account for the fact that the slope on one side of the inverted V pattern is steeper than the slope on the other side.

65

Figure A.2 contains the contour plot and the perspective plot of the residuals that were produced by Model 1, while Table A.1 contains the ordinary least squares estimates for the parameters. Since the residuals range from -5.8 mm to 8.6 mm, changing the units of the z-coordinate into mm at the beginning of the analysis allows the residuals to be described in reasonable units.

Table A.1. Parameter estimates for Model 1

Parameters	Estimates
β_0	-948.688
β_1	12.257
β_2	-8.606
β_3	-13.198
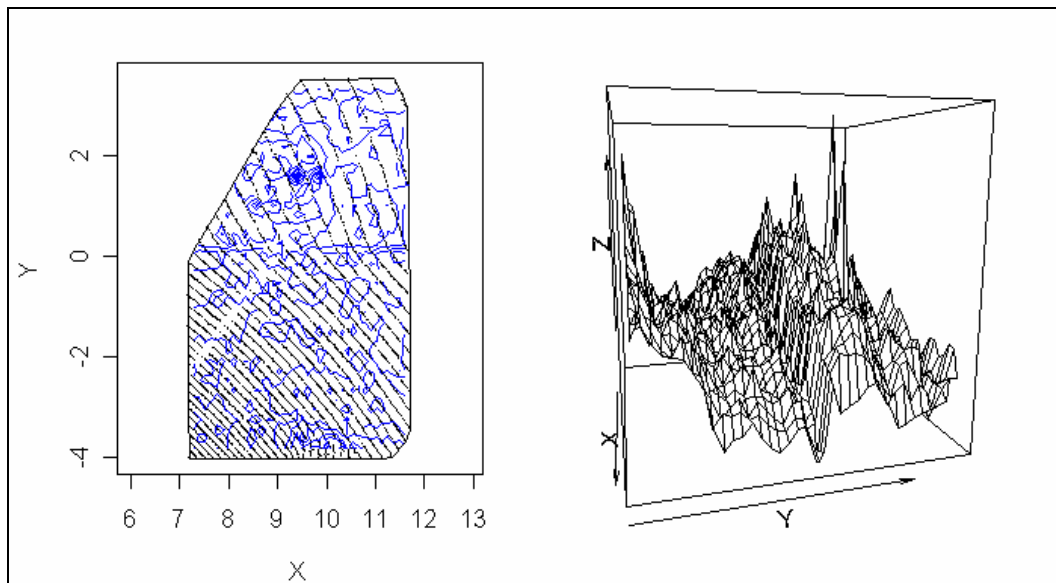
Figure A.2. Contour plot and perspective plot of residuals (mm) from Model 1

To examine the spatial dependence among the residuals, three empirical variograms were computed based on the residuals: an omnidirectional variogram, a directional variogram with an azimuth angle of 0 degrees and a tolerance angle of 22.5 degrees, and a directional variogram with an azimuth angle of 90 degrees and a tolerance angle of 22.5 degrees. Directional variograms were calculated because the equipment used to compact the subbase and pave the road moves parallel to the centerline of the road. Due to computer memory limitations, empirical variograms could not be calculated for the nearly 6,000 observations. Consequently, empirical variograms were calculated from a random sample of 2,000 residuals produced by Model 1 and their respective locations. Unfortunately, none of these variograms looked similar in shape to a theoretical variogram, such as an exponential or spherical variogram.

Therefore, Model 1 was altered to account for additional trends in hopes of obtaining an empirical variogram that would be similar in shape to a theoretical variogram. Since one of the

prominent patterns that can be detected in the perspective plot in Figure A.2 is a ridge along the x-axis, a term can be added to the model that will allow the trend describing observations with y-coordinates that are greater or equal to zero to have a different intercept. Consequently, the second model, Model 2, is as follows:

$$Z = \beta_0 + \beta_1 Y_0 + \beta_2 X + \beta_3 |Y| + \beta_4 Y_1, \tag{3.2}$$

Where $Y_0 = \begin{cases} 1, & if\ Y \geq 0 \\ 0, & if\ Y < 0 \end{cases}$.

Table A.2 contains the ordinary least squares estimates for the parameters, while Figure A.3 contains the contour plot and the perspective plot of the residuals from Model 2. All three types of empirical variograms that were calculated for Model 1 were again calculated based on a random sample of 2,000 residuals produced by Model 2. Fortunately, the residuals from Model 2 produced a directional variogram with an azimuth angle of 90 degrees that is similar in shape to the exponential or spherical variogram. All three types of variograms are shown in Figure A.4. Basing the theoretical variogram on the directional empirical variogram with an azimuth angle of 90 degrees is reasonable because, as mentioned above, both the compacting and paving operations move parallel to the centerline of the road.

Table A.2. Parameter estimates for Model 2

Parameters	Estimates
β_0	-949.273
β_1	2.038
β_2	12.259
β_3	-8.405
β_4	-14.101
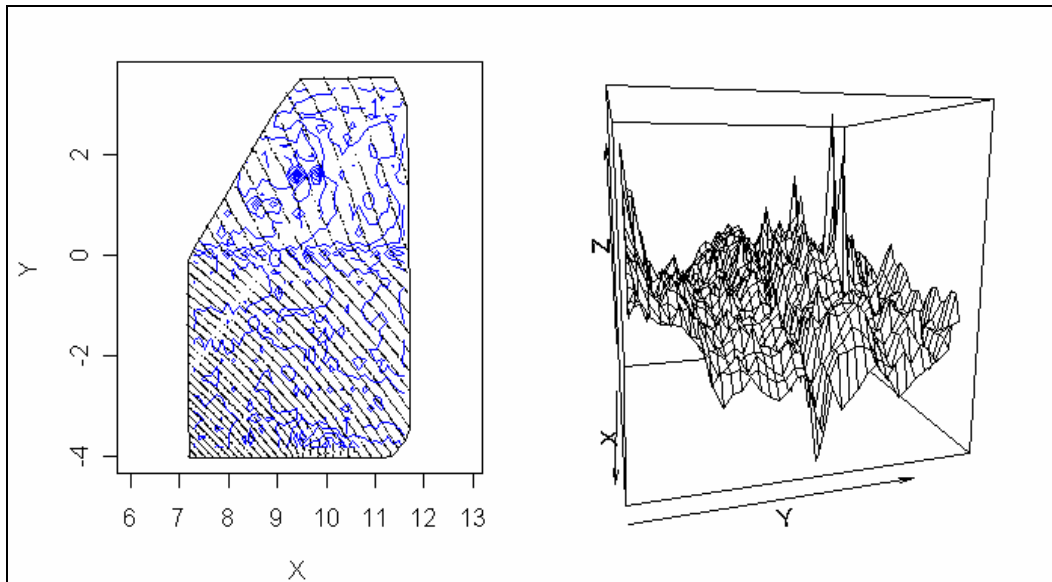
Figure A.3. Contour plot and perspective plot of residuals (mm) from Model 2

Estimates for the parameters for the exponential and spherical variograms were obtained using the variofit command in R. Only points based on a maximum distance of four meters were used to fit the theoretical variograms to reduce the influence of points that are based on a relatively small number of pairs of locations. Figure A.5 contains a plot of the empirical semi-variogram with the fitted exponential and spherical semi-variograms, while Table A.3 contains the estimates for the parameters of the exponential and spherical variograms.
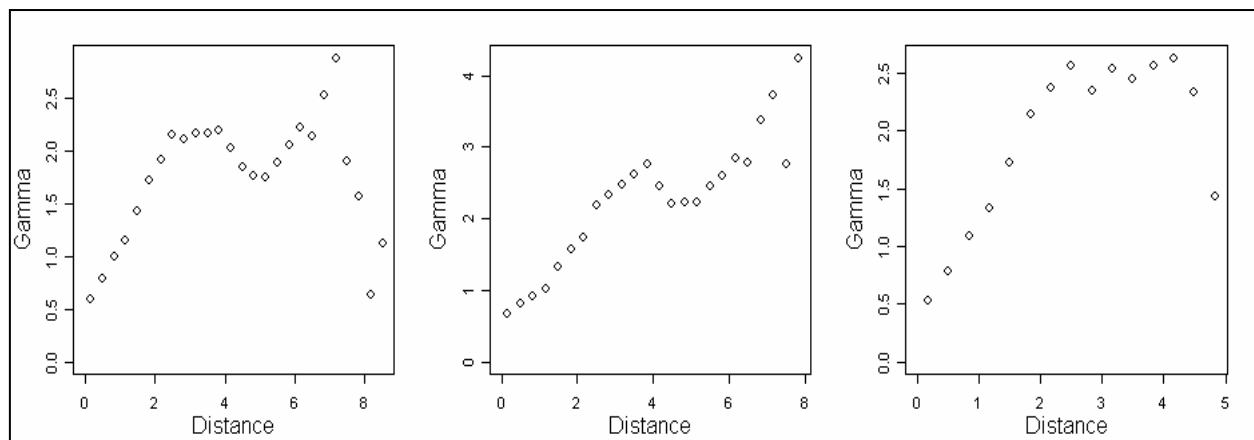
Figure A.4. Empirical semi-variogram of the residuals (left to right: omnidirectional, 0 degrees, and 90 degrees)
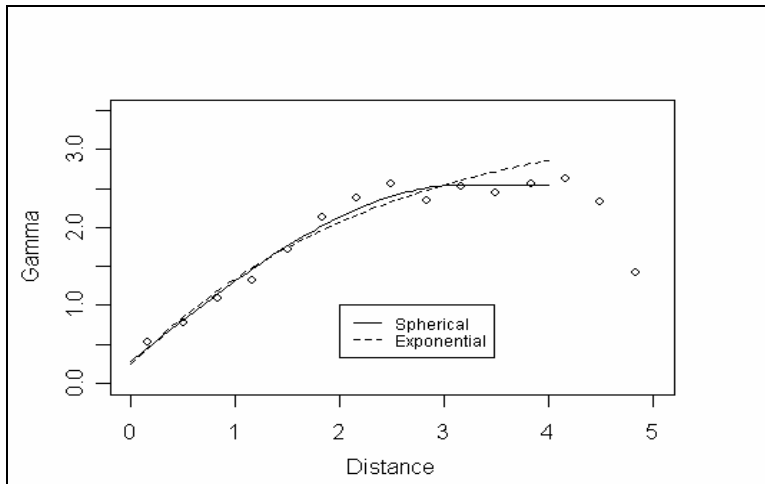
Figure A.5. Fitted theoretical semi-variograms

Table A.3. Estimates of parameters for theoretical variograms

| Parameters	Spherical	Exponential
Tausq	0.285	0.240
Sigmasq	2.265	3.223
Phi	3.194	2.388
WLS criterion	1354.87	2704.93

According to the weighted least squares criterion and Figure A.5, the spherical variogram fits the empirical variogram better than the exponential variogram. Next, ordinary kriging was performed using the spherical variogram and another random sample of 2,000 residuals from Model 2. By choosing another 2,000 residuals from the remaining 3,905 residuals that were not chosen for the calculation of the empirical variogram, one can assess how well ordinary kriging can predict the height of the pavement by comparing the predicted height to the observed height at locations that were not used to estimate the parameters of the model. The second random sample consisting of 2,000 residuals and their respective locations will be called the validation data set. Predictions and prediction squared errors for the validation data set are shown graphically in the image and contour plots in Figure A.6. The squared errors are slightly larger in the lower left-hand corner of the contour plot than in the upper right-hand corner, which is a result of the pavement data being denser in the lower left-hand corner than in the upper right-hand corner. The impact of the number of observations on the squared errors will be examined in more detail in a later section.
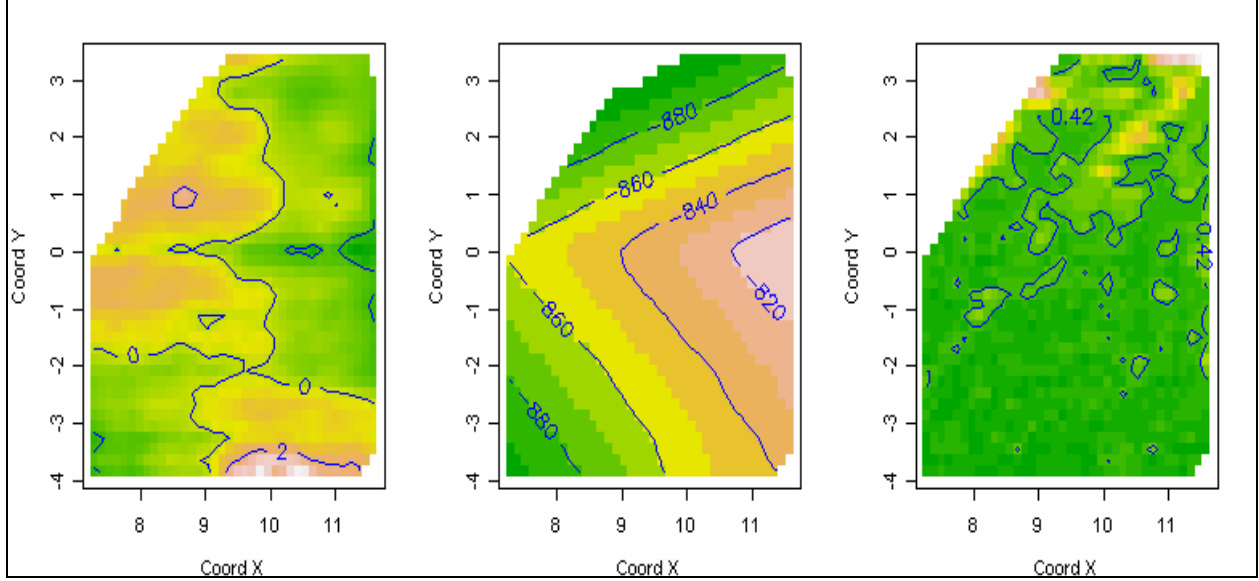
Figure A.6. Contour and image plots of predictions for residuals (left), predictions for pavement height (center), and squared errors (right)

Confidence intervals based on a significance level of 0.05 were then calculated for each location in the validation data set. The predicted height of the pavement consists of the sum of the predicted height from Model 2 and the corresponding predicted residual from the kriging analysis for each location. The 95% confidence intervals were then calculated as follows:

$$p_p(Z, s_i) \pm 1.96 \sqrt{\sigma_p^2(s_i)} \tag{3.3}$$

Where $p_p(Z, s_i)$ is the prediction of height at location, s_i,

and $\sigma_p^2(s_i)$ is the squared error at location, s_i.

The coverage probability, which is the percentage of confidence intervals that capture the actual observation, is 96.6%. The median and the interquartile range of the width of the confidence intervals are 2.45 mm and 0.11 mm, respectively. Moreover, the theoretical prediction mean squared error, which is the mean of the squared errors from the kriging analysis, is 0.402. The empirical prediction mean squared error is 0.437 and is calculated as follows:

$$\hat{\sigma}^2_e = \frac{1}{n} \sum_{i=1}^{n} (Z(s_i) - \hat{Z}(s_i))^2 \tag{3.4}$$

Since random samples were used for the analysis, the steps described in this section, beginning with generating a random sample of 2,000 observations to create the empirical variogram, were repeated 25 times to better understand the values that could be expected for the coverage probability and the median width of a confidence interval. However, only a spherical variogram was fitted to the empirical variogram for every random sample and used for prediction. It is possible that, in some cases, an exponential variogram may have been a slightly better choice. In

70

addition, since the process was repeated only 25 times, the following summary should be treated as a descriptive statement, not an inferential statement. For the 25 repetitions, the minimum and maximum values for the coverage probability are 94.8% and 97.3%, respectively, and the minimum and maximum values for the median width are 2.08 mm and 2.83 mm, respectively.

3.2. Subbase Data Set

The subbase data set, which contains 7,698 observations, was rotated and analyzed in the same manner as the pavement data set. As expected, the trends discovered in the pavement data can be seen in the subbase data, as shown in Figure A.7. However, the trends are less pronounced, since the subbase material does not create a surface that is as smooth as the pavement surface.

Since Model 2 was used to model the trends in the pavement data set, Model 2 will also be used to model the trends in the subbase data set. The ordinary least squares estimates can be found in Table A.4, and the contour plot and perspective plot of the residuals from Model 2 can be found in Figure A.8.
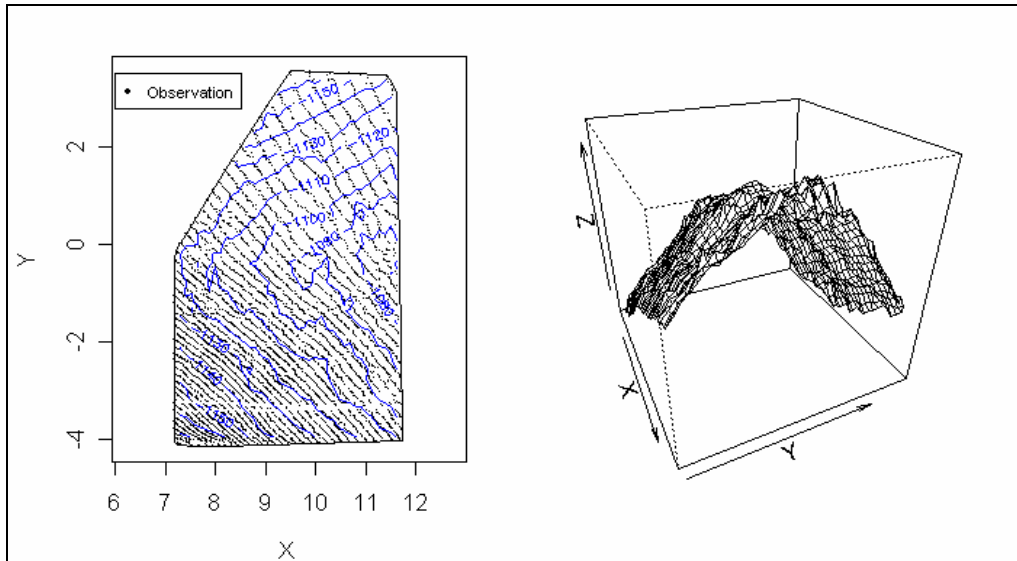
Figure A.7. Contour plot and perspective plot of the subbase data set

Table A.4. Parameter estimates for Model 2

Parameters	Estimates
β_0	-1201.123
β_1	-7.097
β_2	12.280
β_3	-13.254
β_4	-7.390
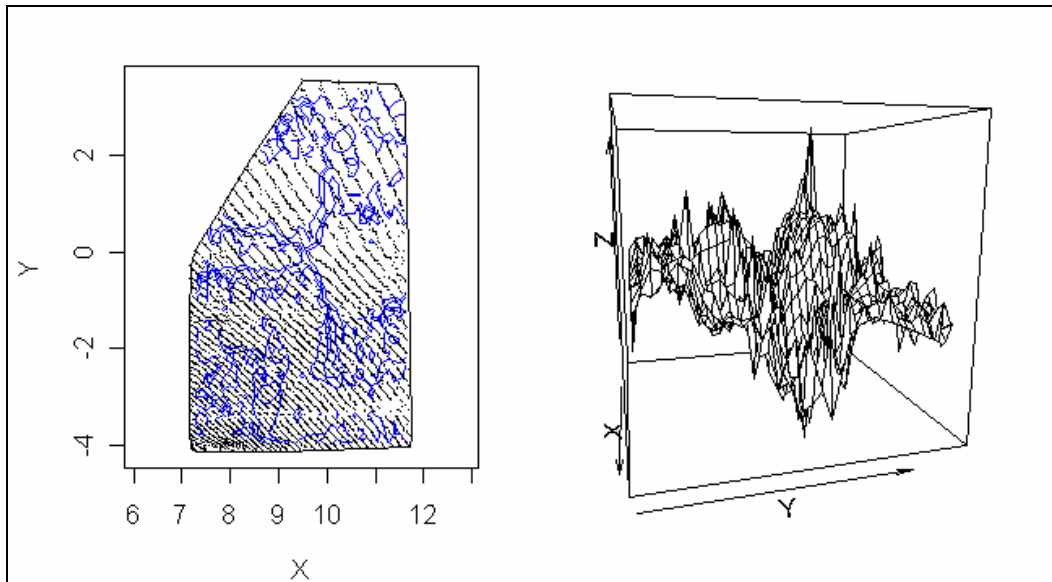
Figure A.8. Contour plot and perspective plot of residuals (mm) from Model 2

The next step was to plot the empirical variograms, as shown in Figure A.9. Again, the directional variogram with an azimuth angle of 90 degrees seems to be similar in shape to a spherical or exponential variogram, at least for distances up to four meters. Therefore, a maximum distance of four meters will be used when fitting the theoretical variograms. However, for the subbase data set, the exponential variogram is a better fit than the spherical variogram according to the weighted least squares criterion. The theoretical semi-variograms are shown in Figure A.10, while the parameter estimates for the spherical and exponential variograms are shown in Table A.5.
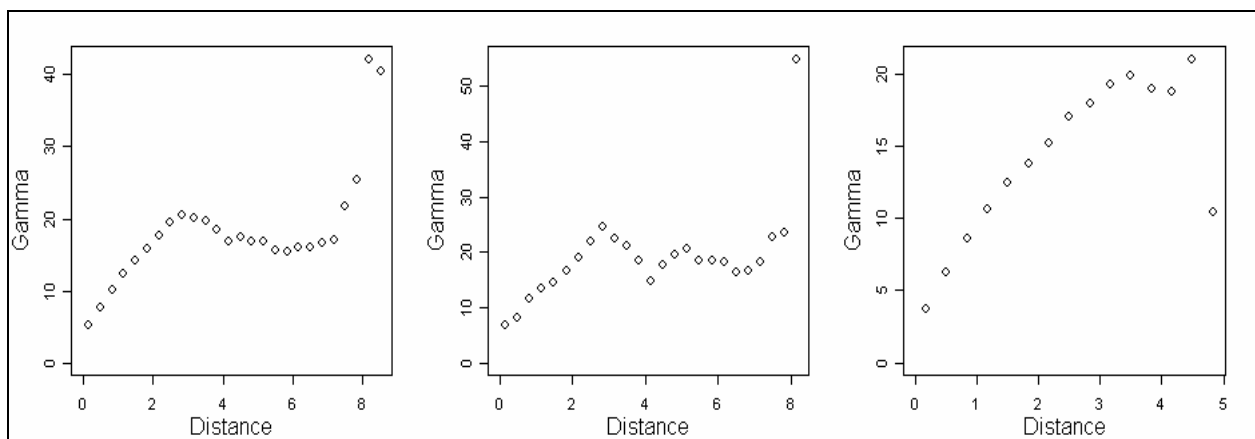
Figure A.9. Empirical semi-variogram of the residuals (left to right: omnidirectional, 0 degrees, and 90 degrees)
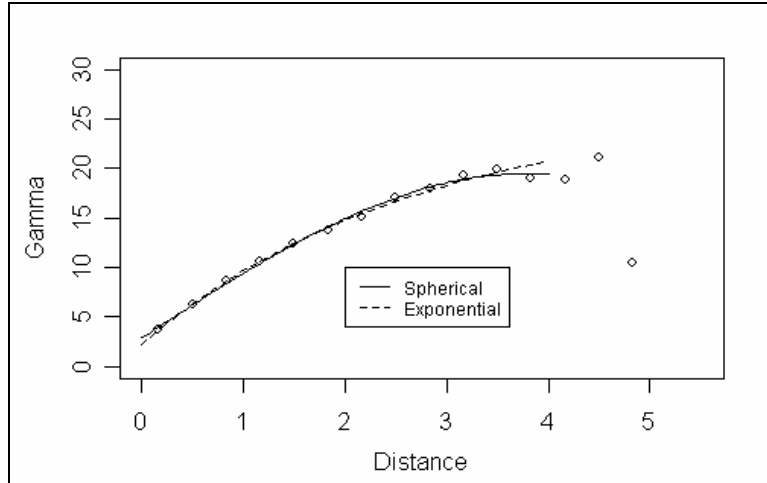
Figure A.10. Fitted theoretical semi-variograms

**Table A.5. Estimates of parameters for theoretical variograms**

Parameters	Spherical	Exponential
Tausq	2.876	2.238
Sigmasq	16.550	23.943
Phi	3.731	2.713
WLS criterion	203.13	171.76

Again, a random sample of 2,000 observations was selected from the remaining observations that were not used to calculate the empirical variogram. Next, ordinary kriging was performed using the exponential variogram. Once predictions were obtained, confidence intervals based on a significance level of 0.05 were calculated for each location in the validation data set. The coverage probability is 95.9%, while the median and the interquartile range of the width of the confidence intervals are 6.98 mm and 0.36 mm, respectively. The theoretical prediction mean squared error is 3.230, while the empirical prediction mean squared error is 2.870. The median width of the confidence intervals for the subbase is larger due to the uneven nature of the subbase when compared to pavement. The contour and image plot of the predictions and squared errors can be seen in Figure A.11.

As with the pavement data, the above process was repeated 25 times, beginning with generating a sample of 2,000 observations to create the empirical variogram. However, only an exponential variogram was fitted to the empirical variogram for every random sample and used for prediction. It is possibile that a spherical variogram could have a lower value for the weighted least squares criterion. For the 25 repetitions, the minimum and maximum values for the coverage probability are 94.7% and 97.1%, respectively. The minimum and maximum values for the median width are 6.42 mm and 7.70 mm, respectively.
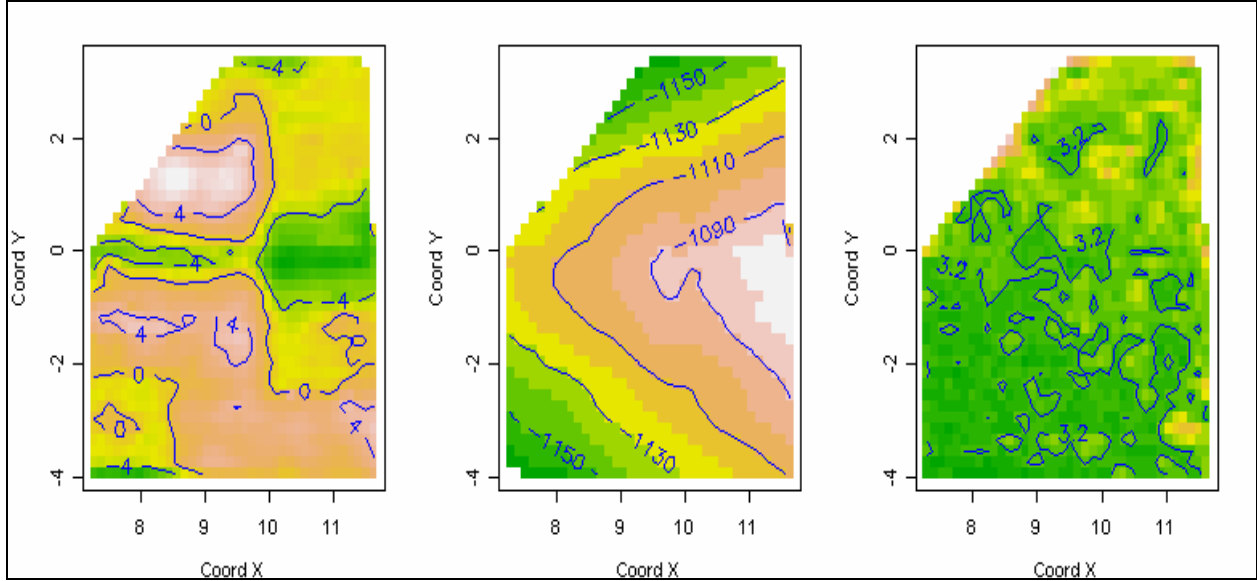
Figure A.11. Contour and image plots of predictions of residuals (left), predictions of subbase height (center), and squared errors (right)

3.3. Depth of Pavement

The 2,000 locations from the subbase validation data set were not only used to predict the height of the subbase at those locations but the height of the pavement as well.

Once the predictions and squared errors were calculated for the height of the subbase and the predictions and squared errors were calculated for the height of the pavement, the 95% confidence intervals were constructed as follows:

$$p_p(Z,s_i) - p_s(Z,s_i) \pm 1.96\sqrt{\sigma_p^2(s_i) + \sigma_s^2(s_i)} \qquad (3.5)$$

Where $p_j(Z,s_i)$ is the prediction of height at location, s_i, for $j = p, s$

and $\sigma_j^2(s_i)$ is the squared error at location, s_i, for $j = p, s$.

The median width and interquartile range of the 95% confidence intervals are 7.46 mm and 0.45 mm, respectively. The image and contour plots of the predictions for the depth of the pavement and the squared errors are shown in Figure A.12.

74
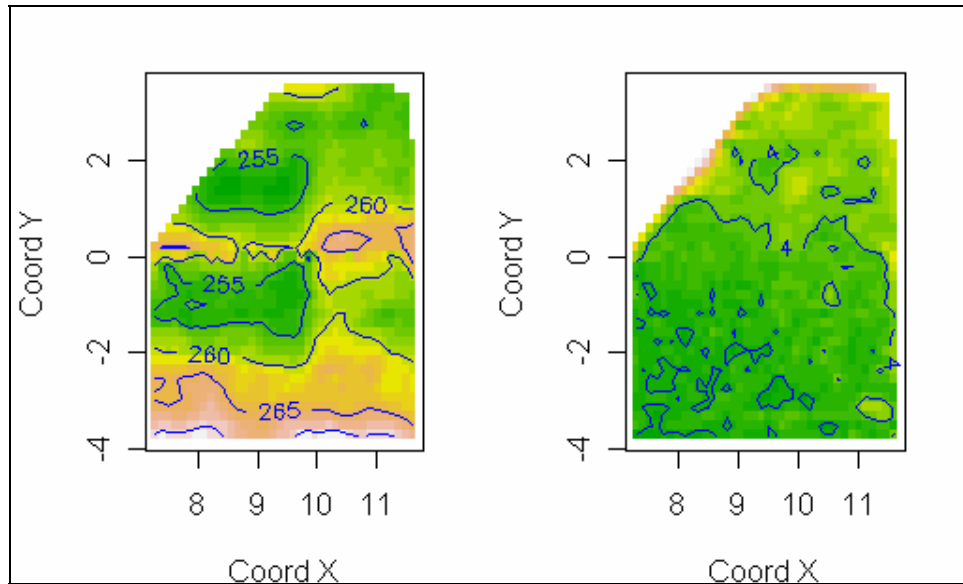
Figure A.12. Contour and image plots of predicted depth of pavement (left) and squared errors (right)

4. Tama, Iowa, Data Set

4.1. Pavement Data Set

Again, starting with the pavement data set, Figure A.13 contains the contour plot of the pavement data set on the left, while the perspective plot is on the right. Tabe A.6 shows the Model 1 parameter estimates. The perspective plot shows that the height of the pavement is increasing in the y-direction and decreasing in the x-direction. Furthermore, an inverted V pattern is not present in this data set. Consequently, a model that accounts for a linear trend in both the x- and y-directions should be sufficient. This model, which will be called Model 1, is as follows:

$$Z = \beta_0 + \beta_1 X + \beta_2 Y .$$
(4.1)
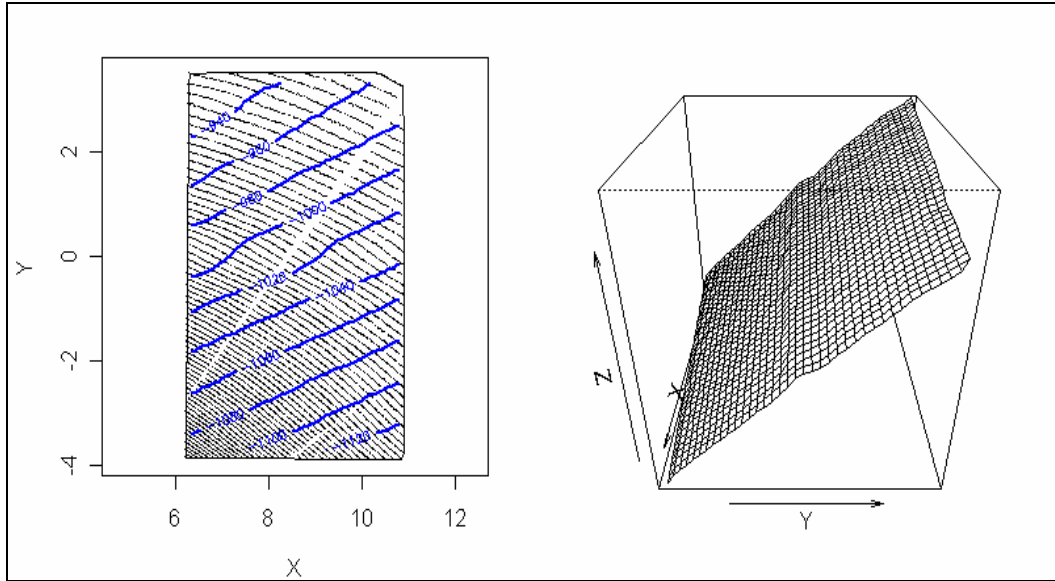
Figure A.13. Contour plot and perspective plot of the pavement data set

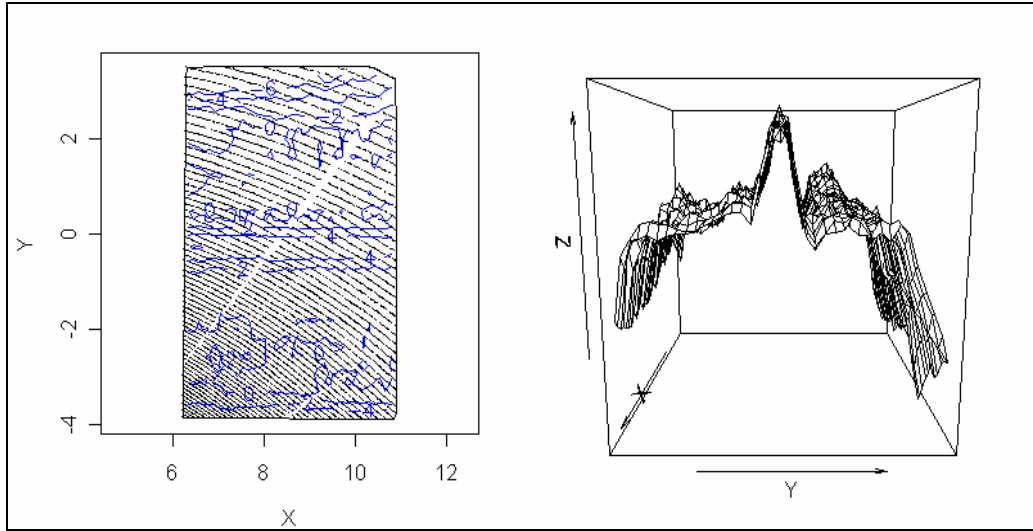**Table A.6. Parameter estimates for Model 1**

Parameters	Estimates
β_0	-930.557
β_1	-10.219
β_2	24.520

After examining the contour and perspective plot of the residuals in Figure A.14, the strong trends are found in the residuals, especially parallel to the x-axis. Next, three different empirical variograms were calculated as described in the previous section. Although the directional empirical variogram with the azimuth angle of 90 degrees looked promising, the coverage probability for a number of samples was much less than the intended 95% coverage probability. Therefore, Model 1 was altered in an attempt to improve the empirical variograms. Since there is an inverted V pattern in the residuals, a second model, Model 2, is as follows:

$$Z = \beta_0 + \beta_1 X + \beta_2 Y + \beta_3 Y_1 \tag{4.2}$$

Where $Y_1 = \begin{cases} Y, & if \ Y \geq 0 \\ 0, & if \ Y < 0 \end{cases}$.
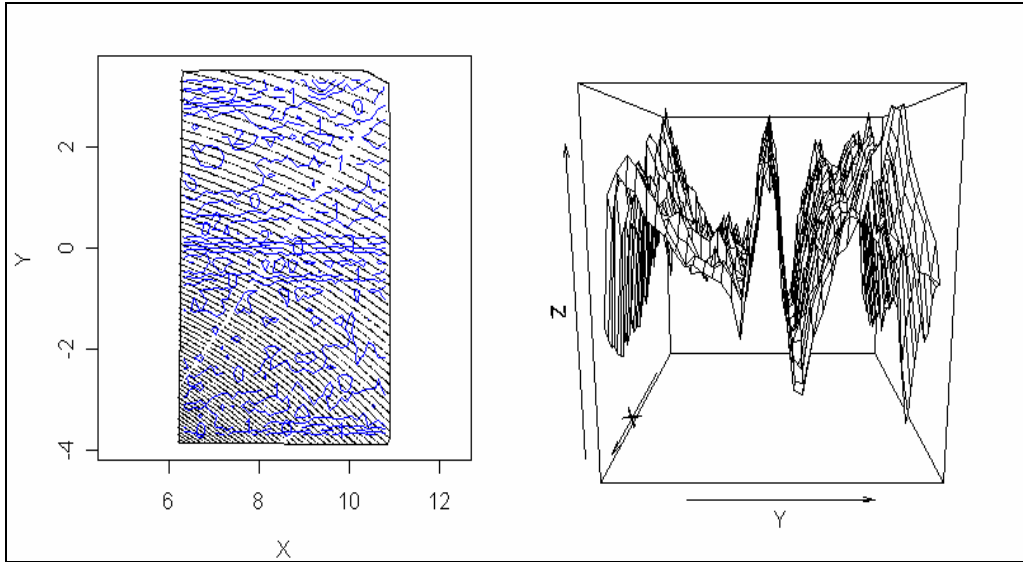
Figure A.14. Contour plot and perspective plot of residuals (mm) from Model 1

Table A.7 contains the ordinary least squares estimates for the parameters, while Figure A.15 contains the contour plot and the perspective plot of the residuals for Model 2. The three types of empirical variograms that were calculated for the previous data sets were again calculated based on a random sample of 2,000 residuals produced by Model 2 and their respective locations. As with the first model, the empirical variograms were not similar in shape to typical theoretical variograms except for the directional variogram with an azimuth angle of 90 degrees. Spherical and exponential variograms were fitted to the empirical variogram, as shown in Figures A.16 and A.17. Table A.8 contains the estimates for the theoretical variogram parameters. For the pavement data, the spherical variogram is associated with a lower value for the weighted least squares criterion than for the exponential variogram.

Table A.7. Parameter estimates for Model 2
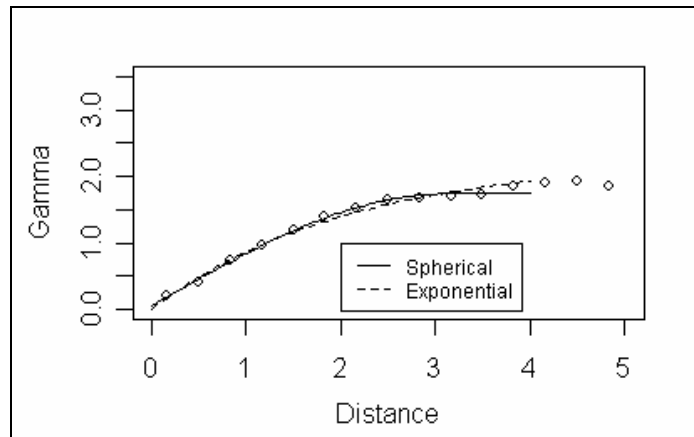
Parameters	Estimates
β_0	-926.741
β_1	-10.243
β_2	26.077
β_3	-4.128

Figure A.15. Contour plot and perspective plot of residuals (mm) from Model 2
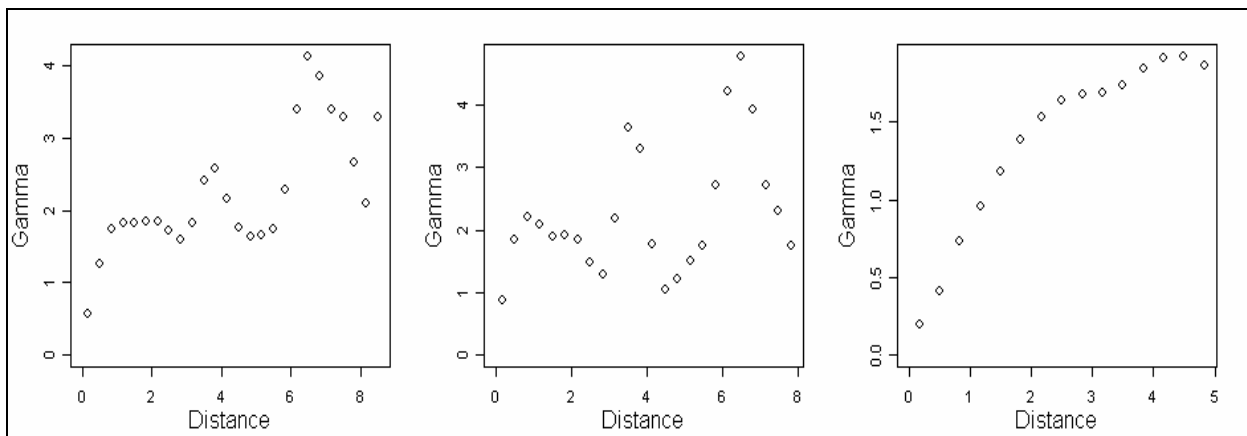
Figure A.16. Empirical semi-variogram of the residuals (left to right: omnidirectional, 0 degrees, and 90 degrees)


Figure A.17. Fitted theoretical semi-variograms

Table A.8. Estimates of parameters for theoretical variograms

Parameters	Spherical	Exponential
Tausq	0.050	0.005
Sigmasq	1.689	2.253
Phi	3.110	2.081
WLS criterion	322.29	857.64

Next, ordinary kriging was performed based on the spherical variogram. Since there are 12,300 observations in the pavement data set and 2,000 of those observations were used to develop the empirical variogram, a second random sample of 2,000 locations was generated from the remaining observations for the validation data set. Predictions and prediction squared errors for the validation data set are shown graphically in the image and contour plots in Figure A.18.
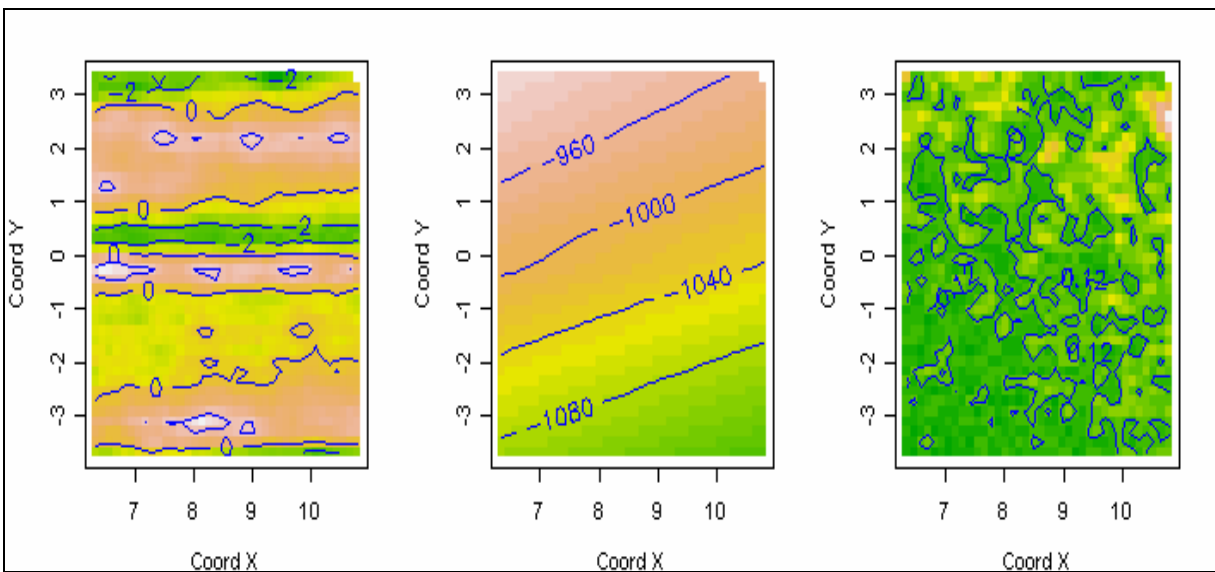

Figure A.18. Contour and image plots of predictions for residuals (left), predictions for pavement height (center), and squared errors (right)

For each location in the validation set, 95% confidence intervals for the height of the pavement were calculated. For these confidence intervals, the coverage probability is 93.9%. Moreover, the median and the interquartile range of the width of the confidence intervals are 1.34 mm and 0.20 mm, respectively. The theoretical prediction mean squared error is 0.122 and the empirical prediction mean squared error is 0.139. After repeating the process 25 times, the minimum and maximum values for the coverage probability were 91.4% and 96.4%, respectively. The minimum and maximum values for the median width are 1.21 mm and 1.43 mm, respectively. Note that only a spherical variogram was fitted to the empirical variogram for every random sample and used for prediction.

4.2. Subbase Data Set

The subbase data set was rotated and analyzed in the same manner as the pavement data set. Figure A.19 shows the contour plot and perspective plot of the subbase data set. Since Model 2

was used to model the trends in the pavement data set, Model 2 was used to model the trends in the subbase data set. The ordinary least squares estimates can be found in Table A.9, and the contour plot and perspective plot of the residuals from Model 2 can be found in Figure A.20.
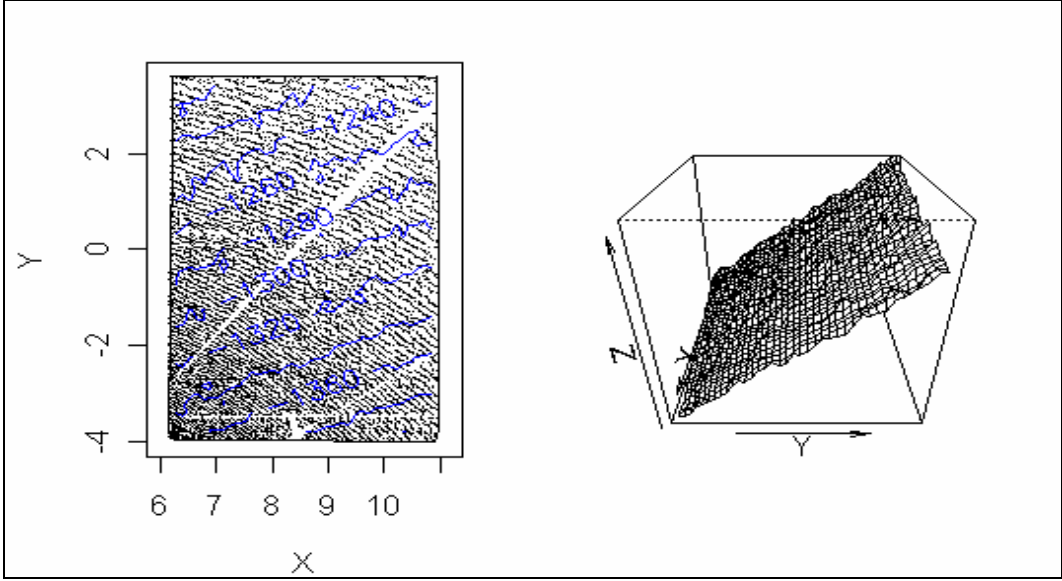
Figure A.19. Contour plot and perspective plot of the subbase data set

Table A.9. Parameter estimates for Model 2

Parameters	Estimates
β_0	-1200.386
β_1	-10.321
β_2	22.824
β_3	-1.768
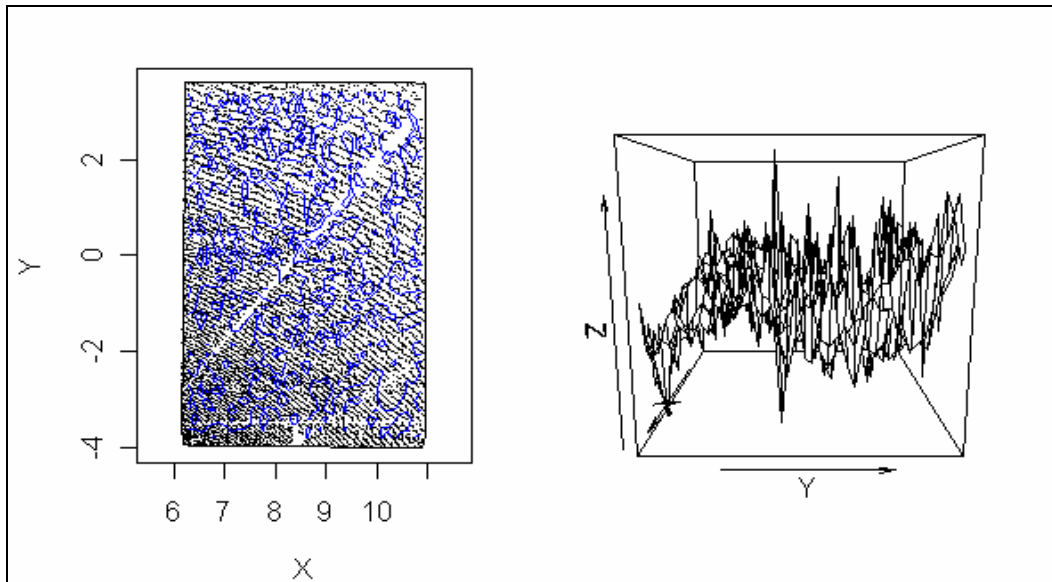
Figure A.20. Contour plot and perspective plot of residuals (mm) from Model 2

The next step was to plot the empirical variograms, shown in Figures A.21 and A.22. The directional variogram with an azimuth angle of 90 degrees still appears to be the most appropriate for fitting a theoretical variogram under a maximum distance of four meters. The parameter estimates for the spherical and exponential variograms are shown in Table A.10, which shows that the spherical variogram fits the empirical variogram better than the exponential variogram according to the weighted least squares criterion.
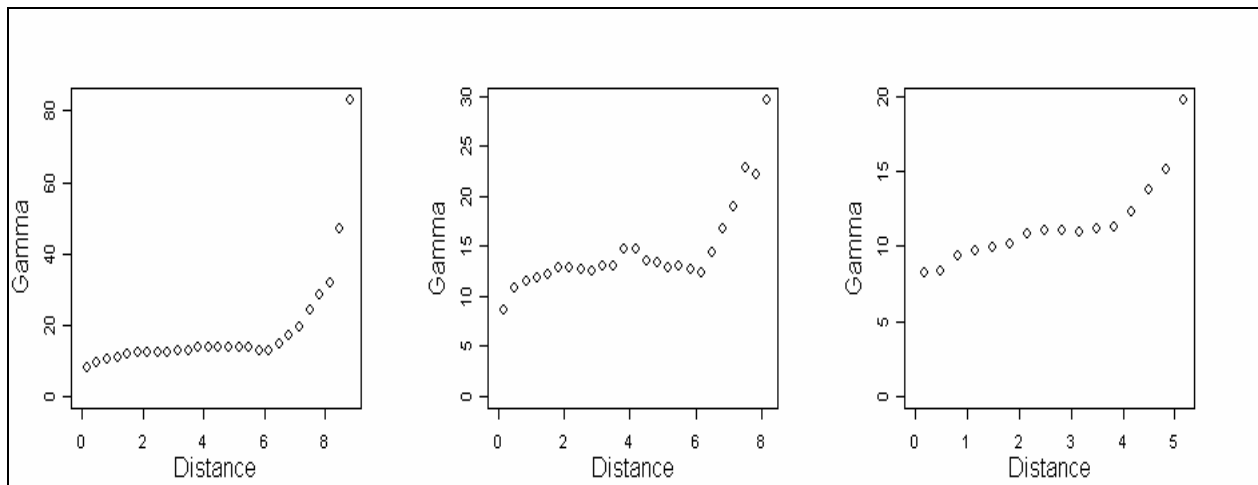
Figure A.21. Empirical semi-variogram of the residuals (left to right: omnidirectional, 0 degrees, and 90 degrees)
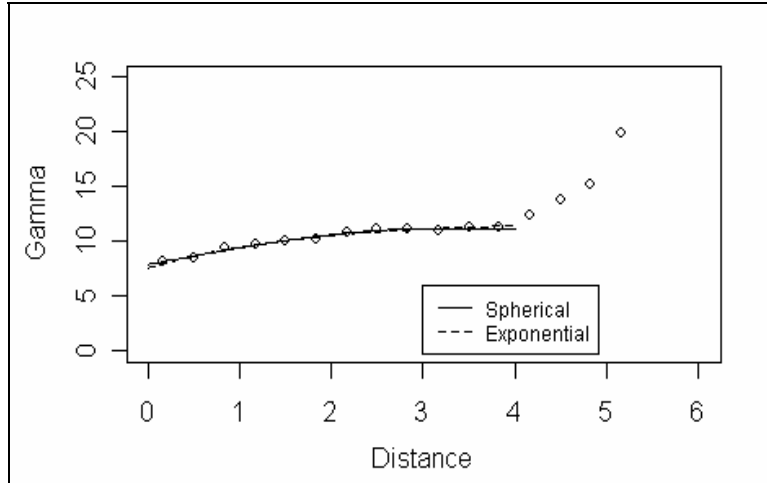
Figure A.22. Fitted theoretical semi-variograms

Table A.10. Estimates of parameters for theoretical variograms

| Parameters	Spherical	Exponential
Tausq	7.853	7.509
Sigmasq	3.311	4.262
Phi	3.179	1.642
WLS criterion	66.54	80.41

Again, a random sample of 2,000 observations was selected from the remaining observations that were not used to create the empirical variogram. Kriging was performed based on the spherical variogram. Once predictions were obtained, confidence intervals based on a significance level of 0.05 were calculated for each location in the validation data set. The coverage probability for these intervals is 94.6%. Moreover, the median and the interquartile range of the width of the confidence intervals are 11.30 mm and 0.07 mm, respectively. The theoretical prediction mean squared error is 8.336, while the empirical prediction mean squared error is 9.061. The contour and image plot of the predictions and squared errors can be seen in Figure A.23. After repeating the process 25 times, the minimum and maximum values for the coverage probability are 92.8% and 95.6%, respectively. The minimum and maximum values for the median width are 9.86 mm and 12.85 mm, respectively. Note that only a spherical variogram was fitted to the empirical variogram for every random sample and used for prediction.
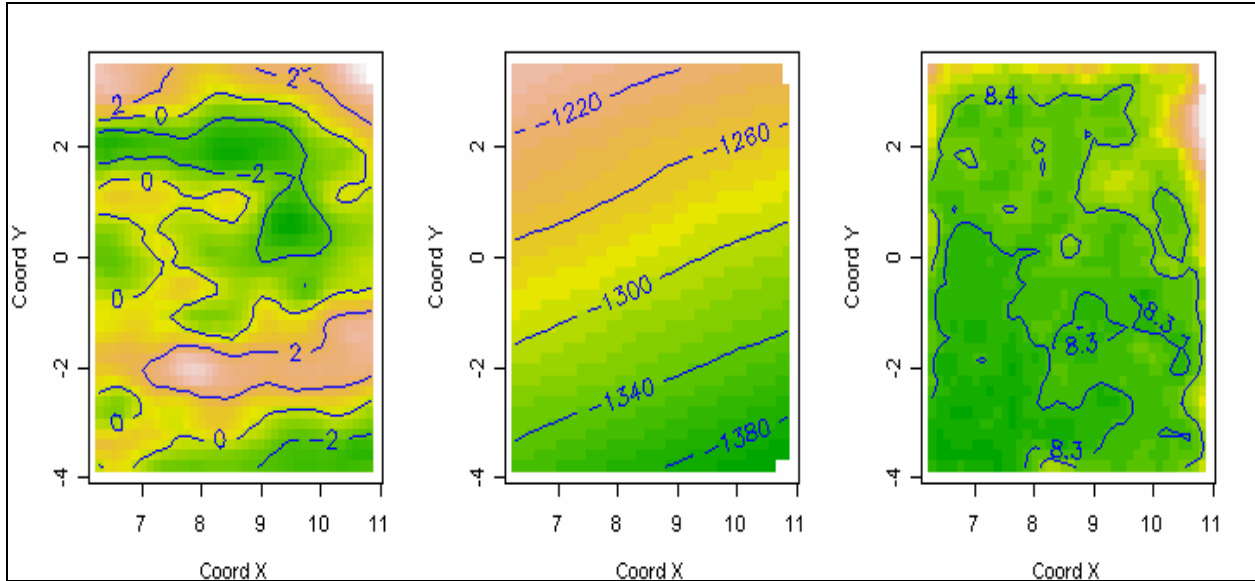
Figure A.23. Contour and image plots of predictions of residuals (left), predictions of subbase height (center), and squared errors (right)

4.3. Depth of Pavement

Ordinary kriging was then used to aid in predicting the height of the pavement and the height of the subbase at the locations that were selected for the subbase validation data set. Confidence intervals were calculated based on a significance level of 0.05. The median width and interquartile range of the 95% confidence intervals are 11.27 mm and 0.12 mm, respectively. The image and contour plots of the predictions for the depth of the pavement and the squared errors are shown in Figure A.24.
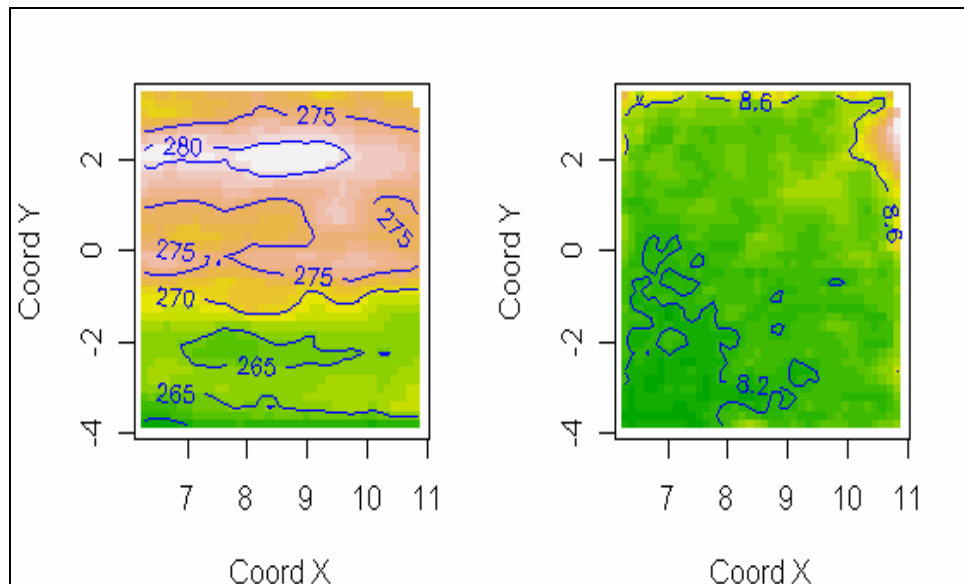
Figure A.24. Contour and image plots of predicted depth of pavement (left) and squared errors (right)

5. Seney, Iowa, Data Set

5.1. Pavement Data Set

Starting with the pavement data set, Figure A.25 contains the contour plot of the pavement data set on the left, while the perspective plot is on the right. The perspective plot shows that there is an inverted V pattern in the pavement. The pavement also increases in the x-direction. Although the trends in the pavement from Seney, Iowa, look similar to the trends in the pavement from Hospers, Iowa, fitting a model that would produce reasonable coverage probability took more effort than fitting a model for the Hospers data set. The final model is as follows:

$$Z = \beta_0 + \beta_1 Y_0 + \beta_2 X + \beta_3 |Y| + \beta_4 Y^2 + \beta_5 Y^4 + \beta_6 Y_1 \tag{5.1}$$

Where $Y_0 = \begin{cases} 1, & \text{if } Y \geq 0 \\ 0, & \text{if } Y < 0 \end{cases}$ and $Y_1 = \begin{cases} Y, & \text{if } Y \geq 0 \\ 0, & \text{if } Y < 0 \end{cases}$
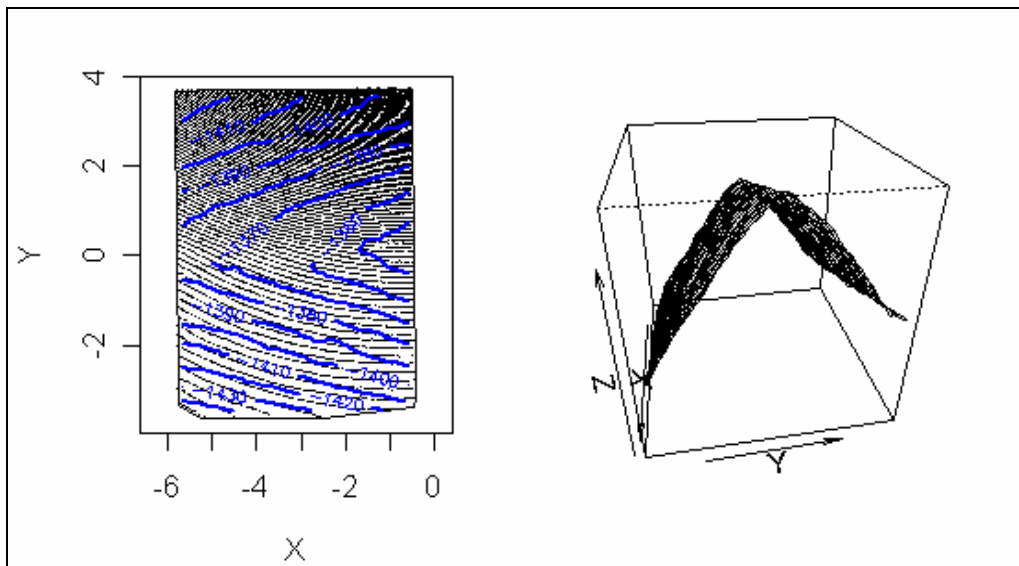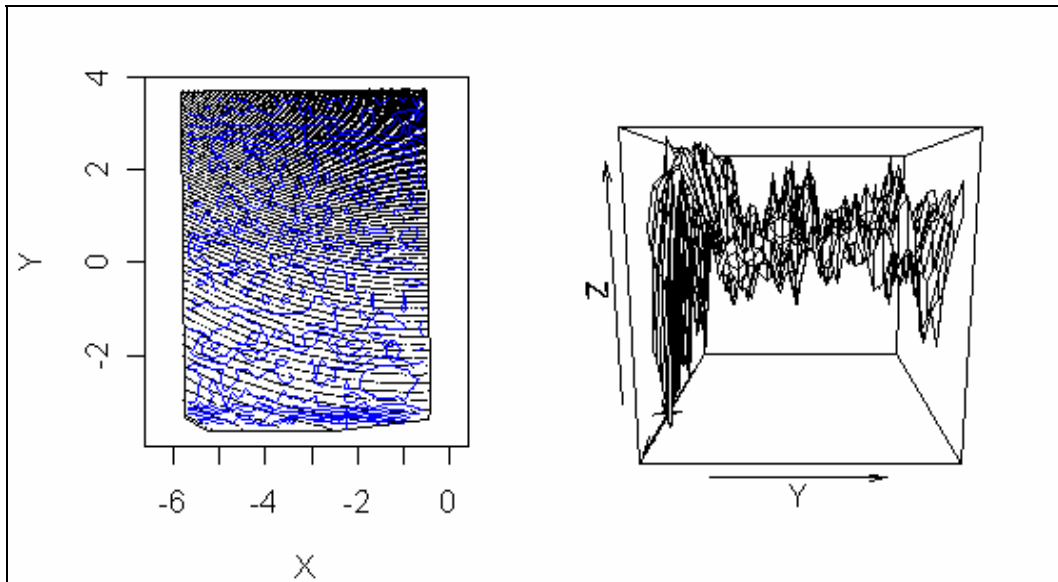

Figure A.25. Contour plot and perspective plot of the pavement data set

Table A.11 contains the ordinary least squares estimates for the parameters, while Figure A.26 contains the contour plot and the perspective plot of the residuals. All three types of empirical variograms were calculated based on a random sample of 2,000 residuals from the model and their respective locations. The empirical variogram with an azimuth angle of 90 degrees appears to the most appropriate for fitting a theoretical variogram. Spherical and exponential variograms were fitted to the empirical variogram and can be found in Figures A.27 and A.28, while the parameters can be found in Table A.12. According to the weighted least squares criterion, the spherical variogram fits the empirical variogram better than exponential variogram.

Table A.11. Parameter estimates for Model 1

Parameters	Estimates
β_0	-1338.390
β_1	-1.602
β_2	5.921
β_3	-12.357
β_4	-3.702
β_5	0.129
β_6	4.286

Figure A.26. Contour plot and perspective plot of residuals (mm) from Model 1
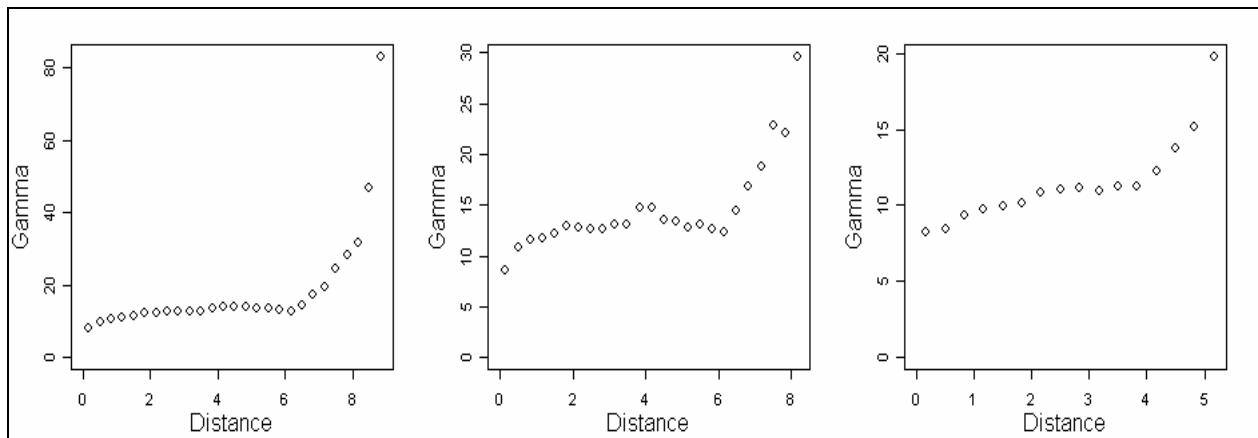
Figure A.27. Empirical semi-variogram of the residuals (left to right: omnidirectional, 0 degrees, and 90 degrees)
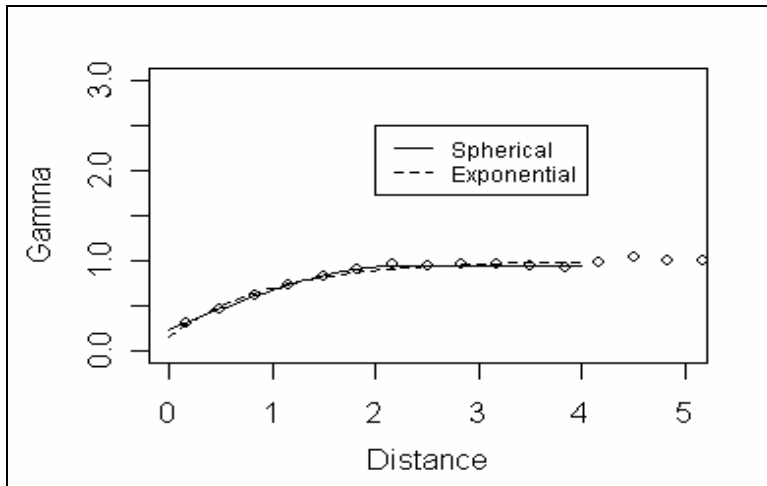
Figure A.28. Fitted theoretical semi-variograms

Table A.12. Estimates of parameters for theoretical variograms

Parameters	Spherical	Exponential
Tausq	0.238	0.156
Sigmasq	0.714	0.847
Phi	2.307	0.976
WLS criterion	52.80	490.33

Next, ordinary kriging was performed based on the spherical variogram for the validation data set. Predictions and prediction squared errors for the validation data set are shown graphically in the image and contour plots in Figure A.29.
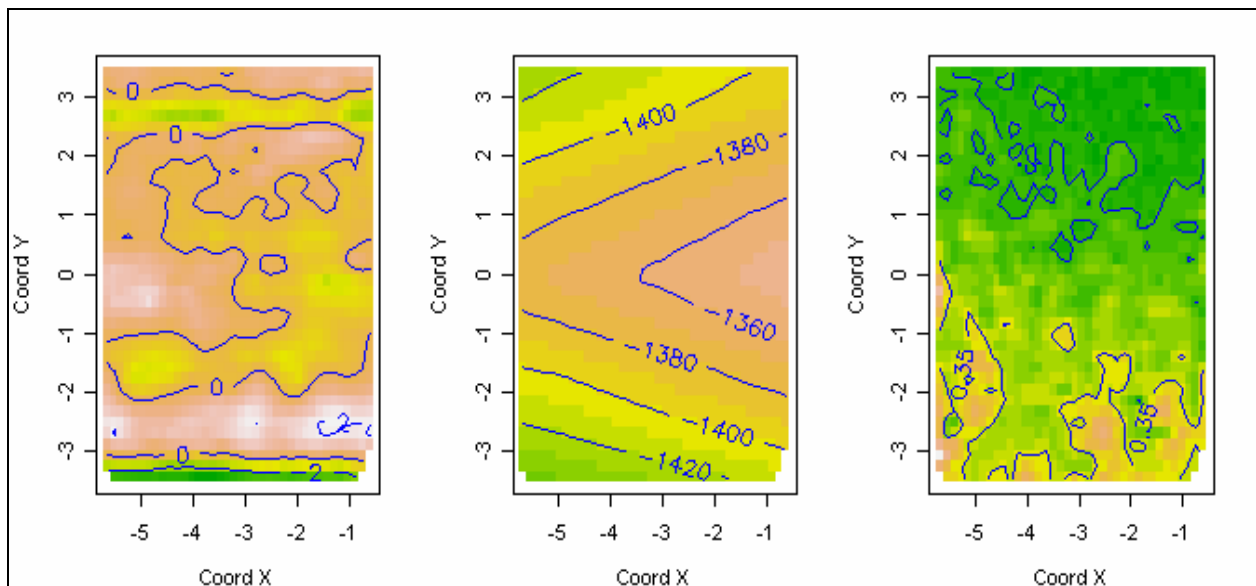
Figure A.29. Contour and image plots of predictions for residuals (left), predictions for pavement height (center), and squared errors (right)

For each location in the validation set, 95% confidence intervals for the height of the pavement were calculated. The coverage probability is 92.5%. Moreover, the median and the interquartile range of the width of the confidence intervals are 2.155 mm and 0.084 mm, respectively. The theoretical prediction mean squared error is 0.308, and the empirical prediction mean squared error is 0.371. After repeating the process 25 times, the minimum and maximum values for the coverage probability are 90.2% and 94.7%, respectively. The minimum and maximum values for the median width are 1.90 mm and 2.12 mm, respectively. Note that only a spherical variogram was fitted to the empirical variogram for every random sample and used for prediction.

5.2. Subbase Data Set

The subbase was rotated in the same manner as the pavement data set and is shown in Figure A.30. To model the trend in the subbase, the same model that was used for the pavement data set will be used, except for the two terms Y^2 and Y^4, since the coverage probability for the 95% confidence intervals was much less than the expected coverage probability. The ordinary least squares estimates can be found in Table A.13 and the contour plot and perspective plot of the residuals from Model 2 can be found in Figure A.31. The model for the subbase is given as follows:

$$Z = \beta_0 + \beta_1 Y_0 + \beta_2 X + \beta_3 |Y| + \beta_4 Y_1,$$ (5.2)

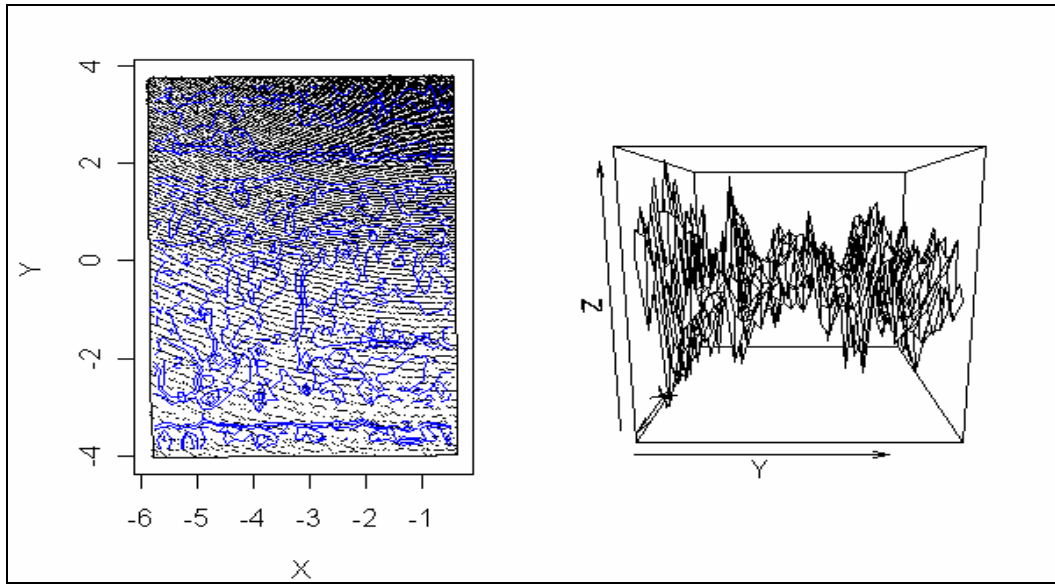Where $Y_0 = \begin{cases} 1, & if \ Y \geq 0 \\ 0, & if \ Y < 0 \end{cases}$ and $Y_1 = \begin{cases} Y, & if \ Y \geq 0 \\ 0, & if \ Y < 0 \end{cases}$
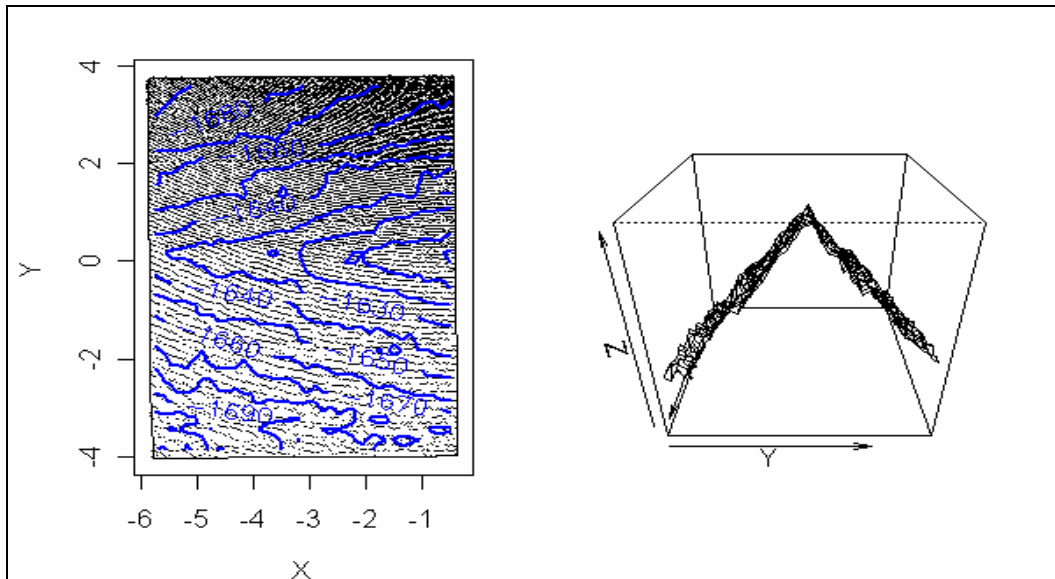
Figure A.30. Contour plot and perspective plot of the subbase data set

Table A.13. Parameter estimates for Model 2

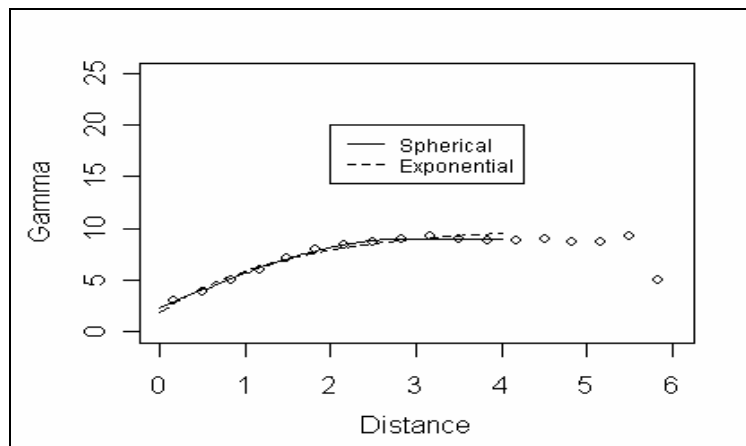| Parameters	Estimates
β_0	-1598.777
β_1	3.435
β_2	6.218
β_3	-19.866
β_4	1.335

Figure A.31. Contour plot and perspective plot of residuals (mm) from Model 2

The next step was to plot the empirical variograms, as shown in Figures A.32 and A.33. Again, the empirical variogram with an azimuth angle of 90 degrees appears to be the most appropriate for fitting an exponential or spherical variogram. The parameter estimates for the spherical and exponential variograms are shown in Table A.14. Again the spherical variogram fits the empirical variogram better than the exponential variogram.

Ordinary kriging was performed using the spherical variogram for the validation data set. The 95% confidence intervals, which were calculated for each location in the validation data set, produced a coverage probability of 91.9%. Moreover, the median and the interquartile range of the width of the confidence intervals are 6.610 mm and 0.248 mm, respectively. The theoretical prediction mean squared error is 2.886, while the empirical prediction mean squared error is 3.881. After repeating the process 25 times, the minimum and maximum values for the coverage probability are 89.8% and 93.9%, respectively. The minimum and maximum values for the median width are 6.02 mm and 6.87 mm, respectively. Note that only a spherical variogram was fitted to the empirical variogram for every random sample and used for prediction.
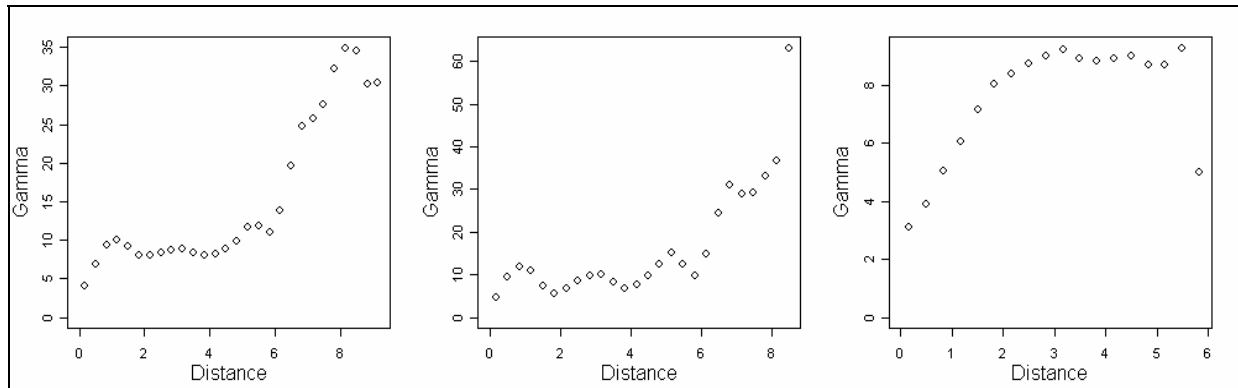
Figure A.32. Empirical semi-variogram of the residuals (left to right: omnidirectional, 0 degrees, and 90 degrees)


Figure A.33. Fitted theoretical semi-variogram

Table A.14. Estimates of parameters for theoretical variograms

Parameters	Spherical	Exponential
Tausq	2.305	1.891
Sigmasq	6.692	8.228
Phi	2.884	1.521
WLS criterion	137.40	696.28

5.3. Depth of Pavement

Ordinary kriging was then used to aid in predicting the height of the pavement and the height of the subbase at the locations that were selected for the subbase validation data set. Confidence intervals were calculated based on a significance level of 0.05. The median width and interquartile range of the 95% confidence intervals were 6.957 mm and 0.267 mm, respectively. The image and contour plots of the predictions for the depth of the pavement and the squared errors are shown in Figures A.34 and A.35.
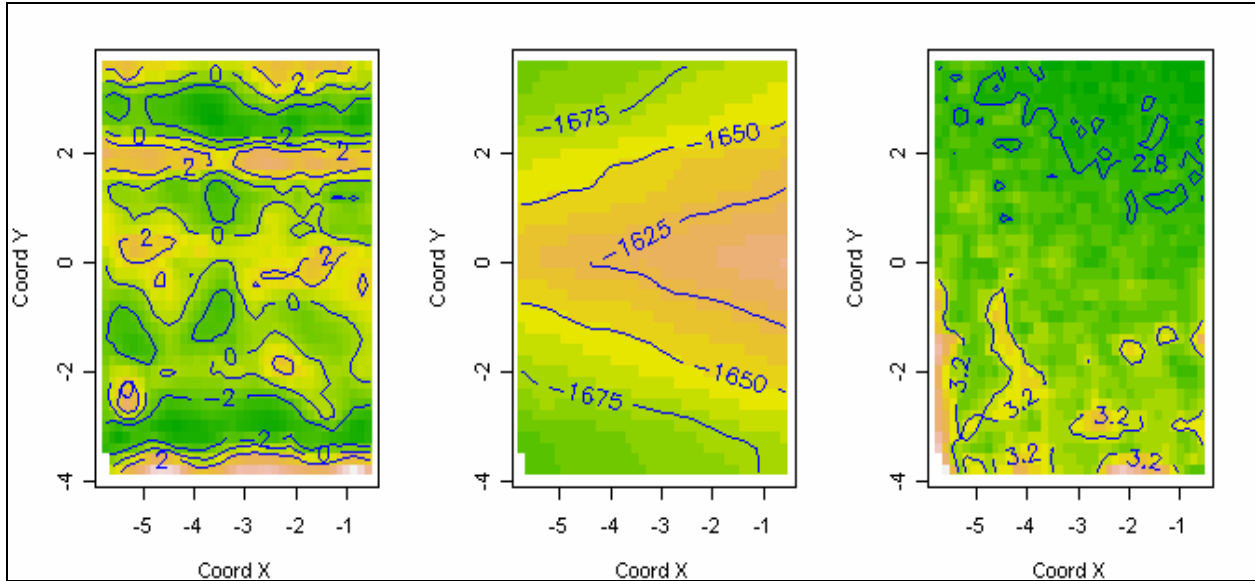
Figure A.34. Contour and image plots of predictions of residuals (left), predictions of subbase height (center), and squared errors (right)
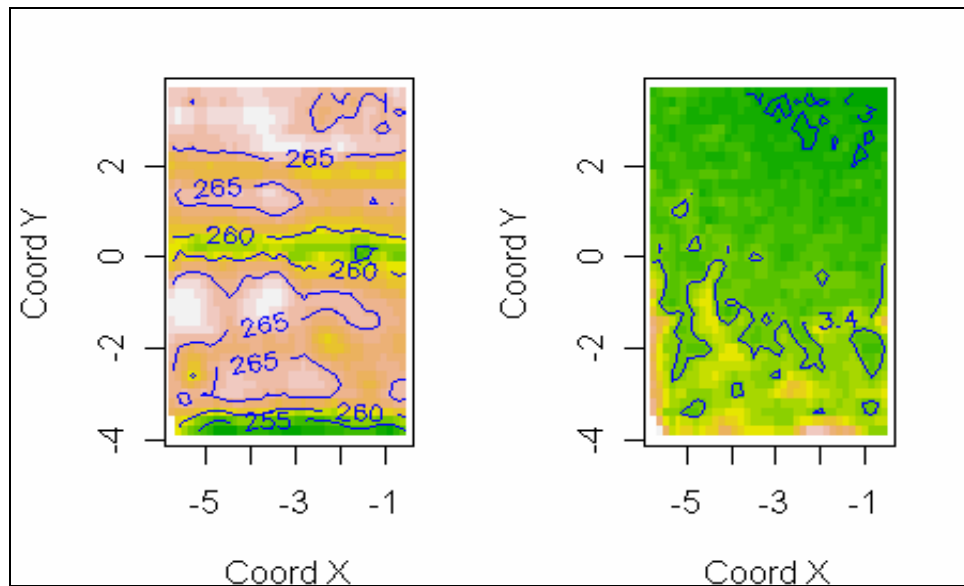
Figure A.35. Contour and image plots of predicted depth of pavement (left) and squared errors (right)

6. Summary of Kriging Results

Data were collected from three different locations in Iowa: Hospers, Tama, and Seney. For all the pavement and subbase data sets, a linear model was fitted to the data to account for large-scale trends in the pavement and subbase. Subsequently, 2,000 observations were randomly selected to calculate an empirical variogram. Ordinary kriging was then performed using a spherical or exponential variogram at 2,000 locations that were randomly selected from the

90

remaining observations that were not used for the calculation of the empirical variogram. The choice of the spherical or exponential variogram was based on the weighted least squares criterion.

The method of analyzing the data did not change from location to location, except for the form of the linear model that was used to account for large-scale trend in the pavement or subbase. In some cases, additional terms had to be added to account for structure that could not be seen in a certain perspective. Once a model had been fitted and a perspective plot had been created based on the residuals, only then were additional trends seen that could be explained by a linear model. In addition, the coverage probability in some cases was a little less than the expected 95% coverage probability. At this time, there is no apparent reason why the coverage probability is slightly less than what would be expected. The differences in coverage probability, median width of the confidence intervals, and prediction mean square error can be seen in Table A.15.

Table A.15. Summary of kriging results

		Hospers	**Tama**	**Seney**
Pavement	Coverage probability	96.6%	93.9%	92.5%
	Median width (mm)	2.45	1.34	2.16
	Prediction MSE	0.402	0.112	0.308
Subbase	Coverage probability	95.9%	94.6%	91.9%
	Median width (mm)	6.98	11.30	6.10
	Prediction MSE	3.230	8.336	2.886

7. Impact of Number of Observations on Squared Errors

To determine how the number of observations impacts the size of the squared errors, several subsets of different sizes from the Hospers data set were analyzed. First, several data sets of different sizes were created from the pavement data set. Since the computer was only able to perform kriging for data sets with approximately 2,000 observations or less, all the data subsets contain 2,000 observations or less. Since the pavement data set based on the residuals produced by Model 2 has 5,905 data points, every third observation was chosen for the first data set, starting with the first observation; the second data set contains every fourth observation; the third data set contains every fifth observation, and so on. Finally, the eighth data set contains every tenth observation. The validation set for the first data set contained every third observation, but began with the second observation. For each data set, the empirical directional variogram with an azimuth angle of 90 degrees was fitted with a spherical variogram. The variogram was then used to predict the locations in the respective validation data set. For each data set, the coverage probability and the prediction mean squared error were calculated. The subbase data set was analyzed in the same manner except that the largest data set contains every fourth observation and the smallest data set contains every thirteenth observation. Also, the empirical directional variogram with an azimuth angle of 90 degrees was fitted with an exponential variogram.

Figure A.36 plots the coverage probability and the prediction mean squared error versus the number of observations for both the pavement and subbase data sets. Notice that for data sets produced from either the pavement or subbase data sets that contain 500 to 1,000 points, the

mean square prediction error and the coverage probability are quite variable, whereas for data sets that contain more than 1,000 data points, the coverage probability and prediction mean squared error are both relatively stable.
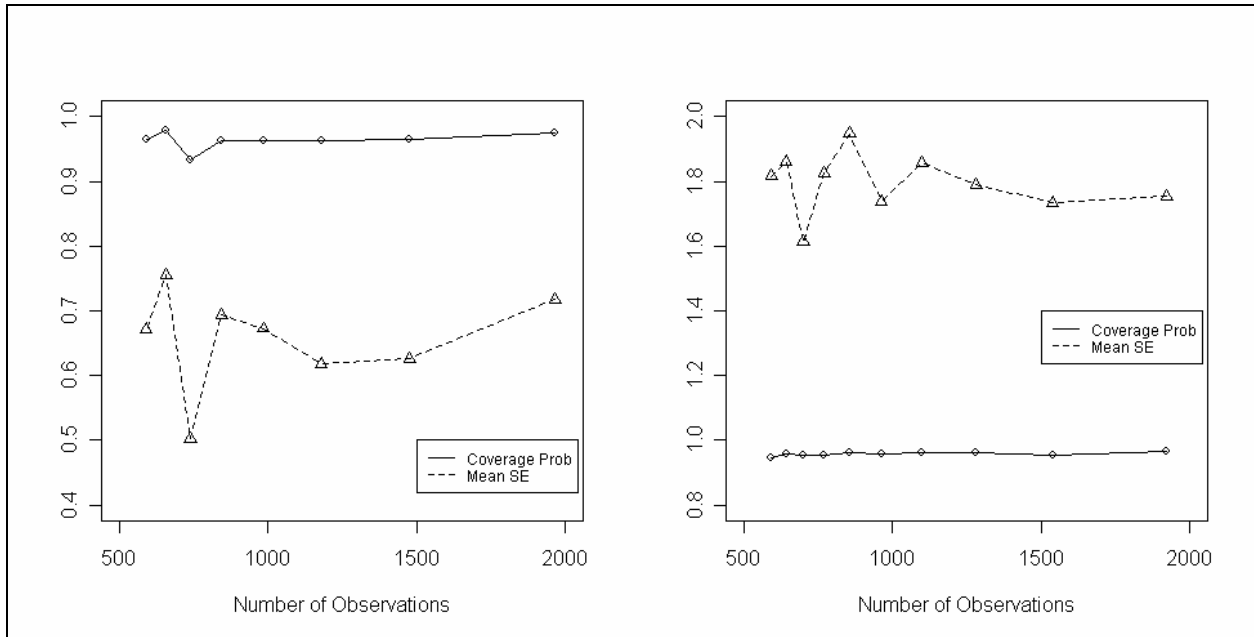
Figure A.36. Coverage probability and prediction mean squared error vs. number of observations for Hospers pavement data set (left) and Hospers subbase data set (right)

From the analysis presented in this section as well as the previous sections, a data set that covers an area similar in size to the area covered by the Hospers data set should contain at least 1,500 points to fit a model and create an empirical variogram to fit a theoretical variogram. The data set should also include additional observations to serve as the validation set. Having additional observations to check the model fit is recommended because, during the analysis of the three data sets, some of the models that were used to remove the trends led to a coverage probability that was much less than the expected confidence level, even when the empirical variograms gave little indication that there would be a significant difference between the expected coverage probability and the actual coverage probability.